

---

# Development of High Power Pump Laser for Future Sources of Isolated Attosecond Pulses

Dmitrii Kormin

---



München 2021



---

# **Development of High Power Pump Laser for Future Sources of Isolated Attosecond Pulses**

**Dmitrii Kormin**

---

Dissertation  
an der Fakultät für Physik  
der Ludwig-Maximilians-Universität  
München

vorgelegt von  
Dmitrii Kormin  
aus Petropavlovsk, Kasachstan

München, den 18.05.2021

Erstgutachter: Prof. Dr. Ferenc Krausz  
Zweitgutachter: Prof. Dr. Oleg Pronin  
Tag der mündlichen Prüfung: 18.05.2021

# Zusammenfassung

Neueste Entwicklungen in der Lasertechnologie haben zur Entstehung leistungsfähigen Lichtquellen geführt, die Lichtpulse mit wenigen Zyklen und Energien von bis zu 100mJ liefern können. Bei Intensitäten in der Größenordnung von  $10^{20}\text{W}/\text{cm}^2$ , scheinen solche Lasersysteme die perfekten Treiber für relativistische Wechselwirkungen zwischen Licht und Materie zu sein, die nach theoretischen Berechnungen zur Erzeugung von intensiven isolierten Attosekundenpulsen geeignet sein sollten. Attosekundenpulse sind wiederum für viele Projekte in der Grundlagenforschung zu ultraschnellen Phänomenen von großem Interesse.

Die vorgestellte Arbeit besteht aus zwei Forschungsprojekten, die durch die Idee verbunden sind, eine ideale Quelle für intensive isolierte Attosekundenpulse zu entwickeln. Der erste Teil bezieht sich auf das sogenannte SHHG-Experiment (Surface High Harmonics Generation), das mit einem modernen Laser mit dem Pulsdauer von zwei Lichtwellenzyklen betrieben wird. In diesem Experiment wurde Ultraviolettstrahlung von bis zu 100eV auf der Oberfläche einer Quarzglasplatte erzeugt. Die Untersuchung der Abhängigkeit dieser Strahlung von der Form des elektrischen Laserfeldes führte zur Entwicklung einer neuartigen Technik zur Analyse der Oberschwingungsspektren. Dieses Verfahren erweitert die Idee der konventionellen spektralen Interferometrie auf das Zusammenwirken von drei nicht äquidistanten Attosekundenpulsen und ermöglicht (unter bestimmten Bedingungen) die Rekonstruktion der zeitlichen Struktur des erzeugten ultravioletten Pulszugs. Solche Rekonstruktionen zeigten eine gute Übereinstimmung mit den Ergebnissen numerischer Simulationen und bestätigten die Verwendbarkeit des Antriebslasers zur Erzeugung hochisolierter Attosekundenpulse bei bestimmten, von experimentellen Voraussetzungen abhängigen Formen des elektrischen Feldes.

Allerdings ist die Helligkeit einer solchen Attosekundenpulsquelle durch die Wiederholrate des Treiberlasers begrenzt. Niedrigere Pulsenergie der vorhandenen Laser der Kilohertz-Klasse mit wenigen Lichtwellenzyklen zeigt, dass die Skalierung der Durchschnittsleistung nicht trivial ist und eine weitere Verbesserung der bestehenden Lasertechnologien erfordert, unter anderem die Entwicklung geeigneter Pumplaser mit hoher Durchschnittsleistung.

Dem wissenschaftlichen Weg des Autors folgend, wechselt der Forschungsschwerpunkt des zweiten Teils der Arbeit zu den Pumplasern mit hoher Pulsenergie und Wiederholrate. Ein der bislang fortschrittlichsten Pumplaser mit Pikosekundenpulsedauer basiert auf der Dünnscheibentechnologie und liefert 200mJ Pulsenergie mit einer Wiederholrate von 5 kHz. Um die Verwendbarkeit dieses Lasers durch Erhöhen der Pulsenergie und/oder der Durchschnittsleistung zu verbessern, wurde ein zusätzlicher Multipass-Verstärker auf Basis dünner Scheiben entwickelt. Es wurde gezeigt, dass ein herkömmliches  $4f$ -Bildgebungsdesign aufgrund der starken Verschlechterung des Strahlprofil für eine große Anzahl von Durchgängen nicht verwendbar ist. Im Gegensatz dazu ermöglichte die Verwendung des modernhaltenden Quasi-Resonator-Design eine effiziente Verstärkung unter Beibehaltung der resonatorähnlichen Strahlqualität ( $M^2 \approx 1.12$ ), die für die Multipass-Verstärker einzigartig ist. Der Verstärker verwendete eine Eingangsleistung von  $\sim 200\text{W}$  bei 5kHz und erzeugte eine Ausgangsleistung

## **Zusammenfassung**

von über 1kW. Eine solche Verwendung des Quellenlasers und des Verstärkers liefert zwei Pumpstrahlen mit Energien von 160mJ und 200mJ. Zusätzlich wurde alternativ dazu ein Betriebsmodus bei 1kHz Wiederholrate numerisch untersucht. Eine Pulsenergie von fast 0.5J wird erwartet, wenn die vom Quelllaser maximal verfügbaren 200mJ Pulsen als Eingangssignal benutzt werden. Abschließend werden verschiedene Methoden zur möglichen Verbesserung der Stabilität und Verstärkung diskutiert.

Basierend auf all den oben genannten Ergebnissen stellt die aktuelle Arbeit nicht nur einen wichtigen Schritt in Richtung zukünftiger Quellen der Attosekundenpulse dar, sondern treibt auch die vorhandenen Lasertechnologien voran, was wiederum zu vielfältigen grundlegenden und angewandten Forschungsprojekten beitragen könnte.

# Abstract

Recent progress in laser technologies has led to emergence of powerful ultra-short light sources that can deliver few-cycle pulses with energies up to 100mJ. Providing the intensities on the order of  $10^{20}\text{W/cm}^2$  such laser systems appear to be the perfect drivers for relativistic light-matter interaction experiments, which according to theoretical investigations should be suitable for generation of intense isolated attosecond pulses. In turn, attosecond pulses are of high interest for many fundamental researches in ultrafast science.

The presented work consists of two research projects that are united by the idea of developing an ideal source of intense isolated attosecond pulses. First part is related to so called *surface high harmonics generation* (SHHG) experiment driven by the state-of-the-art few-cycle laser. In this experiment extreme ultraviolet (XUV) emission up to 100eV was generated from the surface of a fused silica target. While studying the dependence of the generated XUV signal from the shape of the laser electric field, a novel approach in analysis of the harmonics spectra was invented. This technique extrapolates the idea of conventional spectral interferometry (SI) to the interaction of three non-equidistant attosecond pulses and (under certain conditions) allows to reconstruct the temporal structure of the generated XUV pulse train. Demonstrating good agreement with the results of numerical simulations, such reconstructions confirmed the usability of the driving laser for generation of highly isolated attosecond pulses in case of having certain, experimental conditions dependent shape of the electric field.

However the brightness of such a source of attosecond pulses is limited by the repetition rate of the driving laser. Lower pulse energy of the existing kilohertz-class few-cycle lasers indicates that scaling of the average power is not trivial and requires further improvement of the current laser technologies, including the development of suitable high average power pump lasers.

Following the scientific path of the author, the research focus of the second part of the thesis switches to the high pulse energy and repetition rate pump lasers. One of the most advanced picosecond pump lasers to date is based on *thin-disk* technology and provides 200mJ pulses at 5kHz repetition rate. In order to improve its usability by increasing the output pulse energy and/or average power an additional thin-disk based multipass amplifier was developed. Conventional  $4f$ -imaging propagation scheme was shown to be not usable for high amount of passes due to strong degradation of the beam. In contrary to this, usage of the mode-preserving *quasi-resonator scheme* allowed for efficient amplification while preserving the resonator-like beam quality ( $M^2 \approx 1.12$ ) that is unique for the multipass amplifiers. Being seeded with  $\sim 200\text{W}$  at 5kHz, the amplifier produced above 1kW of output power. Such usage of the source laser and the amplifier provides two pump beams with 160mJ and 200mJ respectively. In addition to this an alternative 1kHz operation regime was numerically investigated. Almost 0.5J pulse energy is expected if seeded with the maximal available from the source laser 200mJ pulses. Finally, various methods of possible stability and amplification improvement are discussed.

Based on all the above mentioned results, the current work not only presents an important step towards future sources of the attosecond pulses, but also pushes forward the existing laser technologies – which in turn might contribute to diverse fundamental and applied researches.

**Abstract**

# Contents

<b>Zusammenfassung</b> .....	<b>v</b>
<b>Abstract</b> .....	<b>vii</b>
<b>Contents</b> .....	<b>ix</b>
<b>List of figures</b> .....	<b>xi</b>
<b>List of tables</b> .....	<b>xiii</b>
<b>Abbreviations</b> .....	<b>xv</b>
<b>Introduction</b> .....	<b>1</b>
<b>Chapter 1 Generation of XUV emission from oscillating plasma surface</b> .....	<b>5</b>
1.1 Interaction of dense plasma with intense laser pulses .....	6
1.2 Driving laser and experimental setup .....	9
<b>Chapter 2 Recognition of isolated attosecond pulses</b> .....	<b>15</b>
2.1 Spectral interferometry .....	15
2.2 Analysis of the measured XUV spectra.....	19
2.2.1 Interference of two pulses.....	19
2.2.2 Interference of three pulses.....	21
<b>Prospect: A route towards an ideal source of isolated attosecond pulses</b> .....	<b>25</b>
<b>Chapter 3 Thin-disk based high power pump laser</b> .....	<b>28</b>
3.1 Propagation and transformation of laser beams .....	28
3.1.1 Ideal Gaussian beam .....	28
3.1.2 Ray transfer matrix method .....	31
3.1.3 Real beam and embedded Gaussian principle .....	33
3.2 Basic principles of laser amplifiers .....	34
3.2.1 Optical transitions in a medium .....	34
3.2.2 Yb:YAG emission and absorption cross-section .....	36
3.2.3 Numerical description of amplification .....	37
3.2.4 Regenerative and multipass amplifiers .....	38
3.2.5 CPA principle and dispersion control.....	40
3.3 Thin-disk lasers .....	41
3.3.1 Thin-disk geometry.....	41

## Contents

3.3.2 Thin-disk based 1kW sub-picosecond pump laser .....	43
<b>Chapter 4 Multipass amplifier .....</b>	<b>45</b>
4.1 Pump and seed beams .....	46
4.1.1 Pump laser and imaging optics .....	46
4.1.2 Pump and seed spot sizes .....	47
4.2 Imaging configuration .....	53
4.2.1 Principle of $4f$ -imaging .....	53
4.2.2 Realization of $4f$ -imaging with two disks .....	54
4.2.3 Beam propagation .....	56
4.2.4 Amplification and beam quality .....	59
4.2.5 Results and conclusions .....	64
4.3 Quasi-resonator configuration .....	65
4.3.1 Eigenmode preservation .....	65
4.3.2 Deviation from the eigenmode .....	67
4.3.3 Mode matching .....	69
4.3.4 Stability and alignment .....	72
4.3.5 Beam quality .....	75
4.3.6 Amplification .....	78
4.3.7 Characterization of the output beam .....	83
4.4 Potential for further development .....	86
4.4.1 Amplification enhancement .....	86
4.4.2 Operation at 1kHz .....	88
<b>Summary and outlook .....</b>	<b>91</b>
<b>Appendix A Prepulse generation .....</b>	<b>93</b>
<b>Appendix B Amplification simulation .....</b>	<b>95</b>
B.1 Basic assumptions .....	95
B.2 Seed ellipse expansion .....	96
<b>Appendix C Damage threshold estimation .....</b>	<b>99</b>
<b>Appendix D Data archiving .....</b>	<b>101</b>
<b>Bibliography .....</b>	<b>103</b>
<b>List of publications .....</b>	<b>109</b>
<b>Acknowledgements .....</b>	<b>111</b>

# List of figures

Figure 1-1: Generation of XUV emission from solid surface. ....	6
Figure 1-2: Evolution of the electron density.....	7
Figure 1-3: Plasma motion simulation. ....	8
Figure 1-4: Carrier-envelope phase. ....	9
Figure 1-5: Non-collinear OPA. ....	10
Figure 1-6: LWS-20 amplification scheme. ....	10
Figure 1-7: Experimental setup scheme. ....	11
Figure 1-8: Dependence of the measured XUV signal on the prepulse delay. ....	12
Figure 1-9: Used SiO <sub>2</sub> target. ....	12
Figure 1-10: Measured harmonics spectra. ....	13
Figure 2-1: Conventional spectral interferometry. ....	15
Figure 2-2: Numerical model of interference of three pulses. ....	16
Figure 2-3: Fourier analysis of the interference spectrum. ....	17
Figure 2-4: Comparison of the reconstructed and the original data. ....	19
Figure 2-5: Spectral interferometry with two attosecond pulses.....	20
Figure 2-6: Spectral interferometry with three attosecond pulses.....	22
Figure 2-7: Reconstructed pulse train. ....	23
Figure 2-8: Highly-isolated attosecond pulse.....	24
Figure 3-1: TEM modes. ....	30
Figure 3-2: Gaussian beam evolution.....	30
Figure 3-3: Ray transfer matrix method.....	31
Figure 3-4: M-squared parameter of a real beam. ....	33
Figure 3-5: Optical transitions in 2-, 4- and 3-level systems. ....	34
Figure 3-6: Emission and absorption cross-section of Yb:YAG.....	37
Figure 3-7: Two types of amplifiers.....	39
Figure 3-8: Principle scheme of a grating compressor.....	40
Figure 3-9: Thin-disk geometry. ....	42
Figure 3-10: Principle scheme of the source laser. ....	43
Figure 4-1: Pump beam imaging. ....	46
Figure 4-2: Super-Gaussian beam. ....	48
Figure 4-3: Spatial beam distortions related to the pump spot size.....	49
Figure 4-4: Simulation of the population depletion for different seed powers. ....	51
Figure 4-5: Progressing population depletion during strong seed amplification. ....	51
Figure 4-6: Output beam profile in case of significant depletion.....	52
Figure 4-7: 4 <i>f</i> -imaging.....	53
Figure 4-8: Multipass 4 <i>f</i> -imaging scheme.....	54
Figure 4-9: Vacuum chambers. ....	55
Figure 4-10: Folding mirror and imaging mirrors.....	56
Figure 4-11: Correct propagation of the seed beam inside the amplifier. ....	57
Figure 4-12: Propagation change caused by the thermal lens effect.....	58

## List of figures

Figure 4-13: Amplification curves.....	59
Figure 4-14: Amplification in case of smaller pump spot.....	60
Figure 4-15: Distortions in the output beam.....	61
Figure 4-16: Accumulation of the beam distortions.....	62
Figure 4-17: Example of Airy pattern.....	63
Figure 4-18: Output beam profile in case of smaller seed beam.....	63
Figure 4-19: Simulation of the output power for bigger seed-to-pump spot sizes ratio.....	64
Figure 4-20: Eigenvector preservation.....	65
Figure 4-21: Dependence of the eigenmode from the propagation distance.....	66
Figure 4-22: Quasi-resonator scheme.....	66
Figure 4-23: Evolution of the eigenmode inside the amplifier.....	67
Figure 4-24: Eigenmode robustness.....	68
Figure 4-25: Dependence of the eigenmode from the disks radius of curvature.....	68
Figure 4-26: Oscillation of the beam size.....	69
Figure 4-27: Input scaling telescope.....	70
Figure 4-28: Sine fit in case of different input beams.....	72
Figure 4-29: On-disk seed pattern in case of the input beam misalignment.....	73
Figure 4-30: On-disk seed pattern in case of the disk misalignment.....	74
Figure 4-31: Depletion observation.....	74
Figure 4-32: Beam quality without pumping.....	75
Figure 4-33: Influence of the pump power on the output beam profile.....	76
Figure 4-34: Stability drop in case of reaching the edge of the pump spot.....	77
Figure 4-35: High-gain amplification.....	78
Figure 4-36: Amplification with reduced amount of bounces.....	80
Figure 4-37: Double seed spot alignment.....	81
Figure 4-38: Double seed spot amplification.....	81
Figure 4-39: Double seed spot amplification in case of bigger pump spot.....	82
Figure 4-40: Stable operation at 1kW.....	83
Figure 4-41: $M^2$ measurement at 1kW output power.....	83
Figure 4-42: Narrowing of the output spectrum.....	84
Figure 4-43: Measurement of the output pulse duration.....	85
Figure 4-44: Double-passing principle.....	86
Figure 4-45: Optimal amount of bounces.....	87
Figure 4-46: Simulation of the output pulse energy at 1kHz.....	89
Figure S-1: Prepulse generation.....	93
Figure S-2: Dynamics of the upper state population.....	96
Figure S-3: Simulations of the ellipse effect at low pump power.....	97
Figure S-4: Simulations of the ellipse effect at high pump and seed power.....	97

# List of tables

Table 3-1: Ray transfer matrices of simple optical components.....	32
Table 4-1: Influence of the input telescope .....	71

## List of tables

# Abbreviations

<b>SHHG</b>	–	surface high harmonics generation
<b>XUV</b>	–	extreme ultra violet
<b>OPCPA</b>	–	optical parametric chirped pulse amplification
<b>SI</b>	–	spectral interferometry
<b>AR</b>	–	anti-reflection
<b>FWHM</b>	–	full width at half maximum
<b>CEP</b>	–	carrier-envelope phase
<b>NOPA</b>	–	non-collinear optical parametric amplification
<b>BBO</b>	–	beta barium borate, $\text{Ba}(\text{BO}_2)_2$
<b>LBO</b>	–	lithium triborate, $\text{LiB}_3\text{O}_5$
<b>KDP</b>	–	potassium dihydrogenphosphate, $\text{KH}_2\text{PO}_4$
<b>ATI</b>	–	above-threshold ionization
<b>FT</b>	–	Fourier transformation
<b>GD</b>	–	group delay
<b>PIC</b>	–	particle-in-cell
<b>TEM</b>	–	transverse electro-magnetic mode
<b>RoC</b>	–	radius of curvature
<b>YAG</b>	–	yttrium aluminum garnet, $\text{Y}_3\text{Al}_5\text{O}_{12}$
<b>CPA</b>	–	chirped pulse amplification
<b>CAIGO</b>	–	ytterbium compound $\text{Yb}^{3+}:\text{CaGdAlO}_4$
<b>CW</b>	–	continuous wave
<b>ASE</b>	–	amplified spontaneous emission
<b>UEL</b>	–	upper energy level

**Abbreviations**

# Introduction

Modern science reveals an apparent connection between the macro- and the micro- processes and objects in the world. The more we understand about the interaction of atoms and molecules in matter, the more powerful our vehicles and engines are. The more powerful particle accelerators we can build, the deeper we can look inside the atomic nuclei. Modern technologies allow us to travel all over the world and even further: we send research probes outside the Solar system and build the space-shuttles that bring the astronauts to the near-earth orbit and back. Engineering of such complicated high-technological units is directly connected to the nanometers ( $10^{-9}\text{m}$ ) scale lithography, which allows producing compact and fast electronics that is able to switch on the time frames of nanoseconds ( $10^{-9}\text{s}$ ). Thus further development of human civilization – whether the interstellar travels over the trillions of kilometers or invention of high-precision medical tools is implied – is closely related to investigations of various ultrafast processes occurring on the molecular and atomic scales. Such research will not only advance our understanding of the fundamental laws of the universe, but can also lead to an important breakthrough and big changes in our daily life.

Basic approach in studying fast processes can be well illustrated with Motion Picture principle that Eadweard Muybridge [1] used for recording of the motion with several usual (single-shot) photo cameras: continuous motion of an object can be well described with several consecutive static images, if the translations of the object between each two images is relatively small. Moreover, if the process is reproducible and can be manually repeated required number of times, the corresponding sequence of the static images can be recorded using only a single camera and adjusting the delay before making a snapshot. This example also implies that the camera is fast enough to make a nice static image without blurry traces that appear when a fast moving object is recorded with a too long exposure. Realization of this principle for studying the ultrafast dynamics inside matter is called *pump-probe technique*: the system under study – electrons, atoms or molecules – is first triggered (pumped) by the first laser pulse and then probed by the second one. The reaction of the system, for example the absorption spectrum, is measured as a function of the delay between these two laser pulses. In analogy to Motion Picture, if the pump and probe pulses (as well as the delay resolution) are significantly shorter than the characteristic time scale of the process, its evolution in time can be described by the obtained sequence of the delay-dependent measurement points.

Such research became possible after the invention of the first laser [2] and subsequent reaching the femtosecond ( $10^{-15}\text{s}$ ) duration of the laser pulses [3]. However for studying sub-femtosecond scale processes even shorter laser pulses are required, which supposes quite broad spectral bandwidth: a hundred attoseconds ( $100 \times 10^{-18}\text{s}$ ) pulse requires at least<sup>1</sup> 4000THz (about 17eV) of bandwidth, which is out of reach for any known laser material. Coherent spatio-temporal combining of several short (7–8fs) broadband pulses allows for

---

<sup>1</sup> Assuming a perfectly compressed Gaussian-shape pulse.

## Introduction

reaching sub-femtosecond duration (for example,  $\sim 380$ as were demonstrated in [4]), but does not seem to be significantly scalable.

In order to create sufficiently broadband emission so called *high-harmonics generation* process can be involved. For the first time it was observed during the nonlinear interaction of moderate-intensity ( $\sim 10^{13}$ – $10^{14}$ W/cm<sup>2</sup>) laser pulses with noble gases [5]. During such an interaction some electrons are freed from their atoms and accelerated: within one half of the laser cycle they are pushed away from the atoms, within the second half – when the electric field changes its direction – they are pulled back and re-collide radiating in ultraviolet or even X-ray ranges. Being driven by few-cycle lasers, such experiments allowed to generate isolated attosecond pulses [6] and gave a birth to attosecond physics [7].

An alternative to the conventional gas high harmonics generation is so called *surface high harmonics generation*, where the emission occurs as the result of the interaction between an intense laser pulse and overdense plasma generated on the solid surface [8, 9]. In contrary to gas harmonics, where exceeding the laser intensity of  $\sim 10^{15}$ W/cm<sup>2</sup> leads to reduction of the generation efficiency connected to the strong ionization of the gas medium [10], this approach can be used for efficient generation of intense isolated attosecond pulses at the laser intensities of  $10^{20}$ W/cm<sup>2</sup> [11]. Last achievements in the development of few-cycle lasers [12] allowed to perform corresponding experiments.

This thesis, as well as the research path of its author, is split into two parts. The first part is related to the experimental realization of the above mentioned approach and characterization of the generated attosecond pulses and their harmonics spectra. In the second part the research focus is shifted from the investigation of the generation process to further development of the laser technologies that would significantly improve the existing few-cycle lasers. Both parts are nevertheless united by the idea of creating a perfect source of intense isolated attosecond pulses that would allow for convenient performance of the ultrafast pump-probe experiments.

The word “convenient” here implies two main features. The first one is that the generated attosecond pulses should be intense enough to trigger even strongly nonlinear processes to the level of detection. The second important parameter is the repetition rate, which allows accumulating enough data within a reasonable time. It is not only important for statistics-based measurements (e.g. tagging the carrier-envelope phase like in [13]), but also for detection of weak signals using increased exposure times.

At the moment the most intense few-cycle lasers that are used for surface harmonics generation operate at the repetition rate of few hertz [14, 15]. Similar experiments can be also performed with kilohertz-lasers [16], but their low pulse energy does not allow to fully realize the main benefit of this approach (comparing to the traditional gas harmonics), namely usage of ultra-high intensities. The future third-generation few-cycle lasers [17] that could provide high energy pulses at (few) kilohertz repetition rate, require correspondently powerful pump lasers. This need stimulated the development of a kilowatt-class thin-disk based pump laser that can operate at 5kHz delivering 200mJ pulses [18].

The second part of this thesis describes the efforts aimed to overcome the limitations of the above mentioned laser, related to its principle design [19, p46–58]. Being extended with an additional amplifier, it can turn into a powerful pump laser for a future high-repetition rate few-cycle laser system, which will be able to drive an ideal source of isolated attosecond-pulses.

**Introduction**

# Part I

## Generation of isolated attosecond pulses

The first part of the manuscript is dedicated to generation of isolated attosecond pulses from relativistically oscillating plasma. It describes the interaction of ultra-intense laser pulses ( $I \approx 10^{20} \text{W/cm}^2$ ) with a solid surface leading to formation of an overdense plasma that generates extreme ultra-violet (XUV) emission. The generated XUV signal is presented by a train of very short pulses whose amount and properties depend on the driving laser pulse. **Chapter 1** gives a basic explanation of the underlying processes and describes the experimental setup together with the driving laser system and obtained XUV spectra. **Chapter 2** describes a new method of the measured spectra analysis that is based on the conventional spectral interferometry. It reveals (under certain conditions) the complete temporal structure of the pulse trains and allows for distinguishing of highly isolated pulses. In **Prospect** the key requirements are discussed, that modern few-cycle high-intensity lasers should fulfill in order to drive an ideal source of the isolated attosecond pulses.

### Chapter 1

## Generation of XUV emission from oscillating plasma surface

This chapter starts with a brief explanation of XUV emission process that occurs during the interaction of an intense laser pulse with dense plasma generated via ionization of a solid dielectric surface. During this interaction electrons reach relativistic velocities and emit bursts of pulses, which due to strong nonlinearity of the generation process appear to be significantly shorter than the driving laser period. In some specific conditions a single attosecond pulse can be obtained. The second section describes the experimental setup and the diagnostics that were used for detection and characterization of the generated emission. It also gives a compact description of LWS-20 [12], a laser system based on *optical parametric chirped-pulse amplification* (OPCPA, [20]), which due to its few-cycle high-energy pulses appears to be a perfect light source for driving this experiment. The demonstrated scheme of amplification of weak microjoule level seed pulses up to 100mJ clarifies the important role of the pump lasers in reaching high output pulse energy, which is essential for generation of strong isolated attosecond pulses via the discussed laser-plasma interaction. The chapter closes with a presentation of accumulated experimental data.

## 1.1 Interaction of dense plasma with intense laser pulses

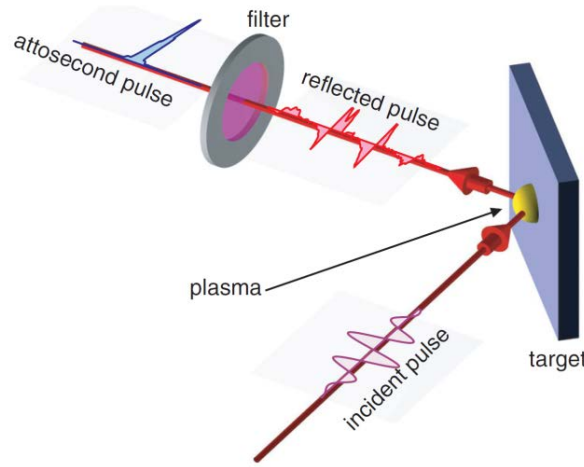


**Figure 1-1: Generation of XUV emission from solid surface.**

Incident laser pulse (p-polarized) ionizes the surface of solid material and is being reflected from the generated plasma. Being accelerated by the laser field, plasma electrons radiate in the direction of the reflected laser pulse. Generated emission is presented by a train of XUV pulses, whose amount and individual parameters depend on the laser field shape and electron density distribution. According to theoretical model in some particular cases it should be possible to separate a single isolated pulse with attosecond duration by using proper high-pass filter. The figure is taken from [11].

Generation of XUV emission from dense plasma created on the surface of solid materials is a very promising alternative to the gas harmonics generation [21] that is widely used for obtaining isolated attosecond pulses. Though this method allows for emission generation in the X-ray range [22], experimental data discussed and presented in this work correspond to 15–100eV and thus can be rightfully called XUV emission. Being tightly focused on the surface of a solid dielectric (usually SiO<sub>2</sub> glass), an intense laser pulse ionizes a thin layer of material and turns it into an expanding plasma bubble – a dense cloud of electrons and ions that broadens because of the electromagnetic interaction and a high kinetic energy of the particles. If the laser pulse is intense enough, the surface is ionized in the very beginning of the interaction with a pulse (at its rising edge) and the rest of the pulse is being reflected by a dense layer of free electrons in the plasma cloud performing as a *plasma mirror*. Since some descent intensity of the laser pulse is required for the surface ionization – for AR (anti-reflection) coated fused silica glass it can be  $\sim 10^{16} \text{W/cm}^2$  – plasma mirrors are often used for suppression of unwanted prepulses and pedestals: the front part of the laser pulse is not reflected until some threshold ionization intensity is reached [23].

However the surface can be also ionized by a special manually created prepulse that is sent in front of the main laser pulse. Depending on the time between the ionization and the main pulse arrival the spatial distribution of the electrons is different. It can be described with so called *plasma scale length* ( $L$ ), which defines the steepness of the electrons density gradient in the direction normal to the target surface:

$$n(x) = n_0 * e^{-x/L} \quad (1.1)$$

## 1.1 Interaction of dense plasma with intense laser pulses

Before the ionization the density distribution is presented by a step function, because all the electrons take their places in the solid body structure. Such a condition corresponds to  $L \rightarrow 0$ . Afterwards the plasma cloud starts expanding and the density profile becomes more and more sloping (**Figure 1-2**), what corresponds to increasing scale length  $L$ .

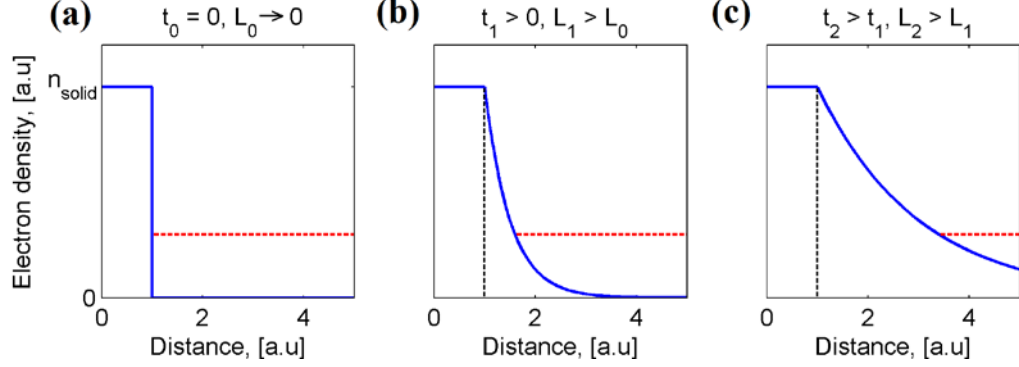


**Figure 1-2: Evolution of the electron density.**

(a) Before the ionization all the electrons take their places in the solid material structure. (b) Shortly after ionization most of the electrons are still concentrated close to the surface. (c) Further expansion of the plasma cloud, density profile becomes gradual. Vertical dashed (black) line corresponds to the surface coordinate. Horizontal dashed line (red) represents the critical density level.

Depending on the plasma scale length, the laser pulse can propagate to a different depth inside the plasma cloud. In a first approximation (neglecting small variance for different spectral component) incident light is reflected at the coordinate that corresponds to the *critical density*, which can be defined as

$$n_c = \frac{\epsilon_0 m_e}{e^2} \omega_L^2 \quad (1.2)$$

and has a meaning of the minimal electron density that can shield an electromagnetic wave with a frequency  $\omega_L$ . In case of a steep profile corresponding to a plasma condition immediately after the ionization, the laser pulse faces a very dense plasma cloud and is being reflected immediately. If the plasma cloud had enough time for some expansion, the laser pulse will propagate inside the low-density shell of the cloud until it reaches the critical density layer, which reflects it back. For the pulse cleaning purpose an almost steep plasma profile would be beneficial due to the minimal interaction with the low-density shell of the cloud. But for efficient generation of the XUV emission a slightly expanded plasma with  $L \approx 0.2\lambda_L$  is more suitable [24].

Being reflected from the critical-density-layer of electrons, the laser pulse also forces them to move accordingly to the electric field oscillations. During several optical cycles electrons are strongly pushed and pulled by the laser pulse field, which leads to emission of new photons that propagate together with the reflected laser pulse. This motion of the electrons can be well illustrated by **Figure 1-3**, showing the result of numerical simulations of the interaction between an intense few-cycle laser pulse and a slightly expanded plasma cloud. Three well visible dents framed with narrow layer of very high electron density (black color in the figure) correspond to three laser pulse cycles. At each cycle the rising electric field pushes the electrons towards the surface (right side of the figure) creating a layer of even higher density. When the

## Chapter1: Generation of XUV emission from oscillating plasma surface

electric field changes its sign in the end of the cycle, all these overdense bunches of electrons move back outside the surface. Because of the rising amplitude of the laser field (which now pulls the electrons) and a strong electrostatic force caused by a high local charge density, these electrons experience significant acceleration and radiate new electro-magnetic waves in ultraviolet and even X-ray ranges.

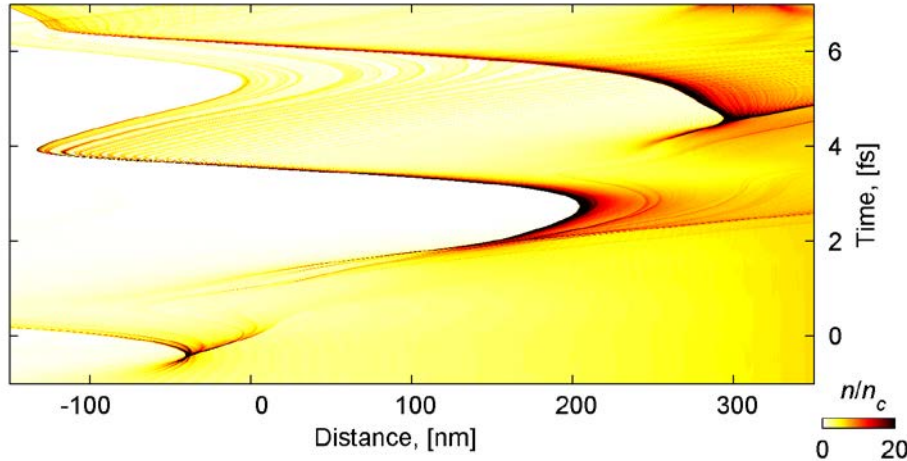


**Figure 1-3: Plasma motion simulation.**

Presented picture demonstrates the electron density distribution (plasma scale length  $L = 0.4\lambda_L$ ) during the interaction with a short, intense laser pulse ( $\tau_{FWHM} = 5fs$ ,  $T_L = 2.51fs$ ,  $\varphi_{CEP} = \pi$ ), calculated<sup>1</sup> using one-dimensional particle-in-cell (PIC) simulations [25]. Incident laser pulse propagates towards the target surface (from left to right), interacts with the electrons and is being reflected back. Three low-density dents (white color) at the period of  $\sim 2.5fs$  correspond to three oscillations of the laser field which push the electrons towards the surface. Each dent is framed with a dark line representing accelerated motion of the dense electron bunches outside the surface – in the direction of the reflected laser field – which leads to emission of new high-energy photons. Axes origins are relative.

The energy of the emitted photons (as well as their flux) nonlinearly depends on the electron acceleration. Due to this most of the emission at each laser cycle occurs within a very short timeframe when the resulting electromagnetic force affecting the electrons is at its maximum. Moreover, photons with the highest energy are only emitted when the acceleration reaches its peak. The stronger the laser field, the higher the maximum photon energy and the shorter the timeframe corresponding to emission of the most energetic photons. Thus extremely short XUV pulses can be obtained by filtering out low energy photons: according to the theoretical model [11] usage of a copper foil filter allows for  $\sim 5as$  duration, if the laser pulse is intense enough to generate photons with energies up to 1keV.

The amount of generated pulses and their individual characteristics (spectrum, photon flux etc.) do not only depend on the plasma condition, but also on the laser pulse shape. For long pulses with the duration of several cycles the exact electric field shape does not play any significant role, because several cycles with a comparably strong electric field are always presented in the middle of the laser pulse (**Figure 1-4a** and **b**). The generated pulse train will anyway consist of

<sup>1</sup> All the simulations presented in **Chapters 1** and **2** of the current work were performed by Dr. Guangjin Ma based on the approach presented in [25]. Necessary parameters and approximations can be found in Methods section of the original paper [14]. The same approach was used in [24] where the generation of isolated attosecond pulses during the laser-plasma interaction at such high intensities was investigated theoretically.

## 1.2 Driving laser and experimental setup

several XUV pulses with a few strong ones in the middle, whose individual intensity will slightly change depending on the exact shape of the electric field under the envelope. But for short laser pulses with the full width half maximum (FWHM) duration about two electric field cycles and shorter the situation is completely different. Subfigures **c** and **d** demonstrate such a pulse with two different values of *carrier-envelope phase* (CEP) – an instantaneous phase offset between the pulse envelope maximum and the electric field oscillations.

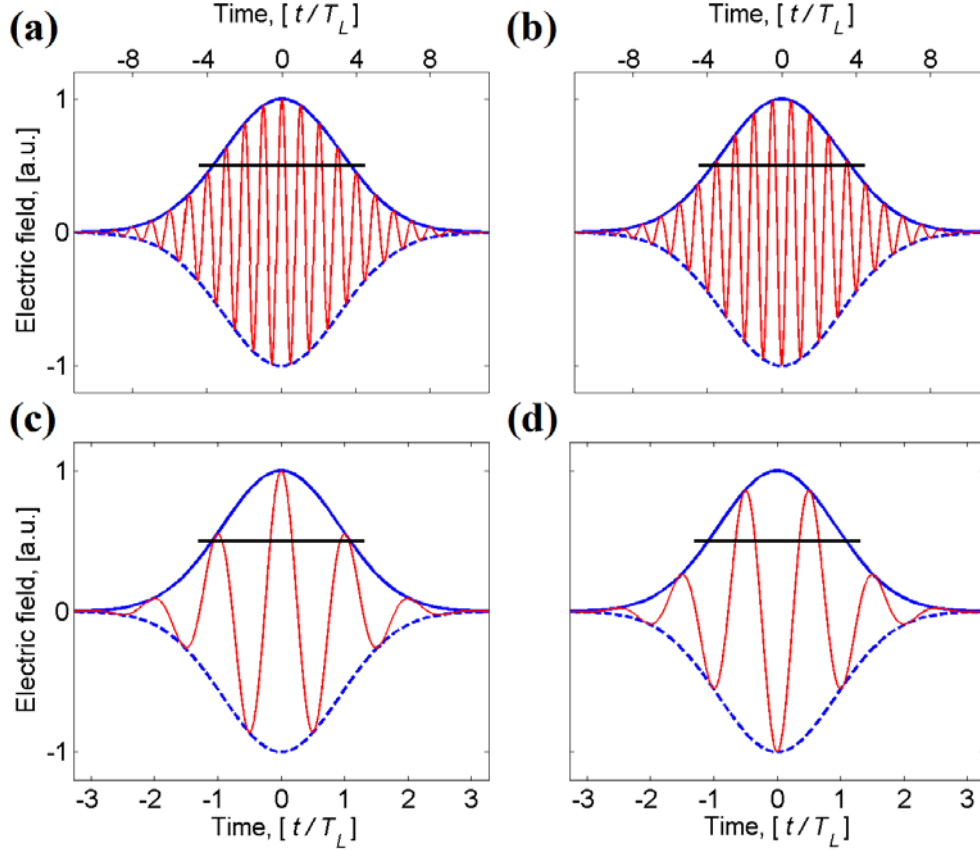


**Figure 1-4: Carrier-envelope phase.**

The shape of the electric field inside a laser pulse is approximated with Gaussian intensity envelope (FWHM level is shown with black lines) and fast harmonic oscillation at the central frequency  $\omega_0 = 2\pi/T_L$ . **(a)** Long pulse ( $\tau_{FWHM} \approx 8T_L$ ) with coinciding envelope maximum and field oscillation phases, i.e.  $\varphi_{CEP} = 0$ . **(b)** The same long pulse with  $\varphi_{CEP} = \pi$ . Regardless of the exact field shape it has several strong cycles. **(c)** Short laser pulse ( $\tau_{FWHM} \approx 2T_L$ ) with  $\varphi_{CEP} = 0$  has a dominant central cycle and two side ones, which are significantly ( $\sim 30\%$ ) weaker. **(d)** The same short pulse with  $\varphi_{CEP} = \pi$  has two equivalently strong cycles.

In case of  $\varphi_{CEP} = \pi$  there are only two cycles with a strong electric field while a pulse with  $\varphi_{CEP} = 0$  has three strong field cycles. Moreover, in this case the maximal photon energy of the central generated XUV pulse can be significantly higher than for the other two pulses because of the nonlinear dependence on the electric field. It allows to pick a single attosecond pulse by filtering the high energy photons, which are presented only in one of three generated pulses.

## 1.2 Driving laser and experimental setup

For realization of the method presented in the previous paragraph a multi-terawatt peak power laser system LWS-20 was used. Detailed description of this light source can be found in the

## Chapter1: Generation of XUV emission from oscillating plasma surface

corresponding article [12]. For the current work it is important to mention that the driving laser is based on *non-collinear* optical parametric amplification (NOPA), a four-wave mixing process that occurs when two beams – a weak broadband seed beam and a strong monochromatic pump beam with a shorter wavelength – overlap spatially and temporally in a nonlinear crystal. **Figure 1-5** explains the principle of NOPA.

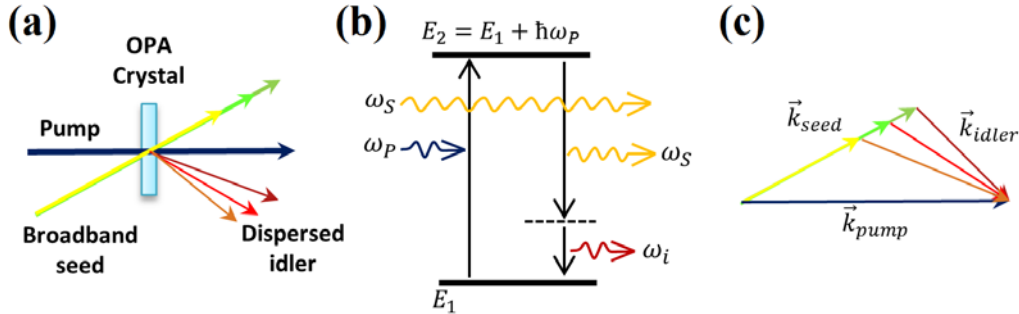


**Figure 1-5: Non-collinear OPA.**

(a) Geometry of the beams. Monochromatic pump and broadband seed beams overlap in a nonlinear crystal where the mixing process takes place and propagate further in their original directions. An additional beam called idler appears as the result of the interaction. The most commonly used crystals are BBO ( $\beta$ -barium borate), LBO (lithium triborate) and KDP (potassium dihydrogen phosphate), but there are others. (b) Energy diagram of the process. The energy of the absorbed pump photon is transmitted to a new seed photon and an idler photon. Since the seed beam is broadband, idler also contains different wavelengths. (c) Phase-matching condition. Wave-vectors ( $\vec{k} = 2\pi\vec{e}/\lambda = k\vec{e}$ , where  $\vec{e}$  is a unity-vector in the propagation direction) of all the beams are connected via  $\vec{k}_{pump} = \vec{k}_{seed} + \vec{k}_{idler}$ .

In LWS-20 amplification occurs in two stages, which for optimization of the efficiency within the whole bandwidth are split between two crystals each. One pair of the crystals is optimized (in terms of thickness and angles) for amplification of the seed within 580–700nm and uses 355nm pump beams, the second one – for 700–1020nm seed range and uses 532nm pump. Both pump beams are obtained from the same pump laser with the fundamental frequency  $\omega_p$  corresponding to  $\lambda_p = 1064nm$ : the second and third harmonics are generated in LBO crystals (details are presented in [26, p10–12]). The amplification scheme presented in **Figure 1-6** gives an idea of the seed and pump pulses energies.

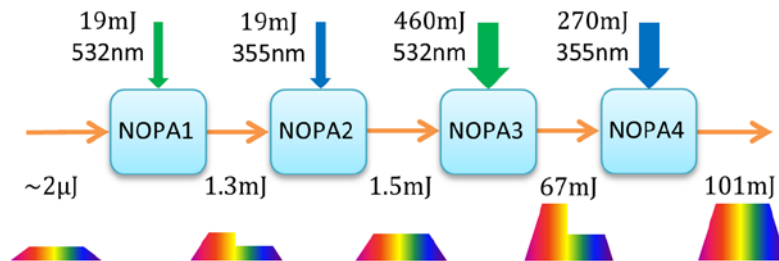


**Figure 1-6: LWS-20 amplification scheme.**

Seed beam sequentially propagated through 4 BBO crystals, where two parts of the spectrum are separately amplified. Crystals are pumped with the pump beams corresponding to the amplified spectral ranges.

## 1.2 Driving laser and experimental setup

Although LWS-20 can operate at 10Hz, its repetition rate was reduced down to 1Hz for reliable synchronization of the electronics and mechanics used in two laboratories located at two different floors and connected via a 20m vacuum beamline. **Figure 1-7** demonstrates the experimental scheme. Since the output beam of the driving laser has a random CEP, a small portion was sent into a stereo-ATI (above threshold ionization) phasemeter [27] that measures the CEP of each laser shot. It is necessary for further *CEP tagging* – sorting of the obtained experimental data accordingly to the laser CEP for detection of the correlations. The main part of the pulse is cleaned from unwanted prepulses by a plasma mirror in a way that was described in the previous paragraph. Afterwards the cleaned pulse is sent to the beamline and experimental chamber, but can be optionally steered to a home-made third-order auto-correlator [28] for the analysis of the temporal profile. This measurement is necessary to prove the absence of unwanted prepulses and long front-pedestals that could cause a premature ionization of the target surface and lead to a non-optimal plasma condition.

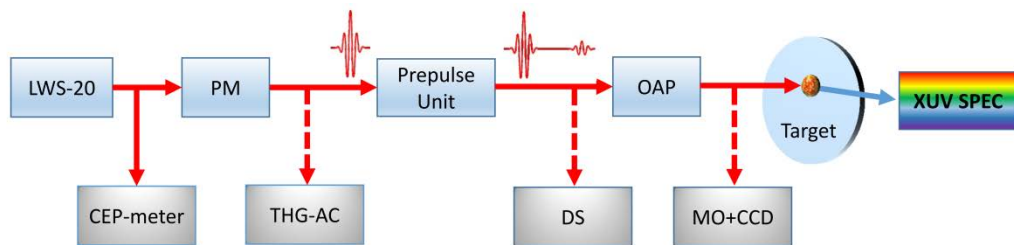


**Figure 1-7: Experimental setup scheme.**

LWS-20 delivers two-cycle laser pulses. A small portion of the beam is sent to a stereo-ATI phasemeter for measuring the CEP of each laser shot. The contrast of the main pulse is improved by a plasma mirror (PM) and characterized by a third-order auto-correlator (THG-AC). A controllable prepulse is produced in the prepulse unit. Afterwards, the on-target pulse duration is measured and optimized via *chirp-scan* technique [29]. For this purpose a home-made dazscope (DS) is used in combination with an acousto-optical modulator (*Dazzler*, Fastlite), which is a part of the driving laser. An off-axis parabolic mirror (OAP) tightly focuses the beam on the fused silica target that is translated after every shot. The generated XUV emission is reflected to a flat-field spectrometer where it is spatially separated from the fundamental beam. The focus quality is checked and optimized with the attenuated beam by replacing the target with a microscope objective (MO) and imaging it to a camera (CCD).

In the experimental chamber a controlled prepulse for optimization of the plasma scale length is created by inserting a small quarter-inch mirror in front of one of the steering mirrors. Detailed explanation of the prepulse generation is presented in **Appendix A**. This method allows to control the delay between the main pulse arrival and ionization of the surface within 0–12ps, which significantly affects the laser-plasma interaction. **Figure 1-8** represents the dependence of the XUV generation efficiency as a function of the prepulse delay, which unambiguously proves the efficiency and necessity of the manual plasma scale length control.

Before being sent to the target the beam ( $d \approx 50\text{mm}$ ) is tightly focused by an off-axis parabolic mirror ( $f = 60\text{mm}$ ), resulting in a main pulse focus size of  $1.3\mu\text{m}$ . Measurement of the beam size at focus is performed by imaging it to a camera via a microscope objective, which can be inserted in the beam by a motorized stage. Together with 5.1fs pulse duration (at intensity FWHM level) and 40mJ on-target energy left after all the losses such a focus size leads to the peak laser pulse intensity of  $1.3 \times 10^{20}\text{W}/\text{cm}^2$ . Due to some technical restrictions connected to the experimental chamber design the incident angle is slightly bigger than the optimum ( $55^\circ$  instead of  $45^\circ$ ), but according to simulations the difference is negligible.

## Chapter1: Generation of XUV emission from oscillating plasma surface

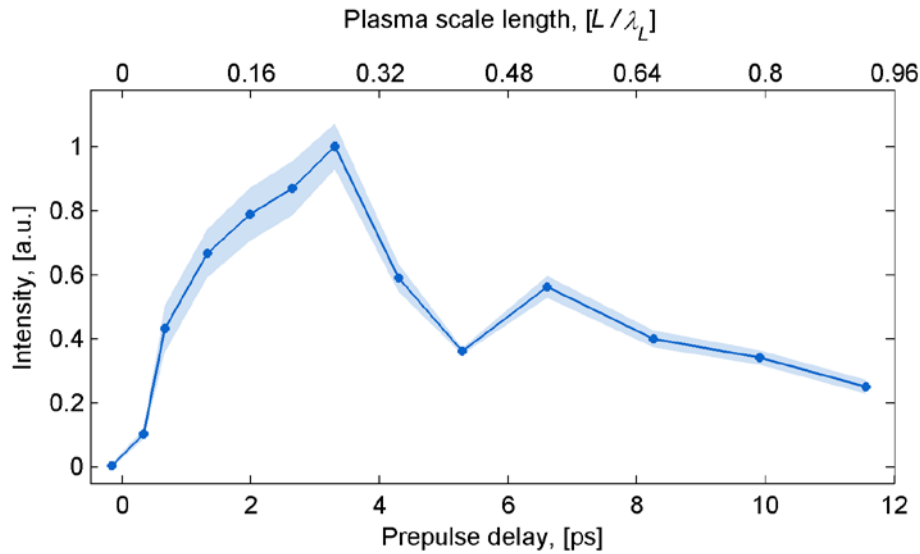


**Figure 1-8: Dependence of the measured XUV signal on the prepulse delay.**

Average integrated (within the spectral range of 16–100eV) intensity of the XUV signal measured at different prepulse values. Shaded area represents the standard error of the measurement. The assigned plasma scale length (upper x-axis) values are obtained from MEDUSA simulations [30].

The target is presented by a cylindrical piece of glass ( $\text{SiO}_2$ ) installed on a construction consisting of 3 motorized stages. The first linear stage provides translations in the direction of the incident beam for alignment to the beam focus. The second stage is rotational and is needed for translating to a new undamaged position after each laser shot. The third stage (also linear) serves for translation of the target along its surface which is necessary when the full rotation of the target has been performed. It is also used for replacing the target with the microscope objective. **Figure 1-9** shows a used target and explains its rotation and translation principle.

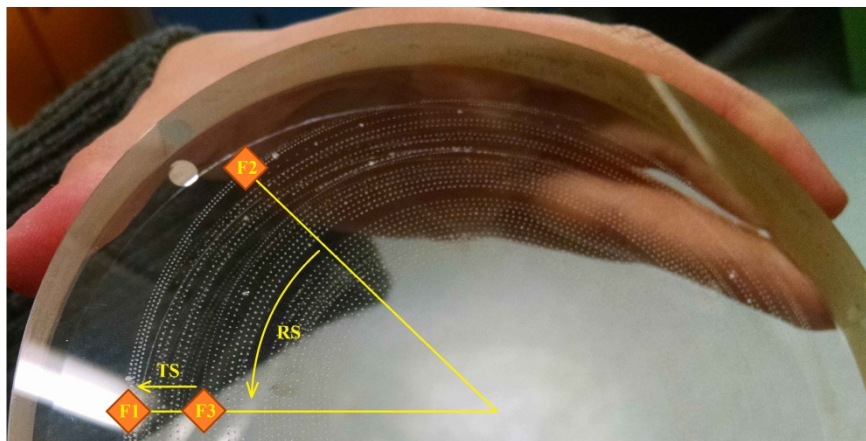


**Figure 1-9: Used  $\text{SiO}_2$  target.**

Small white dots are the damages (craters) on the surface which appear after the ionization. After each shot the target is revolved by the rotational stage, what is schematically shown with an arrow RS: it is a radial rotation that brings point F2 to the position of F1, corresponding to the fixed focus of the laser beam. When the full circle is filled with craters, the translation stage changes the radius (shown with arrow TS, which brings the point F3 to the position of F1). The absolute scale of both movements in the figure is strongly exaggerated for better visibility. Real rotation angle depends on the current circle radius and corresponds to  $\sim 3\text{mm}$  distance between any two consecutive shots. The same distance is used as a translation step for shifting to another circle. The area within  $\sim 20\text{mm}$  from the edge is used for fixation of the target in the rotational stage and thus cannot be used. Total amount of shots for a single target having the diameter of 150mm is  $\sim 30000$ .

## 1.2 Driving laser and experimental setup

The reflected beam is sent to a home-made spectrometer, where the fundamental laser frequency is spatially separated from the generated XUV pulses and blocked. Each measured spectrum is assigned to the laser pulse CEP. An example of such two spectra corresponding to different CEP values is presented in **Figure 1-10a**. Strong modulations in the spectrum – so called *harmonics* – appear as the result of the interference between several generated pulses that reach the detector at different times. Sorting of the measured harmonics spectra according to the laser pulse CEP (**Figure 1-10b**) reveals an unambiguous correlation, which matches well to the result of simulations. The origin of such behavior can be explained via interferometric analysis of the measured spectra that is presented in the following chapter.

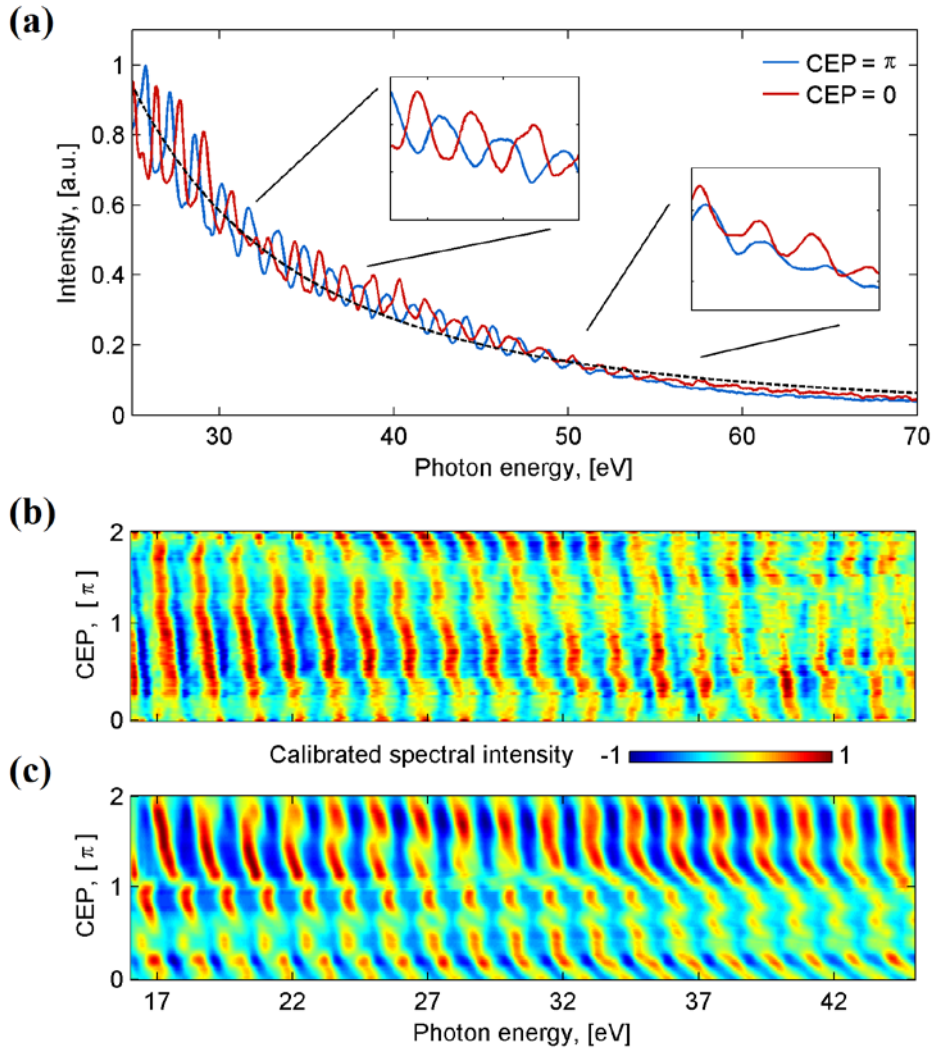


**Figure 1-10: Measured harmonics spectra.**

(a) Example of two spectra measured at different CEP. Black dashed line shows expected from the theory [31] intensity scaling law  $I(\omega) \sim \omega^{-8/3}$  that agrees well with the measured spectra. (b) Set of measured spectra sorted according to the laser pulse CEP.  $\tau_{pp} \approx 1.67ps \leftrightarrow L \approx 0.13\lambda_L$ . (c) Corresponding simulations. In both cases spectral intensity is calibrated for better visualization: minimum and maximum values within the whole spectral range are normalized to -1 and 1 respectively.

## **Chapter1: Generation of XUV emission from oscillating plasma surface**

# Chapter 2

## Recognition of isolated attosecond pulses

The second chapter is dedicated to analysis of the measured harmonics spectra via a novel interferometric approach. First of all the conventional spectral interferometry is described, afterwards the concept is extended to the case of three interfering pulses. Corresponding numerical model demonstrates the underlying mathematical justification of the suggested treatment as well as its usability boundaries. The second section demonstrates the application of this method to the measured XUV spectra generated at different CEP of the driving laser. Successful temporal reconstruction of the generated pulse trains allowed to define the optimal CEP range that results in the generation of a well-isolated attosecond pulse.

### 2.1 Spectral interferometry

Conventional *spectral interferometry* (SI) is a method of complete temporal characterization of an unknown pulse, which is based on the analysis of the spectrum that presents the result of interference between this unknown pulse and an already characterized reference pulse.

**Figure 2-1** explains the measurement and analysis principle.

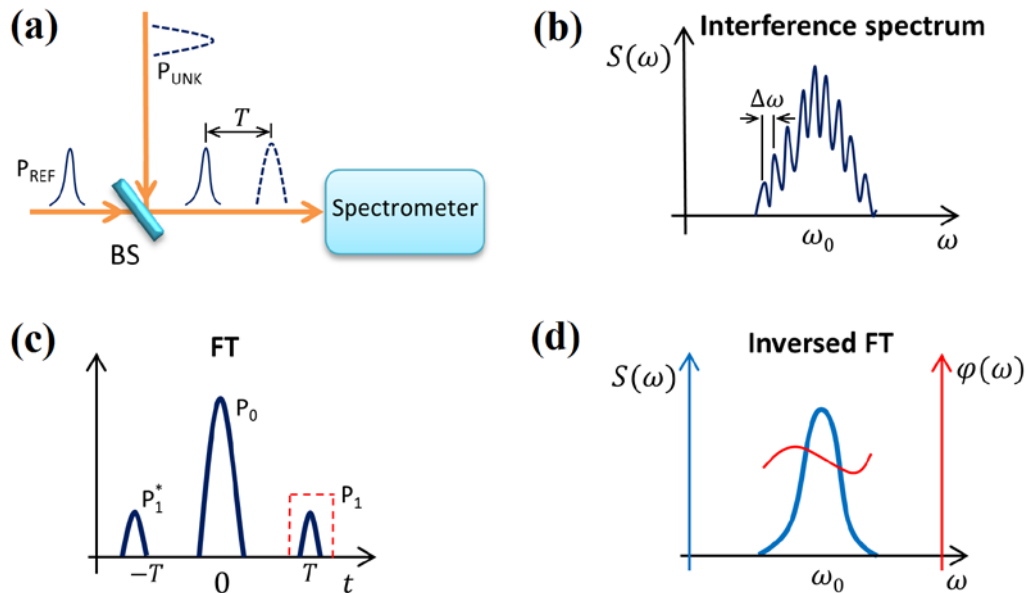


**Figure 2-1: Conventional spectral interferometry.**

(a) Measurement scheme. The unknown pulse is sent to the spectrometer together with the reference pulse. (b) Measured resulting spectrum  $S_{SI}$  contains frequency modulations  $\Delta\omega$  that depend on the delay  $T$  between the measured and reference pulses. (c) Fourier transformation of the measured spectrum. Dashed line shows the temporal gate function for further inversed FT (d) Inversed FT of the gated peak  $P_1$  gives the coupled spectrum  $S(\omega) = \sqrt{S_{REF}(\omega)S_{UNK}(\omega)}$  and the phase difference  $\varphi(\omega) = \varphi_{REF}(\omega) - \varphi_{UNK}(\omega)$ .

## Chapter 2: Recognition of isolated attosecond pulses

The resulting spectrum  $S_{SI}$  (subfigure **b**) contains the information about the spectral phase and intensity of the unknown pulse, which can be extracted via simple Fourier analysis. The Fourier transformation (FT) of such a spectrum, presented on subfigure (c), consists of three well distinguishable peaks. Zero-peak  $P_0$  contains only the information about the slow changing envelope of the spectrum  $S_{SI}$ , while peak  $P_1$  located at falls-time  $t_1 = T$  (and also its copy located at  $t = -T$ ) defines the modulation in the spectrum and encrypts the phase and intensity of the interfering pulses. In order to derive this information inversed Fourier transform should be applied to peak  $P_1$ . Applying a temporal gate function (for example in a shape of Planck-taper window [32]) allows for separation of  $P_1$  from the zero-peak and unwanted noise. The resulting *coupled* spectrum and phase (subfigure **d**) unambiguously define the relation between the individual spectra and phases of the unknown and reference pulses. The advantage of SI approach is a possibility to completely characterize the temporal structure of an unknown pulse based on a single measurement of the resulting spectrum  $S_{SI}$ . However it is only possible – and this is the main disadvantage of the method – if there is a source of reproducible and characterized (in terms of spectral phase and intensity) reference pulse with a comparable duration and spectral bandwidth.

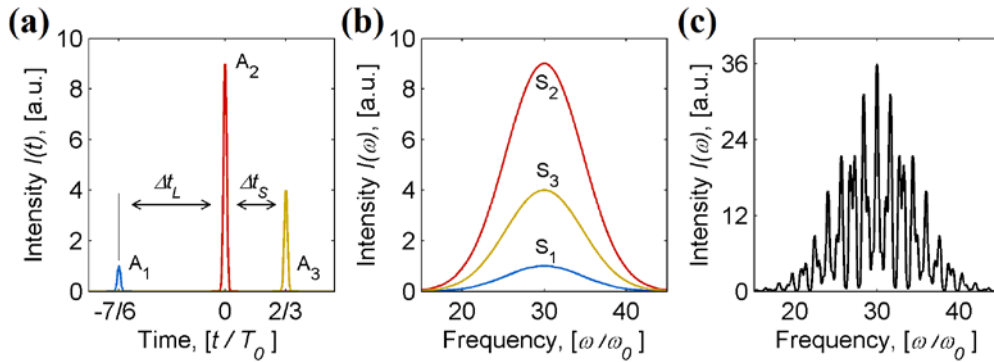


**Figure 2-2: Numerical model of interference of three pulses.**

(a) Temporal structure of a non-equidistant pulse train.  $\Delta t_L$  and  $\Delta t_S$  are long and short delays between the pulses. Full duration is  $\Delta t_F = \Delta t_S + \Delta t_L$  (b) Individual spectra of the pulses. (c) Resulting interference spectrum  $S_{SI}$ .

A similar approach can be extended to a pulse train consisting of three pulses. **Figure 2-2** demonstrates the corresponding numerical model. Three non-equidistant pulses with individual spectra  $S_1$ ,  $S_2$  and  $S_3$  have non-zero components within the same spectral range. Resulting spectrum of such a pulse train  $S_{SI}$  obtains specific harmonics-like modulations, whose depth and wavelength depend on the individual spectra and phases of the interfering pulses. If it is known in advance, that the spectral phase of each pulse in the train is flat or contains only a linear component, which is also called *group delay* (GD), but does not contain any higher order dispersion, the resulting interference spectrum contains enough information for a complete temporal reconstruction of the original pulse train. Mathematically this requirement can be expressed as

$$\frac{\partial^k \varphi}{\partial \omega^k} \equiv 0 \quad \text{for} \quad k \geq 2 \quad (2.1)$$

$\varphi(\omega) = A\omega + const$ , where  $A$  is the GD.

## 2.1 Spectral interferometry

**Figure 2-3a** shows the corresponding Fourier transformation. Similar to the traditional SI, it consists of a zero-peak  $P_0$  and three peaks encoding the pairwise interference of all three pulses in the train. Inversed Fourier transformation of each peak (within the corresponding temporal gate) gives three coupled spectra and phases (subfigures **b** and **c**). Distinguishing of the pulses, whose interference is presented by each of three peaks, is possible via comparison of the delays in the pulse train.

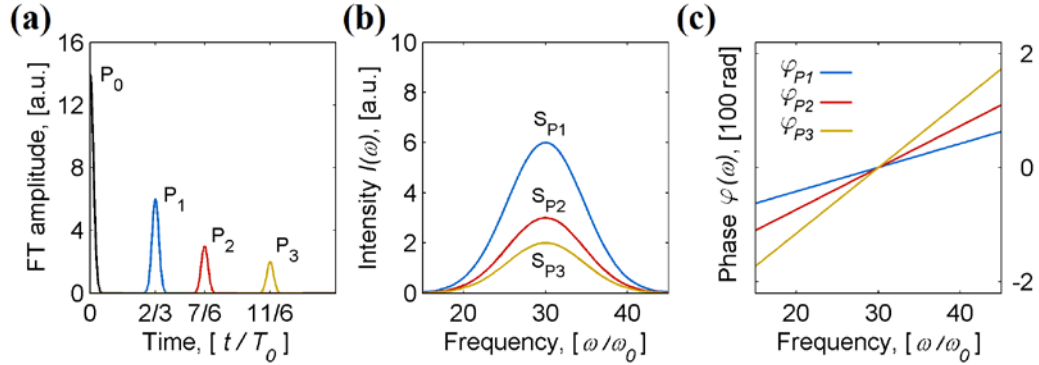


**Figure 2-3: Fourier analysis of the interference spectrum.**

(a) Fourier transformation of the interference spectrum  $S_{SI}$ . (b) Pairwise coupled spectra of individual pulses. (c) Coupled phases representing pairwise phase differences of individual pulses.

These delays are contained in the corresponding phase differences, presented by the coupled phases  $\varphi_{P1}$ ,  $\varphi_{P2}$  and  $\varphi_{P3}$ . However the delay between any two pulses in the train is also imprinted in the position of the peak, representing the interference of these two pulses. Thus if  $\Delta t_L$  and  $\Delta t_S$  are the long and the short delays between the pulses in the train (**Figure 2-2a**) and  $\Delta t_F = \Delta t_S + \Delta t_L$  is the full pulse train duration, then the “false” time coordinate of the peaks in the Fourier transform satisfy the following relations:

$$\begin{aligned}
 t_{P1} &< t_{P2} < t_{P3} \\
 t_{P1} &\equiv \Delta t_S \\
 t_{P2} &\equiv \Delta t_L \\
 t_{P3} &\equiv \Delta t_F = \Delta t_S + \Delta t_L \equiv t_{P1} + t_{P2}
 \end{aligned} \tag{2.2}$$

which means that peak  $P_3$  always represents the interaction of the first and the last pulses in the train, while peaks  $P_1$  and  $P_2$  correspond to the interaction of the central pulse with the side ones. However, the direction of the time axis cannot be unambiguously defined: the first and the last pulses can be swapped around the central one with the corresponding delays and the resulting FT (**Figure 2-3a**) stays the same. Thus the final result of the reconstruction can be inversed in time. In case of the experimental data analysis this ambiguity can be resolved by comparison with the simulations. The properties of the plasma are different before, during and after the interaction with the laser pulse, which allows to distinguish the first and the last generated XUV pulses.

Since each peak in the Fourier transform is assigned to a pair of interfering pulses, relations between the individual and the coupled spectra and phases can be unambiguously defined by the following equations:

## Chapter 2: Recognition of isolated attosecond pulses

$$\begin{aligned}
 P_1: \quad S_{P1} &= \sqrt{S_2 S_3} \\
 \varphi_{P1} &= \varphi_2 - \varphi_3 = \Delta\varphi_{23}
 \end{aligned} \tag{2.3}$$

$$\begin{aligned}
 P_2: \quad S_{P2} &= \sqrt{S_1 S_2} \\
 \varphi_{P2} &= \varphi_1 - \varphi_2 = \Delta\varphi_{12}
 \end{aligned} \tag{2.4}$$

$$\begin{aligned}
 P_3: \quad S_{P3} &= \sqrt{S_1 S_3} \\
 \varphi_{P3} &= \varphi_1 - \varphi_3 = \Delta\varphi_{13}
 \end{aligned} \tag{2.5}$$

These system of equations can be resolved relatively to the individual spectra, giving  $S_1 = S_{P2}S_{P3}/S_{P1}$ ,  $S_2 = S_{P1}S_{P2}/S_{P3}$  and  $S_3 = S_{P1}S_{P3}/S_{P2}$ , but is underdetermined relatively to the individual phases. Here requirement **2.1** reveals its meaning. According to **Figure 2-3c** all three coupled phases are linear and have no higher order dispersion. But  $\varphi_{P3} = \varphi_{P1} + \varphi_{P2}$ , which means that there are only two independent equations for three unknown phases and the individual phases cannot be derived. However the absolute phase is not important for the reconstruction of the temporal structure of the pulse train. Translation property of the Fourier transformation makes the reconstruction insensitive to adding a constant phase or a constant *group delay* (GD), which is the first derivative of the phase  $\frac{\partial\varphi(\omega)}{\partial\omega}$  – it only affects the absolute position of the pulse train on the time axis, but does not change the delay between the pulses. So if at least one of them fulfills requirement **2.1**, all the other pulses automatically also fulfill it, because the phase differences  $\Delta\varphi_{12}$ ,  $\Delta\varphi_{23}$  and  $\Delta\varphi_{13}$  are linear. Therefore one of the unknown phases can be considered equal to zero (since any GD and phase can be added or subtracted) and the other two will be defined by equations **2.3–2.5**. Though it might look like an artificial mathematical assumption, according to the numerical simulations (presented in the supplementary materials to [14]) generated XUV pulse trains – at least in the experiment, described in paragraph **1.2** – should fulfill even stronger requirement: the spectral phase of the individual pulses is not only free of high order dispersion, but is almost perfectly flat and close to zero within the whole spectral bandwidth.

Thus the temporal structure of the pulse train can be reconstructed by inversed Fourier transformation of the complex interference spectrum  $S_{SI}^*$  that is defined by equations **2.6–2.7**.

$$S_{SI}^* = S_1 + S_2 e^{i(-\varphi_{P2})} + S_3 e^{i(-\varphi_{P3})} \tag{2.6}$$

$$I(t) \equiv iFFT\{S_{SI}^*\} \tag{2.7}$$

Here the phase of the first pulse  $\varphi_1$  is chosen to be zero and the other two phases are expressed via the calculated phase differences according to equations **2.3–2.5**. But as it was explained above, any of three phases can be defined as zero – it will only translate the reconstructed pulse train along the time axis:  $I(t) \rightarrow I(t - t_0)$ . Comparison of the reconstructed temporal profile  $I(t)$  and individual spectra  $S_1$ ,  $S_2$  and  $S_3$  with the original ones is shown in **Figure 2-4**.

## 2.2 Analysis of the measured XUV spectra

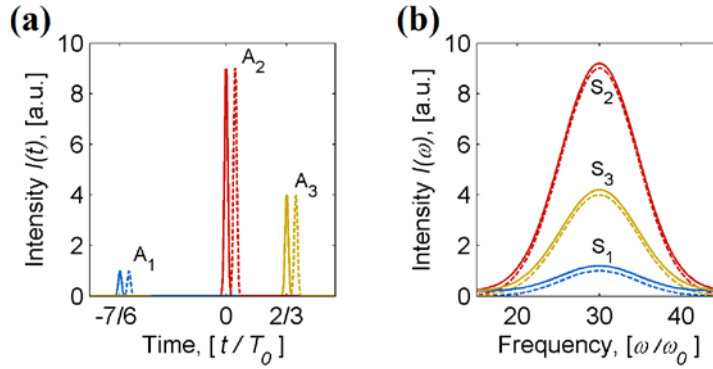


**Figure 2-4: Comparison of the reconstructed and the original data.**

(a) Temporal profile of the pulse train. (b) Individual spectra. For both plots solid lines present the original data, dashed lines – result of reconstruction. Dashed lines are demonstrated with manually introduced displacement (vertical for spectra and horizontal for pulse train) for better visualization.

Demonstrated interferometric treatment can be also applied to the harmonics spectra presented in **Figure 1-10**. In case of simulations such a reconstruction – being based purely on the analysis of the obtained spectra– matches very well with the full results of simulations, which among other data also contain the temporal profile of the generated pulse train and the individual spectra of the pulses (corresponding comparison can be found in the supplementary materials to original paper [14]). Analysis of the measured XUV spectra is presented in the following paragraph.

## 2.2 Analysis of the measured XUV spectra

Experimental data shown in **Figure 1-10** are measured at  $L \approx 0.13\lambda_L$  and demonstrate a clear dependence on the driving pulse: generated spectra are presented by well distinguishable harmonics with an almost constant period and slowly changing, CEP-dependent peaks position. The reason of such a clear pattern is the small delay between the prepulse and the main pulse ( $\tau_{PP} \approx 1.67fs$ ), which leads to high density of the plasma cloud. Dense plasma experiences less motion during interaction with the laser pulses, what results in almost equal delays between the generated pulses. The influence of the plasma motion on the delays is explained in the next paragraph.

### 2.2.1 Interference of two pulses

The simplest example for demonstration of the interferometric treatment is a spectrum with a clear periodic harmonic structure without any additional modulations. Such a spectrum (measured at  $L = 0.25\lambda_L$  and  $\varphi_{CEP} \approx 0$ ) and the corresponding analysis is shown in **Figure 2-5**. According to the simulations for this CEP (in the given experimental conditions, i.e. intensity in the focus and plasma scale length) generated pulse train should consist of two dominant central pulses with almost equivalent intensity and two weak side pulses. Due to the nonlinear nature of the emission process, stronger pulses also have much higher maximum photon energy. It means that above some photon energy threshold only these two dominant pulses define the observed spectrum.

## Chapter 2: Recognition of isolated attosecond pulses

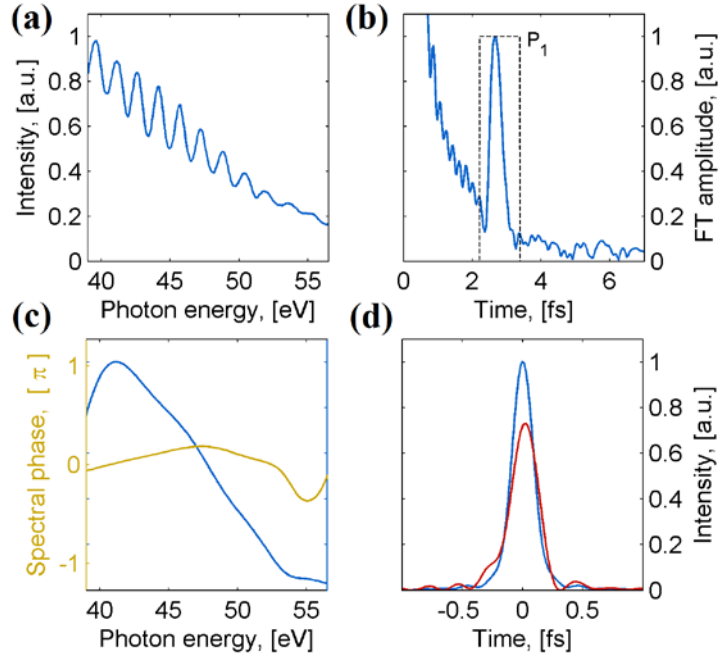


**Figure 2-5: Spectral interferometry with two attosecond pulses.**

(a) Measured spectrum.  $\varphi_{CEP} \approx 0$ ,  $L = 0.25\lambda_L$ . (b) Corresponding Fourier transformation. Dashed line shows the gating window. (c) Coupled spectrum  $S_{P_1}$  (blue) and phase  $\varphi_{P_1}$  (orange), obtained from the inversed FT of peak  $P_1$ . GD (linear component) of the phase is subtracted for better demonstration of the high-order component. Y-axis scale and ticks of the spectrum match the y-axis of the next subplot. (d) Fourier limited (blue) and phase-affected (red) pulses, corresponding to  $S_{P_1}$  and  $\varphi_{P_1}$ . Time delay between the pulses (contained in phase  $\varphi_{P_1}$ ) is compensated for easier comparison.

Analysis of the demonstrated spectrum leads to a conclusion that exactly corresponds to the simulations. Fourier transform (**Figure 2-5b**) contains only a single peak that rises above the noise level and is well separated from a strong zero-peak – such a structure in Fourier domain is typical for conventional spectral interferometry (**Figure 2-1c**), i.e. represents the interference between two pulses. Almost zero phase difference  $\varphi_1 - \varphi_2 = \Delta\varphi_{12} \equiv \varphi_{P_1}$  also matches well to the simulations, which predict the phase of all the generated pulses to be close to zero (and thus their difference too) regardless of the driving laser CEP.

Taking into account, that in the simulations two dominant pulses always have comparable intensity – otherwise there is a third intense pulse, that leads to presence of an additional peak in FT – coupled spectrum  $S_{P_1}$  can be used for approximation of the individual spectra  $S_{P_1} = \sqrt{S_1 S_2} \approx S_1 \approx S_2$ . Based on this spectrum the individual temporal profiles of both pulses can be reconstructed. **Figure 2-5d** shows such temporal profiles for a perfectly zero phase (Fourier limited) and affected by close-to-zero phase  $\varphi_{P_1}$ , which should have a comparable pulse-distorting effect as the real individual (also close-to-zero) phases. The delay between the pulses  $T_{12}$  is imprinted in phase  $\varphi_{P_1}$  and can be directly extracted from the position  $t_{P_1}$  of peak  $P_1$ . Thus above 39eV the generated pulse train can be well approximated by two almost equivalent pulses at temporal distance of 2.7fs with the profiles similar to the phase-affected reconstruction (red curve on subfigure **d**).

## 2.2 Analysis of the measured XUV spectra

Notably, the delay between the pulses  $T_{12}$  is 150as longer than the laser period  $T_L = 2.55fs$ . This difference can be explained by so called *plasma denting*. According to the simulations plasma is being pushed by the intense laser field and different pulses are generated at different spatial coordinates. It leads to a difference in the propagation time (to the detector) that adds to the laser period and affects the interference. Analysis of this delay for different driving laser CEP leads to an important conclusion about motion of the plasma surface that is effectively being probed by the generated XUV pulses. Corresponding results are presented in [14].

### 2.2.2 Interference of three pulses

In terms of generation of an isolated attosecond pulse, two equivalent pulses present the least suitable configuration of the pulse train. Since both pulses have a comparable intensity and maximum photon energy, it is impossible to filter out one of them using a high-pass filter. From this point of view exactly opposite pulse train structure with a strong central pulse and weak side ones is of a high interest since the strongest central pulse can be separated by using a proper filter, as it is shown in **Figure 1-1**. According to the simulations under given experimental conditions (pulse duration, light intensity and plasma scale length) such pulse trains are generated at  $\varphi_{CEP} \approx \pi$ . **Figure 2-6** demonstrates the analysis of the corresponding spectrum, which looks significantly more complicated than in case of two pulses interference. Noticeable beating in the spectrum – an additional slow modulation of the harmonics amplitude – indicates the presence of two different delays between three pulses in the train. As expected from the numerical model, Fourier transformation contains three peaks with different amplitudes and falls-time coordinates, which match equations 2.2. Remarkably, for some plasma conditions the generated pulses can be almost equidistant ( $\Delta t_S \approx \Delta t_L \approx \Delta t_F/2$  according to **Figure 2-2a**). In this case the beating in the spectrum is not so pronounced (or completely absent) and peaks  $P_1$  and  $P_2$  in FT merge into a single peak, which makes the complete reconstruction impossible. It usually occurs when the laser pulse arrives too early after the ionization and the plasma is too dense<sup>1</sup>. For most of the other cases the interferometric approach works well when the XUV signal is measured with a good accuracy. It means that the spectral bandwidth and resolution as well as the signal-to-noise ratio of the spectrometer should be good enough to distinguish the peaks in the FT transform from each other and from the noise.

**Figure 2-6c** shows the individual spectra of the pulses, calculated according to equations 2.3–2.5. As the simulations predicted, the central pulse significantly surpasses the side ones. For a complete reconstruction of the pulse train and comparison of the peak intensities, the phase of one of the pulses should be assigned zero and the other two phases should be recalculated from the coupled phases  $\varphi_{P1}$ ,  $\varphi_{P2}$  and  $\varphi_{P3}$ (subfigure **d**).

---

<sup>1</sup> The data presented in **Figure 1-10** correspond to such a case. Because of the short prepulse delay  $\tau_{PP} \approx 1.67ps$  the plasma stays rigid ( $L \approx 0.13\lambda_L$ ) and does not bend a lot while interacting with the laser pulse. As the result, generated pulse trains are almost equidistant and their spectra are presented by regular harmonics with almost no beating, which allows to distinguish a clear dependence of the harmonics wavelength on the laser pulse CEP. For bigger prepulse delays the plasma is softer and its denting is stronger, which leads to a bigger difference between the short ( $\Delta t_S$ ) and the long ( $\Delta t_L$ ) delays. Resulting spectra are strongly modulated and the corresponding CEP-sorted patterns (can be found in the supplementary materials to [14]) are much more complicated and are not always recognizable.

## Chapter 2: Recognition of isolated attosecond pulses

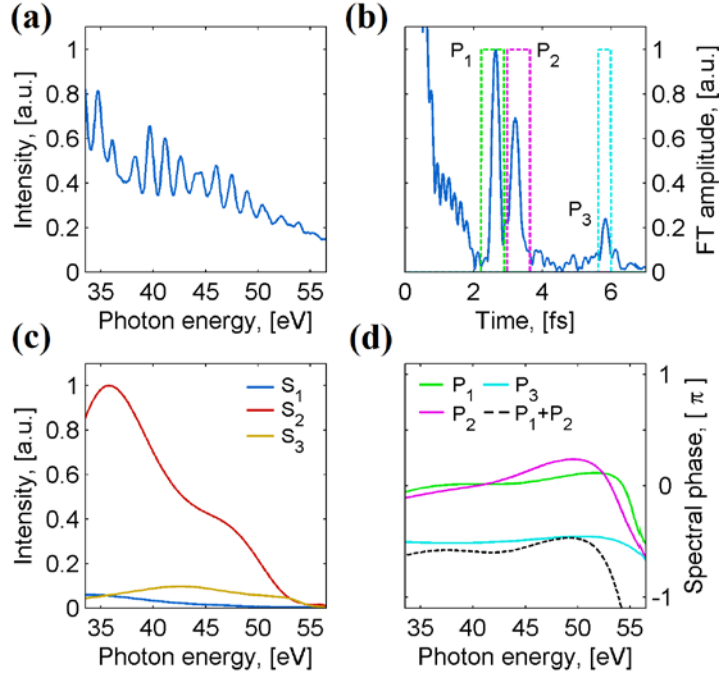


**Figure 2-6: Spectral interferometry with three attosecond pulses.**

(a) Measured spectrum.  $\varphi_{CEP} \approx \pi, L = 0.5\lambda$ . (b) Corresponding Fourier transformation. Dashed lines shows the gating windows of each peak. (c) Individual spectra of the pulses reconstructed according to equations 2.3–2.5. (d) Coupled phases  $\varphi_{P_1}$ ,  $\varphi_{P_2}$  and  $\varphi_{P_3}$  with the subtracted GD components. Black dashed line shows the sum  $\varphi_{P_1} + \varphi_{P_2}$  that matches well to  $\varphi_{P_3}$ . A  $-\pi/2$  displacement is added to the lines corresponding to  $\varphi_{P_3}$  and  $(\varphi_{P_1} + \varphi_{P_2})$  for better visibility.

Without the GD component they all are very close to zero within the spectral range containing any significant intensity, what makes the used zero-approximation quite legitimate. For the worst case estimation of the central-to-side pulses peak intensity ratio the phase of the third pulse in this train should be assigned zero<sup>1</sup>, so equation 2.6 takes the following form:

$$S_{SI}^* = S_1 e^{i\varphi_{P_3}} + S_2 e^{i\varphi_{P_1}} + S_3 \quad (2.8)$$

Inversed Fourier transformation of such a complex interference spectrum gives the temporal structure of the pulse train within the presented spectral range (**Figure 2-7a**). Here the peak intensity of the central pulse (as well as the contained energy) is at least 6 times higher than for the side pulses, what already allows to consider such a pulse train as a single attosecond pulse for investigation of strongly nonlinear processes like multiphoton absorption (e.g. like in [33]).

<sup>1</sup> According to the individual spectra (**Figure 2-6c**), the third pulse is stronger than the first one and weaker than the central one:  $S_2 \geq S_3 \geq S_1$  within the presented spectral range. Since the spectra are known, the peak intensity depends on the minor high-order dispersion of the individual phases, among which one should be pure zero and two other are not, though also quite flat. Assigning a non-zero phase to any two pulses slightly reduces their peak intensity comparing to the Fourier limit, while the third pulse stays Fourier-limited. Thus for the worst case estimation of the central-to-side pulses peak intensity the zero-phase has to be assigned to the strongest of the two side pulses, which in the given example is the third one.

## 2.2 Analysis of the measured XUV spectra

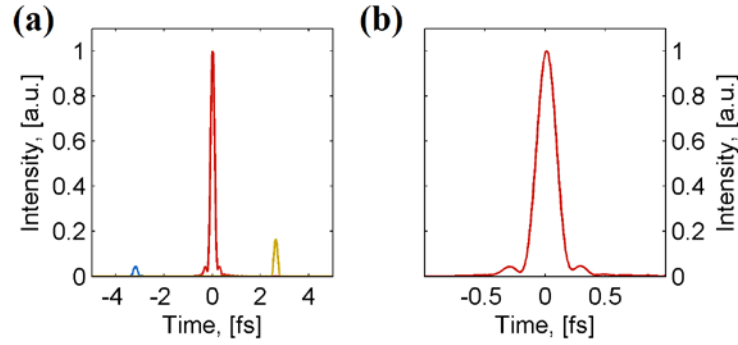


**Figure 2-7: Reconstructed pulse train.**

(a) Full temporal structure of the pulse train (corresponding to  $\varphi_{CEP} \approx \pi$ ,  $L = 0.5\lambda_L \leftrightarrow \tau \approx 6.4ps$ ). Isolation degree of the central pulse is at least 6. (b) Temporal structure of the central pulse only. Estimated duration  $\tau_{FWHM} \approx 190as$ .

It is important to mention, that according to this reconstruction the central pulse has a near zero phase within the presented spectral range, where its duration ( $\tau_{FWHM} \approx 190as$ ) allows to call it *attosecond* pulse. However the phase information for the lower photon energy is missing. Though simulations predict the phases of all the pulses in the train to be close-to-zero within the whole spectral range, it cannot be proved by such analysis. So hypothetically a strong high-order dispersion around 10–20eV can significantly stretch the pulse and its duration within the full spectral range can exceed one femtosecond. Thus spectral interferometry alone does not provide enough information about the real duration of the pulses as they were generated – it only tells that the analyzed spectra support attosecond duration. In order to legitimate their sub-femtosecond duration low energy part of the spectrum should be physically cut by some filters corresponding to the analyzed spectral range. For example *Mg* or *Al* foils have quite sharp-edged transmission band within 10–50eV and 18–72eV respectively. For higher photon energies other materials like *Zr* (80–200eV) or *Cu* (400–1000eV) can be used.

The analysis demonstrated in **Figures 2-6** and **2-7** – with three well-defined peaks in the Fourier transform – is the most full and representative example of harmonics interferometric treatment and the corresponding reconstruction of the XUV pulse train temporal structure. However this approach can be also extended to some less determined cases. According to the simulations there is a CEP range, where the *isolation degree* – the relation between the peak intensity of the strongest pulse in the train and the other pulses – is even higher. Corresponding measured spectrum ( $\varphi_{CEP} \approx 11\pi/6$ ) is shown in **Figure 2-8a**. The harmonics amplitude there is so low, that without the interferometric analysis such a spectrum can be hardly distinguished from the noise signal corresponding to a *bad shot* – when the laser is focused on a damaged or distorted part of the glass surface and the generated plasma expands chaotically and does not properly interact with the main laser pulse.

Fourier transformation of such a spectrum also looks different. There are only two recognizable peaks with amplitudes that are just 3–5 times stronger than the noise level. For comparison, this ratio is about 15–20 for the spectra with strongly pronounced harmonics modulations. However these two peaks unambiguously confirm the existence of three pulses in the train.

## Chapter 2: Recognition of isolated attosecond pulses

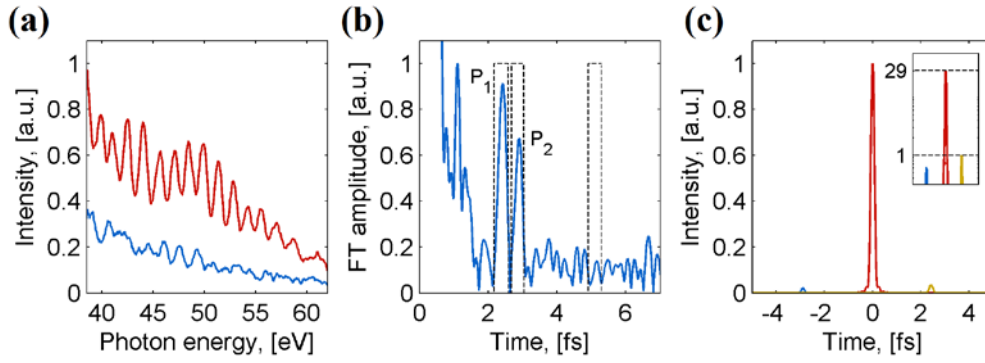


**Figure 2-8: Highly-isolated attosecond pulse.**

(a) Weakly modulated XUV spectrum (blue curve, measured at  $\varphi_{CEP} \approx 11\pi/6$ ,  $L = 0.5\lambda$ ) in comparison with well pronounced harmonics (red curve, measured at  $\varphi_{CEP} \approx \pi$ ,  $L = 0.5\lambda$ ) (b) Fourier transformation of the weakly modulated spectrum. (c) Corresponding temporal structure with the underestimated intensity of the central peak. Inset shows the intensity in a logarithmic scale.

The third peak itself is only needed for calculation of the individual spectra of the pulses, because the phase differences can be extracted from the first two peaks. Moreover, according to equations 2.3–2.5 and general properties of the FT, the amplitudes of peaks  $P_1$  and  $P_2$  relatively to  $P_3$  define the energy content (and also the peak intensity, if the phases are near zero) ratio between the central and the side pulses in the train. This dependence can be expressed via the coupled spectra

$$\frac{S_2}{S_3} = \left(\frac{S_{P2}}{S_{P3}}\right)^2 \quad \frac{S_2}{S_1} = \left(\frac{S_{P1}}{S_{P3}}\right)^2 \quad (2.9)$$

which appear as the inversed FTs of the corresponding peaks. Thus the stronger the first two peaks in the Fourier transform relatively to the third one, the higher the ratio between the corresponding coupled spectra, which in turn means higher isolation degree.

Based on this it is possible to make some approximate reconstruction using the noise level signal at the corresponding falls-time position of peak  $P_3$  (third dashed window on subfigure b). In this case the calculated individual spectra of the pulses as well as their peak intensities will be incorrect in the final temporal reconstruction of the pulse train. But according to equations 2.9 the isolation degree will only be underestimated, because peak  $P_3$  and hence the calculated coupled spectrum  $S_{P3}$  are overestimated. Such an approximate reconstruction (subfigure c) shows that the isolation degree of the central pulse is at least 29, what allows considering it as a single well-isolated attosecond (with respect to the specified spectral range) pulse.

## Prospect:

# A route towards an ideal source of isolated attosecond pulses

Generation of XUV emission from solid surfaces is a promising method of ultra-short pulses creation. Though the relativistic laser-plasma interaction is demanding to the driving light sources, modern lasers have already reached the parameters that allow for generation of intense isolated attosecond pulses. Numerical investigations [24] predicted generation of attosecond pulses with the energy of  $\sim 100\mu\text{J}$  for the light intensity ( $\sim 10^{20}\text{W}/\text{cm}^2$ ), which the state-of-the-art few-cycle laser system LWS-20 can provide.

Unique combination of the high output pulse energy and two-cycle duration ( $\tau = 5.1fs = 2T_L$ , on-target energy  $E_{target} \approx 40mJ$ ) led to a stable generation of the XUV emission up to 100eV. Tagging all the generated XUV spectra with the measured carrier-envelope phases of the driving laser pulses<sup>5</sup> revealed a clear correlation between the shape of the electric field and the resulting XUV pulse train structure manifested in the harmonics pattern. A novel spectral interferometry based approach, developed during the analysis of the experimental data, allowed to extract an important information related to the plasma motion and the birth of the XUV pulses. Supported by the numerical simulation, this method allowed to reconstruct the temporal structure of the generated pulse trains based on their spectra. This in turn enabled the conclusion regarding the optimal CEP that leads to an almost perfectly isolated attosecond pulse: XUV pulse train generated at this condition is presented by a dominant central pulse and two side pulses, whose intensity is about 30 times lower. Such an isolation degree is already enough for almost all the applications, but the side pulses can be also filtered out by usage of special filters if it is necessary for some certain experiments.

However a routine and user-friendly usage of relativistically oscillating plasma as a source of attosecond pulses requires a lot of further development. First of all, the CEP of the driving lasers should be stable and adjusted to the range, which for a given experimental condition – setup geometry, light intensity and plasma scale length – corresponds to the best isolation. Existence of weaker OPCPA based system with stable CEP [34, 35] means that the implementation of the corresponding technologies in LWS-20 or other high-intensity few-cycle laser systems can be realized in the nearest future. Another important improvement that is necessary for convenient application is the increase of the attosecond pulses repetition rate to at least a kilohertz level – of course, without the energy reduction.

This implies investigation and development in three different directions. One of them is a pure engineering and is connected to the limited amount of laser shots per target sample. Estimation

---

<sup>5</sup>At the time of the experiment, i.e. year 2016, LWS-20 system had a random (non-stabilized) carrier-envelope phase. The current state is unknown since the author has changed the research group and direction

### Chapter 3: Thin-disk based high power pump laser

of at least 1kHz repetition rate means that a single glass target is consumed ( $N_{shots} \approx 30000$ ) within 30 seconds, afterwards a long and complicated replacement procedure is necessary. Potential and promising solution of this problem is the usage of thin polymer (PMMA for example) foils as targets [36]. As the prove of principle XUV emission with the energy up to 100eV was obtained from a  $1\text{cm}^2$  piece of  $175\mu\text{m}$  PMMA foil glued to the surface of the glass target. Thus, properly designed mechanics should be able to feed the rolled foil to the focus, providing the fresh surface before each laser shot throughout hours of experiments. Of course, several key requirements like surface quality or stability within the focus z-coordinate have to be satisfied, but all this can be rightfully considered as engineering problems in comparison with the main, truly scientific problem, namely the limited average power of the driving lasers.

At the moment maximal demonstrated average power of the OPA based laser systems is limited with 100W and corresponds to hundreds-kilohertz low pulse energy systems [37, 38]. High energy lasers with the pulse energies of  $\sim 100\text{mJ}$ , necessary for the generation of attosecond pulses from relativistically oscillating plasma, typically operate at few hertz [14, 15] which means  $<1\text{W}$  of average power. The two main limiting factors are negative thermal effects [39] in nonlinear crystals and the availability of powerful pump lasers. Theoretical investigation of thermal properties of borate crystals (BBO, LBO) that are conventionally used in OPCPA allow for at least kilowatt-level of the average power [40], which means that in the nearest future this issue should be resolved by optimization of the amplification process and cooling technologies. As for the high power pump lasers, the second part of this thesis is dedicated to them.

## Part II

# Development of high power and repetition rate multipass amplifier

Second part of the manuscript describes the development of a high power thin-disk based multipass amplifier that is aimed to improve an existing state-of-the-art picoseconds-class pump laser [18]. Combining high repetition rate and pulse energy, such a powerful pump laser will push few-cycle light sources towards higher average output power making them more convenient for generation of isolated attosecond pulses. Moreover, high power picosecond-class lasers are of interest for other applications, including nonlinear spectral broadening in gas cells, (in [41] hundred-millijoules pulses corresponding to half a kilowatt of average power were used) or scattering of fast moving electrons for generation of soft X-ray [42].

Thin-disk lasers are solid state lasers with a specific geometry of the active medium. Traditional crystal shape is a *rod* – relatively big cylinder with the longitudinal dimension significantly exceeding the transverse one. A seed beam enters the crystal from one side and propagates through the whole material length, leaving it from the other side. Due to this long propagation a lot of energy can be extracted and very high pulse energies can be reached [43]. However rod crystals suffer from thermal effects: big crystal size prevents it from efficient cooling and leads to the strong temperature gradient in transverse direction, which in turn significantly reduces the beam quality and can also lead to damage [44].

In terms of longitudinal-to-transverse dimensions ratio thin-disks are complete antipodes to rods. They are only few hundreds microns thick, while the transverse size can reach tens of millimeters. One side of a disk has a high-reflective coating and is attached to a water cooled heat sink. Such a design requires special methods for pumping and energy extraction but leads to very efficient cooling of the whole crystal volume and makes it suitable for being used in high power lasers. State-of-the-art high power picosecond-class laser developed in our laboratory demonstrates a successful usage of thin-disk: it provides 200mJ pulses at repetition rate of 5kHz with high beam quality[18]. The same time existence of various commercially available thin-disk lasers (*Trumpf Scientific Lasers*) indicates high stability and reliability of this technology allowing for development of turnkey systems. **Chapter 3** gives a brief introduction to thin disks, describes the above-mentioned laser system and clarifies the physical and technical constrains preventing further increase of the output power and pulse energy. In order to overcome these constrains an additional amplifier that is also based on thin-disk was developed. It is described in details in **Chapter 4**.

# Chapter 3

## Thin-disk based high power pump laser

This chapter introduces basic physical phenomena needed for understanding of laser amplifiers, particularly thin-disk based – a very beneficial in terms of high average power type of solid state lasers. First of all, the basic concepts of a laser beam are described in section 3.1: what an ideal Gaussian beam is, how it propagates in free space and how real beams differ from this ideal model. Afterwards ray transfer matrix method is presented. It interprets transformation of laser beams by different optical elements in such a way, that even complicated optical systems can be described and calculated via simple linear equations. In section 3.2 basic interaction of light with active laser medium is discussed. Explained there Einstein's *rate equations* give the understanding of the *inversed population* – the key phenomenon in solid state lasers physics. Afterwards two different approaches in amplifiers design and realization of the *chirped pulse amplification* idea are shown. Section 3.3 closes the chapter with an explanation of the thin-disk geometry and a description of the state-of-the-art high power thin-disk based pump laser, which serves as a light source for the amplifier that is being developed.

### 3.1 Propagation and transformation of laser beams

#### 3.1.1 Ideal Gaussian beam

Propagation of electro-magnetic waves in free space or any optical media is generally described by the Maxwell's equations:

$$\nabla \times H = J + \frac{\partial D}{\partial t} \quad (3.1)$$

$$\nabla \times E = -\frac{\partial B}{\partial t} \quad (3.2)$$

$$\nabla \cdot D = \rho \quad (3.3)$$

$$\nabla \cdot B = 0 \quad (3.4)$$

Here  $E$  and  $H$  are the electric and magnetic fields,  $P$  and  $M$  are the electric and magnetic polarization,  $D = \epsilon_0 E + P$  – the electric displacement field,  $B = \mu_0 H + M$  – the magnetic flux density.

### 3.1 Propagation and transformation of laser beams

In a region with no electric charges ( $\rho = 0$ ) and no currents ( $J = 0$ ) they turn into the wave equations<sup>1</sup> **3.5–3.6** [45, p43-46]:

$$\frac{1}{c^2} \frac{d^2 E}{dt^2} - \nabla^2 E = 0 \quad (3.5)$$

$$\frac{1}{c^2} \frac{d^2 B}{dt^2} - \nabla^2 B = 0 \quad (3.6)$$

Since a wave should have a harmonic time dependence component that does not depend on the coordinate, i.e. it can be described as  $U(\vec{r}, t) = U(\vec{r})e^{j\omega t}$ , the wave equations can be transformed into Helmholtz equation:

$$\Delta U(\vec{r}) + k^2 U(\vec{r}) = 0 \quad (3.7)$$

For a linear homogeneous media one of the simplest solutions of Helmholtz equation is a monochromatic plane wave:

$$U(z) = A_0 e^{-jkz} \quad (3.8)$$

$A_0$  is the wave amplitude,  $z$  is the coordinate in the direction of propagation,  $k = \omega/c$  is so called wave number. However due to its wave nature light does not always propagate as a plane wave would do. In order to correctly describe the propagation of a laser beam, a plane wave should be modified with a few assumptions. The first is that the amplitude depends on the coordinate and can slowly change during propagation:

$$U(r, z) = A(r, z)e^{-ikz} \quad (3.9)$$

where  $\frac{\partial A}{\partial z} \ll kA$  and  $\frac{\partial^2 A}{\partial z^2} \ll k^2 A$

The second one is called *paraxial approximation*. It means that all the normals to the *wavefront* – a surface consisting of the points at which electromagnetic wave has the same phase - do not deviate a lot from the propagation direction. Within these two assumptions the solutions of **3.7** are the transverse electro-magnetic (TEM) modes. Such waves preserve their transverse intensity distribution along the propagation direction changing only the field amplitude:  $A(r, z) = A(z)f_z(r)$ . There are several sets of mathematical expression for them, for example Hermite-Gaussain or Laguerre-Gaussain modes. **Figure 3-1a** shows several examples.

The most commonly used mode is the TEM<sub>00</sub>, which is often called *Gaussian beam*. It is a radially symmetric mode with the transverse intensity following the Gaussian distribution:

$$I(r, z) = I_0 \left( \frac{\omega_0}{\omega(z)} \right)^2 e^{-\frac{2r^2}{\omega^2(z)}} \quad (3.10)$$

where  $I_0$  is the waist peak intensity,  $\omega$  – the beam radius at  $1/e^2$  level,  $z$  – the coordinate along the propagation axis,  $r$  – the radial distance to the axis.

---

<sup>1</sup> All the basic equations presented in section **3.1** are taken from [43] if other sources are not specified.

### Chapter 3: Thin-disk based high power pump laser

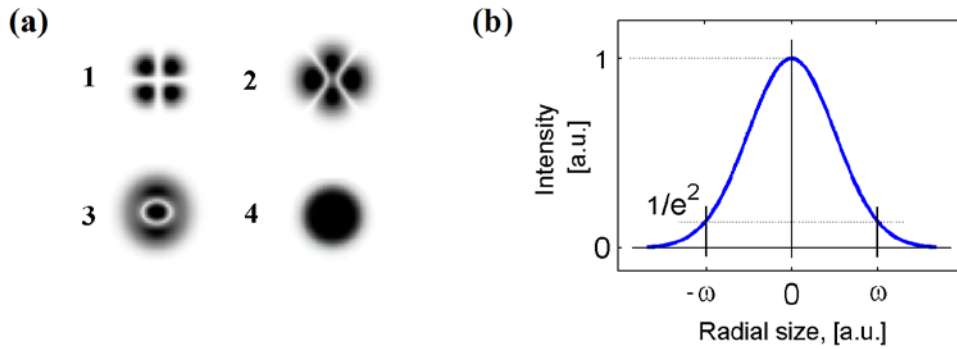


**Figure 3-1: TEM modes.**

(a) Different examples of TEM modes. Example 4 is the TEM<sub>00</sub> mode, which is also called Gaussian. (b) Radial intensity distribution of a Gaussian mode and definition of its waist radius at 1/e<sup>2</sup> intensity level.

When such a beam propagates, diffraction causes the light to spread in transverse direction leading to increase of the beam diameter even after collimation or focusing. Such a beam evolution is shown in **Figure 3-2** and follows the equations:

$$\omega(z) = \omega_0 \frac{1}{\sqrt{1 + (z/Z_R)^2}} \tag{3.11}$$

$$Z_R = \frac{\pi\omega_0^2}{\lambda} \tag{3.12}$$

Here  $\omega_0$  is the beam waist and  $\lambda$  is the wavelength. *Rayleigh range*  $Z_R$  shows how fast the beam diverges. It is a distance from the waist, at which the beam area  $\pi\omega^2/2$  increases twice. **Figure 3-2** also shows that beyond the Rayleigh range the beam asymptotically tends to the constant divergence  $\theta = \omega_0/Z_R$ .

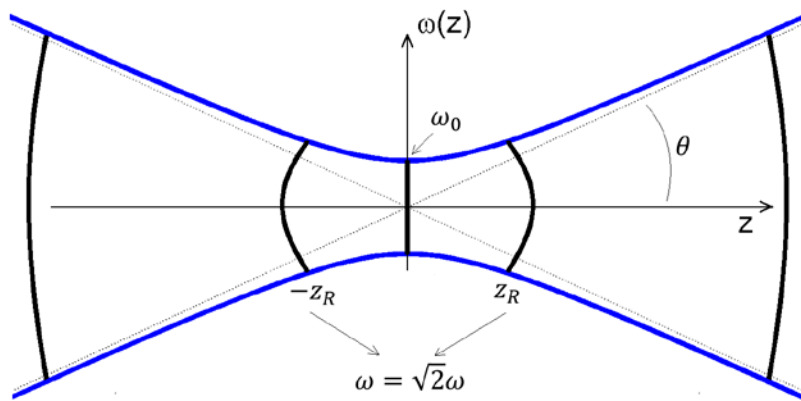


**Figure 3-2: Gaussian beam evolution.**

Propagation of an ideal Gaussian beam is completely defined by its waist radius  $\omega_0$  and the Rayleigh range  $Z_R$ , that shows how fast beam expands due to natural diffraction. Significantly away from the waist beam tends to a constant divergence  $\theta$ . Thick black lines show the wavefront: it is flat at  $z = 0$ , has maximal flexure at  $z = Z_R$  and then decreases, tending to being flat again.

It is also important to mention such a beam parameter as the wavefront radius of curvature  $R$ . For example, a plane wave **3.8** propagates only in  $z$ -direction, so its wavefront does not change and is always presented by a plane that is perpendicular to the propagation direction: all the

### 3.1 Propagation and transformation of laser beams

points on such a plane have the same phase and accumulate equal phase difference while propagating along  $z$  axis. Corresponding radius of curvature (RoC) is infinite. In case of a Gaussian beam electromagnetic waves not only propagate along  $z$  axis, but also diverge in transverse direction. Since the wave velocity in the propagation direction stays equal to the speed of light, diverging waves obtain some transverse velocity component, but corresponding  $z$ -component decreases. This leads to accumulation of a phase delay in  $z$ -direction, i.e. a change of the wavefront curvature  $R$ : it is infinite (plane wavefront) at the waist, then curvature decreases and reaches the minimum around Rayleigh range, but afterwards increases again and tends to infinity when the beam gravitates to a constant divergence  $\theta$ . This behavior can be expressed with the following equation:

$$R(z) = z \left( 1 + \left( \frac{z_R}{z} \right)^2 \right) \quad (3.13)$$

#### 3.1.2 Ray transfer matrix method

The equations 3.11 and 3.12 are enough to describe a free propagating beam. But such equations for beam transformation in an optical system – even a simple one, containing just few lenses – would look much more complicated. The ABCD (or *ray transfer matrix analysis*) method was originally invented for ray tracing in geometrical optics, but also allows describing a Gaussian beam transformation in a relatively simple way.

Geometrical optics (also called *ray optics*) is a model describing the light propagation in terms of rays. Such approximation is acceptable if the wavelength  $\lambda$  is small comparing to the scale of any changes in the medium, thus light does not experience interference or diffraction and propagates corresponding to the plane wave equation 3.8. Then the wave is described as the *light ray* – a line, perpendicular to the wavefront plane and collinear to the wave vector  $k$ .

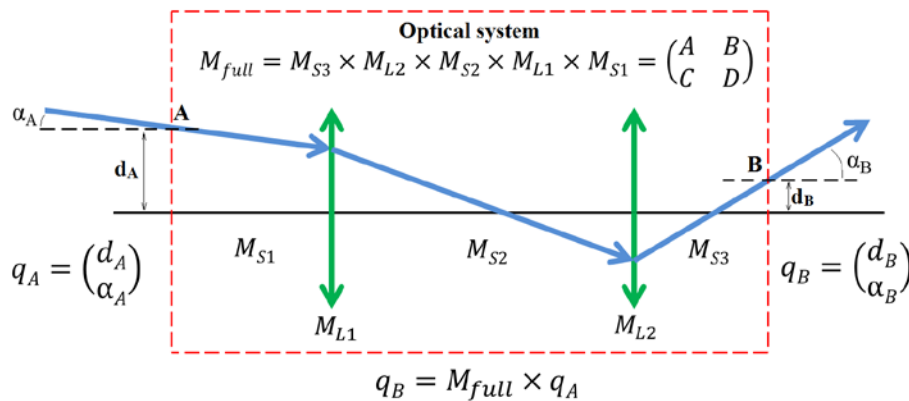


**Figure 3-3: Ray transfer matrix method.**

A light ray enters the optical system at the point  $A$  having the angle and distance relatively to the central optical axis  $\alpha_A$  and  $d_A$  and leaves the system at  $B$  with the corresponding angle and distance  $\alpha_B$  and  $d_B$ . Thus the output ray parameters encoded in  $q_B$  are connected to the input ray parameters via a  $2 \times 2$  matrix  $M_{full}$ . The matrix  $M_{full}$  presents the total transformation that an input ray experiences while propagating through the optical system and can be calculated via the individual matrices of the optical system elements: lenses, free space propagation, different media interfaces etc. Some individual matrices are described in **Table 3-1**.

### Chapter 3: Thin-disk based high power pump laser

Propagation and transformation of such a ray can be described with a ray parameters vectors  $q$ , a two-elements vector representing the distance and the angle relatively to the *main optical axis* of a system – imaginary line, defining the center of rotational symmetry. When a ray propagates, it changes these two parameters. Within the paraxial approximation free propagation does not affect the angle and only modifies the position:  $d_{new} = d_{old} + \alpha_{old}$ , while a thin lens with the optical power  $P = 1/f$  changes only the direction:  $\alpha_{new} = \alpha_{old} + Pd_{old}$ . Such transformations can be represented as a system of linear equations and written in a form of a linear matrix:

$$q_{new} = \begin{pmatrix} d_{new} \\ \alpha_{new} \end{pmatrix} = \begin{pmatrix} A & B \\ C & D \end{pmatrix} \times \begin{pmatrix} d_{old} \\ \alpha_{old} \end{pmatrix} = M \times q_{old} \quad (3.14)$$

The matrix  $M$  is called *ray transfer matrix*. **Figure 3-3** gives an example of using this method for a more complicated optical system, consisting of two lenses and some free propagation intervals. The full transformation matrix is then a linear left-side multiplication of individual matrices, which are described in **Table 3-1**

**Table 3-1: Ray transfer matrices of simple optical components** [45, p29].

Element	Matrix	Remarks
free propagation (constant refractive index $n$ )	$\begin{pmatrix} 1 & l \\ 0 & 1 \end{pmatrix}$	$l$ – propagation distance
thin lens	$\begin{pmatrix} 1 & 0 \\ -P & 1 \end{pmatrix}$	$P=1/f$ $F$ – focal length
refraction at flat interface	$\begin{pmatrix} 1 & 0 \\ 0 & n_1/n_2 \end{pmatrix}$	$n_1, n_2$ – refractive index of initial and final materials
refraction at curved interface	$\begin{pmatrix} 1 & 0 \\ \frac{n_1 - n_2}{Rn_2} & n_1/n_2 \end{pmatrix}$	$R$ – interface radius of curvature $n_1, n_2$ – refractive indexes

Ray transfer (or ABCD) matrix method allows calculating the light propagation through a very complicated optical system. But since it is based on the propagation of the flat waves, it cannot be directly used for Gaussian beams. According to **3.13** the wavefront of a Gaussian beam is relatively flat only around the waist and significantly far away from it, but it has some finite curvature around Rayleigh range. This means that the wave does not propagate according to the plane wave equation **3.8** and cannot be described with a single straight light ray.

In order to utilize the advantages of ABCD matrix method the beam parameters vector should be replaced with a *complex beam parameter*. It is defined by the equations **3.15** and contains information about the current position of the beam relatively to the waist and Rayleigh range  $Z_R$ . Since the Gaussian beam is completely defined by these two parameters, it can also be expressed (**3.16**) via the current beam size  $\omega$  and the wavefront radius of curvature  $R$ , which might be interpreted as analogues to the ray optics parameters  $d$  and  $\alpha$ .

### 3.1 Propagation and transformation of laser beams

$$q = (z - z_{waist}) + iZ_R \quad (3.15)$$

$$\frac{1}{q} = \frac{1}{R} - i \frac{2}{k\omega^2} \quad (3.16)$$

In analogy to the ray parameters vector such a definition allows to describe transformation of a Gaussian beam via ABCD matrix. Thus free propagation distance  $d$  just shifts the beam relatively to its waist, what based on **3.15** means  $q_{new} = q_{old} + d$ . Meanwhile a thin lens with the optical power  $P = 1/f$  modifies the wavefront curvature leading to a different propagation, but without immediate change of the beam size, what according to **3.16** can be expressed as  $1/q_{new} = 1/q_{old} + 1/f$ . It can be shown that all the matrices from **Table 3-1** (and other ray transfer matrices, which are not presented in the table) can be applied to a Gaussian beam, if the equation **3.14** is modified to:

$$q_{new} = \frac{Aq_{old} + B}{Cq_{old} + D} \quad (3.17)$$

#### 3.1.3 Real beam and embedded Gaussian principle

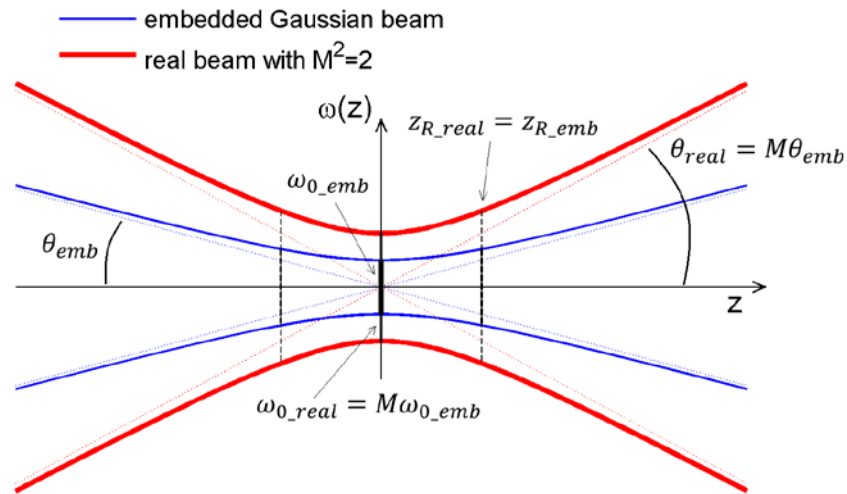


**Figure 3-4: M-squared parameter of a real beam.**

Blue line is a true (embedded) Gaussian beam, red line – a real beam with  $M^2 = 2$ . It has the same  $R_z$ , but  $M$  times bigger waist at any  $z$  coordinate as well as  $M$  times bigger divergence.

A real beam never exactly repeats the behavior of a pure Gaussian beam – it is usually a mixture of the Gaussian mode and other TEM modes. In order to describe how much a given beam differs from an ideal Gaussian and to predict its further propagation, the parameter  $M^2$  (*M-squared*) was introduced [46]:

$$M^2 = \frac{\pi\theta_{real}\omega_{0real}}{\lambda} \quad (3.18)$$

where  $\theta_{real}$  and  $\omega_{0real}$  are the measured divergence and beam waist. The closer is  $M^2$  to 1 the closer is the beam to a Gaussian mode. **Figure 3-4** shows the difference in propagation between the perfect Gaussian beam and a beam with  $M^2 = 2$ . Effectively such an imperfect beam just

## Chapter 3: Thin-disk based high power pump laser

diverges faster and cannot be focused so tight as an ideal one. For correct measurement of the divergence and the waist a set of beam profile measurements should be performed while the beam is being focused. Fitting the measured beam size data to the equation **3.19** [47, p188] gives the waist size and divergence of a real beam, which are needed to calculate the  $M^2$ .

$$\omega_{real}^2 = \omega_{0real}^2 + \theta_{real}^2 z^2 \quad (3.19)$$

Propagation and transformation of such a beam can be simulated by introducing an *embedded Gaussian beam* that propagates coaxially with the real one, but has  $M^2$  times smaller area at any  $z$  coordinate, what in terms of beam radius means:

$$\omega_{emb} = \frac{\omega_{real}}{M} \quad (3.20)$$

Gaussian propagation equations or ABCD transformation should be performed with the embedded beam. Afterwards back calculation based on the same equation provides the real beam size.

## 3.2 Basic principles of laser amplifiers

### 3.2.1 Optical transitions in a medium

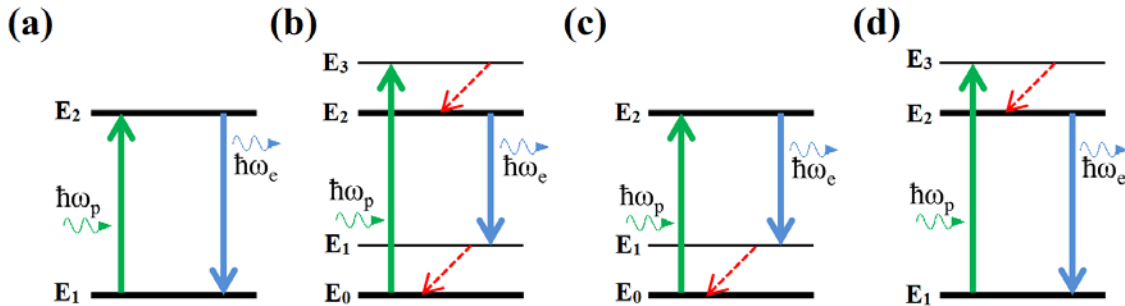


**Figure 3-5: Optical transitions in 2-, 4- and 3-level systems.**

Thick black lines show stable electronic levels, thin black lines – unstable levels, at which electrons have a very high probability of non-radiative scattering (shown with red dashed arrows). Thick vertical arrows show absorption of the pump photons (green) and relaxation with emission of a new photon (blue).

While propagating through a medium, laser light can be absorbed or in some special cases amplified. These processes can be described via dynamics of the electrons population density. In the simplest case a monochromatic light  $\omega_0$  interacts with a material having two discrete energy levels  $E_1$  and  $E_2$  (**Figure 3-5a**), populated with  $N_1$  and  $N_2$  electrons respectively with the total amount of electrons  $N = N_1 + N_2$ . In this case there are several possible transitions. The first is *absorption* of a photon with an energy  $\hbar\omega_0 = E_2 - E_1$ , leading to excitation of an electron from a lower to a higher level. Effectively such an excited electron stores the energy  $E_s = E_2 - E_1$  that can be further released (with or without radiation) during relaxation to a lower level again. Such energy accumulation process is called *optical pumping*. Another possible transition is the *emission* of a photon of the same energy  $E_s$ , which can happen *spontaneously* or can be triggered by the interaction of an electron with another photon with

### 3.2 Basic principles of laser amplifiers

equal energy. Such emission is called *stimulated* and was first introduced by Albert Einstein. This phenomenon is the key point for laser light amplification, because emitted photons are coherent to the initial ones. There is one more possible transition – a non-radiative relaxation of an electron from an upper to a lower level. In this case accumulated energy is transferred to the lattice oscillations (phonons) or molecular and atomic oscillations and vibrations, what increases material temperature. But for two stable levels with a relatively big energy gap between them the probability of non-radiative relaxation is very low and can be neglected while considering electrons dynamics on a short time scale (within the upper level *lifetime*, which will be explained later in paragraph 3.2.3). All three radiative processes are stochastic and depend on population of involved energy levels, material properties and amount of photons presented in the interaction volume. They can be mathematically expressed in the following equations<sup>1</sup> [48]:

$$\text{Absorbtion:} \quad \frac{\partial N_2}{\partial t} = -\frac{\partial N_1}{\partial t} = N_1 B_{12} \rho \quad (3.21)$$

$$\text{Spontaneous emission:} \quad \frac{\partial N_2}{\partial t} = -\frac{\partial N_1}{\partial t} = -N_2 A_{21} \quad (3.22)$$

$$\text{Stimulated emission:} \quad \frac{\partial N_2}{\partial t} = -\frac{\partial N_1}{\partial t} = -N_2 B_{21} \rho \quad (3.23)$$

Here  $A_{21}$ ,  $B_{12}$  and  $B_{21}$  are *Einstein coefficients* encoding the material absorption and emission properties and  $\rho$  is the photon density per unit of volume. It can be also shown, that  $B_{21} = B_{12} = B$  [49, p218]. Amplification is only possible when stimulated emission exceeds absorption, so the condition  $N_1 B_{12} < N_2 B_{21}$  should be satisfied, which is equivalent to  $N_2 > N_1$  for an ideal 2-level system and is called *inversed population*. Because of spontaneous emission inversed population is necessary but not sufficient for light amplification. Additionally to the equations 3.21–3.23 the total amount of electrons should not change:

$$\frac{\partial N}{\partial t} = N_1 B_{12} \rho - N_2 B_{21} \rho - N_2 A_{21} \equiv 0 \quad (3.24)$$

Solving this equation gives  $N_2$ :

$$N_2 = \frac{N}{2 + \frac{A_{21}}{B\rho}} \quad (3.25)$$

It clearly shows that in considered 2-level system  $N_2 < N/2$ , which means that  $N_2 < N_1$  i.e. inversed population and thus amplification is impossible. This limitation can be eliminated in a 4-level system with a significant probability of non-radiative spontaneous relaxation. **Figure 3-5b** shows such a system. There the energy levels  $E_1$  and  $E_3$  are much less stable than  $E_0$  and  $E_2$  because of non-radiative relaxation: electrons at these levels have very high probability of falling to a lower energy level (transferring their energy into the heat) much faster than any radiative transition can occur. Pumping with  $\hbar\omega_{30} = E_3 - E_0$  together with this fast relaxation leads to a high population of  $E_2$  and an almost zero population of  $E_3$ . Stimulated emission at  $\hbar\omega_{21} = E_2 - E_1$  brings the electrons to the level  $E_1$ , but they almost immediately

<sup>1</sup> Equations presented in paragraph 3.2.1 are taken from [48] if other sources are not specified.

## Chapter 3: Thin-disk based high power pump laser

move to the level  $E_0$  via non-radiative relaxation. Thus inversed population between the levels  $E_2$  and  $E_1$  can be quite high allowing for significant amplification. The disadvantages are higher spontaneous emission (due to additional probability of transition to another lower level) and energy losses  $E_{loss} = \hbar\omega_p - \hbar\omega_e$ , which limit pumping efficiency and lead to significant heat of the material. Normalized to the pump photon energy these losses are called *quantum defect*.

$$\eta_P = \frac{\omega_p - \omega_e}{\omega_p} = 1 - \frac{\lambda_p}{\lambda_e} \quad (3.26)$$

To reduce the quantum defect while allowing inversed populations 3-level materials can be used (**Figure 3-5c and d**). They are similar to a 4-level system described above, but have only one non-radiative transition from a single unstable energy level. On the other hand it is more complicated to reach high population inversion for such energy structure comparing to a 4-level system.

### 3.2.2 Yb:YAG emission and absorption cross-section

Equations 3.21–3.23 describe the electrons and photons dynamics for a single wavelength and discrete electron energy levels. Real materials however have a significantly more complicated energy structure. Each energy level is not an infinitely narrow line  $E_L$  but rather a quasi-continuous zone populated with electrons, whose energy distribution in thermal equilibrium can be described with *Boltzmann distribution* [50] :

$$N(E) = N(E_L)e^{-\frac{E-E_L}{k_B T}} \quad (3.27)$$

This means that emission and absorption of the photons is possible not only for exact wavelengths, but within some spectral range. Probability of such transitions is wavelength dependent and can be described by emission and absorption *cross-section*  $\sigma_{em}(\lambda)$  and  $\sigma_{abs}(\lambda)$ , which are similar to the Einstein rate coefficients. Numerically cross-section  $\sigma$  [ $cm^2$ ] can be explained via the following equation:

$$R = \frac{\sigma I}{h\nu} = \sigma\Phi \quad (3.28)$$

Here  $R$  [ $s^{-1}$ ] is the amount of transitions per second and the combination of the intensity  $I$  [ $W/cm^2$ ] and the photon energy  $h\nu$  [ $J$ ] gives the photon flux  $\Phi$  [ $cm^{-2}$ ] – the number of photons per square meter per second. Emission and absorption cross-sections are fundamental properties, which (among other parameters) characterize the usability of a material as an amplification medium.

**Figure 3-6** shows the emission and absorption cross-section of *yttrium aluminum garnet* (YAG) doped by ytterbium ions ( $Yb_{3+}$ ). Physical and mechanical properties of this material make it the best amplification medium for development of high power multipass amplifier. It not only has high damage threshold [51] and good thermal conductivity [52] , but also demonstrates a perfect ratio between the emission and absorption cross-section. At 1030nm emission exceeds absorption for almost one order of magnitude, while the lifetime is relatively high ( $\tau \approx 1ms$ ). Such a combination of parameters allows for reaching significant inversion of population,

## 3.2 Basic principles of laser amplifiers

which is necessary for amplification. The same time Yb:YAG has high absorption at 940nm and 969nm, what is very beneficial for efficient pumping. Additionally to good optical and thermal properties it has high mechanical strength and robustness, what is necessary for cutting and polishing.

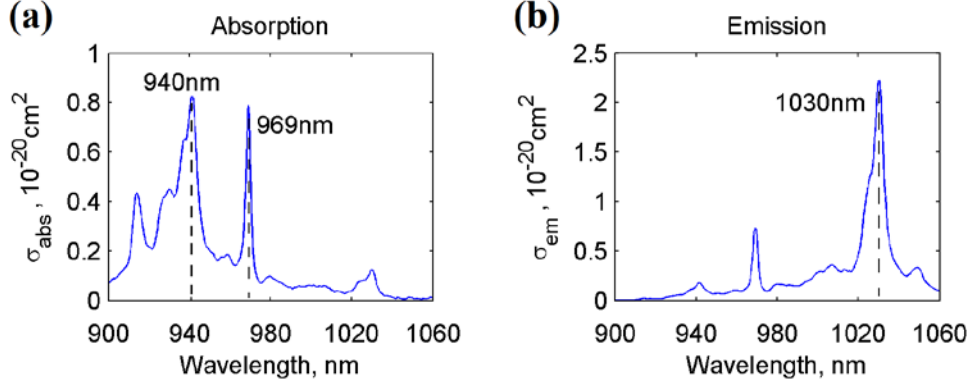


**Figure 3-6: Emission and absorption cross-section of Yb:YAG [52].**

Dashed lines show the main pumping (940nm and 969nm) and lasing (1030nm) wavelengths of the lasers based on this gain medium.

### 3.2.3 Numerical description of amplification

Since absorption and emission in Yb:YAG happen within narrow peaks in the spectrum, it can be numerically described as a 2-level system (**Figure 3-5a**), where both levels follow the Boltzmann distribution **3.27**. In thermal equilibrium the amount of absorbed and emitted photons should be the same in all the spectral range, which means [50]:

$$N_2 \sigma_{em}(\omega) \Phi(\omega) + N_2 A(\omega) = N_1 \sigma_{abs}(\omega) \Phi(\omega) \quad (3.29)$$

Here  $\Phi(\omega)$  is the photon flux,  $A(\omega)$  represents the probability of spontaneous emission of a photon with the frequency  $\omega$ . Considering the emission and absorption in the full spectral range requires integration, which gives:

$$N_2 \int \sigma_{em}(\omega) \Phi(\omega) d\omega + N_2 \int A(\omega) d\omega = N_1 \int \sigma_{abs}(\omega) \Phi(\omega) d\omega \quad (3.30)$$

Integrals within narrow absorption and emission peaks can be represented by some effective values  $\sigma_{emP}$ ,  $\sigma_{absP}$ ,  $\sigma_{emL}$ ,  $\sigma_{absL}$ , which express the integrated probability of emission and absorption within the pumping and lasing spectral ranges. Integrated probability of spontaneous emission  $\int A(\omega) d\omega$  has the meaning of spontaneous emission frequency and can be expressed via the *lifetime*  $\tau$ . Thus expression **3.30** takes the next form:

$$N_2 (\sigma_{emP} \Phi_P + \sigma_{emL} \Phi_L) + N_2 / \tau = N_1 (\sigma_{absP} \Phi_P + \sigma_{absL} \Phi_L) \quad (3.31)$$

This equation defines the relation between all the radiative transitions in a material in presence of pump and seed light. It is also used in numerical calculations of laser amplification, which will be shown later in this work for comparison with the measured data.

## Chapter 3: Thin-disk based high power pump laser

Analysis of the equation 3.31 also helps to introduce and describe some important amplification parameters. For example the *small signal gain*, which effectively means the maximal possible amplification of a weak laser pulse that propagates through a well pumped active medium and is being amplified. A weak seed pulse almost does not reduce the inversed population, because stimulated emission is proportional to the flux, so amount of emitted photons can be considered as negligible relatively to the whole upper level population. However the same amount of photons is significant when adding up with a small seed pulse with the flux  $F_L$ . Spontaneous emission can be considered as a much slower process, that just affects the ratio between  $N_1$  and  $N_2$  during pumping, but does not occur at the time scale of propagating through thin layer of material. Then, assuming the population  $N_1$  and  $N_2$  to be spatially homogenous, the change of the seed flux along the propagation direction  $z$  can be described as:

$$\frac{\partial \Phi_L(z)}{\partial z} = N_{emL} - N_{absL} = N_2 \sigma_{emL} \Phi_L(z) - N_1 \sigma_{absL} \Phi_L(z) \quad (3.32)$$

It can be solved for  $F_L(z)$ , giving

$$\Phi_L(z) = \Phi_L(0) e^{gz} \quad (3.33)$$

$$\text{where } g = N_2 \sigma_{emL} - N_1 \sigma_{absL}$$

Here  $g$  is the material *gain coefficient*, that defines amplification or absorption of light. If  $g \leq 0$ , i.e.  $N_2/N_1 \leq \sigma_{absL}/\sigma_{emL}$ , amplification is impossible – this is an analogue of the inversed population requirement for an ideal 2-level system ( $N_2 > N_1$ ) discussed in the previous paragraph. Factor  $G = e^{gZ}$  corresponding to the full crystal thickness  $Z$  is called *small signal gain* and shows the upper limit of possible amplification in a given crystal. Real amplification (especially for a high seed flux) will be always smaller due to reduce of the inversed population by stimulated and spontaneous emission and non-radiative relaxation.

Repeating the same consideration for the pump light gives analogical equations for the pump light absorption coefficient  $\alpha$ :

$$\Phi_p(z) = \Phi_p(0) e^{\alpha z} \quad (3.34)$$

$$\text{where } \alpha = N_2 \sigma_{emP} - N_1 \sigma_{absP}$$

### 3.2.4 Regenerative and multipass amplifiers

A regenerative amplifier (**Figure 3-7a**) is an optical *resonator* – a system organized in a way, that the laser beam circulates in a closed path – with an active medium inside. The key element of such system is an optical switch that keeps the seed beam within the resonator, where it propagates through the active medium multiple times until it cannot be amplified anymore because the active media is *depleted*, i.e. the upper level is depopulated and the amplification factor  $g$  (equations 3.33) becomes negative.

Switching function in modern high power regenerative amplifiers is performed by using electro-optical Pockels effect [45, p978] in nonlinear crystals (BBO, KDP and others). Such

### 3.2 Basic principles of laser amplifiers

crystals can rotate the polarization of the propagating light depending on the applied voltage and thus can keep the beam inside the resonator or let it propagate through a polarizer and leave the system. For correct operation of an amplifier fast and reliable voltage switching in the crystal is required. Moreover the crystal itself should withstand high power and pulse energy in the resonator and should not introduce any nonlinear effect. Due to these problems optical switches are the main technological constraints for further power and pulse energy scaling of state-of-the-art regenerative amplifiers.

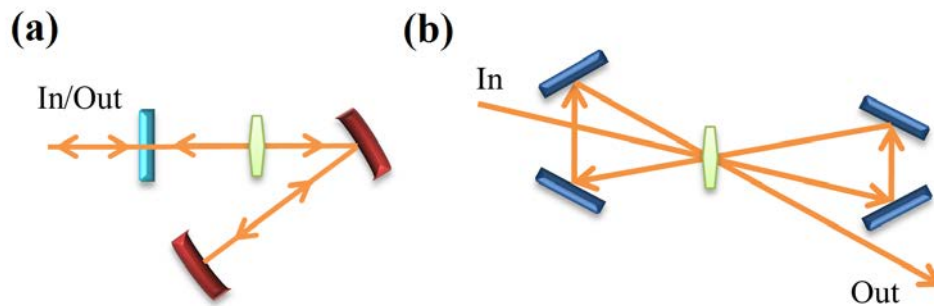


**Figure 3-7: Two types of amplifiers.**

(a) Linear regenerative amplifier. The seed beam enters the resonator through the optical switch (light blue) and bounces there several times being amplified in the active medium (green). Minimum two curved mirrors (red) are required. After depletion of the active medium the amplified seed beam leaves the resonator via the same optical switch, whose switching time defines the amount of bounces. (b) Multipass amplifier. The seed beam is being steered by a set of mirrors (blue). It performs several passes through the active medium (green). Optical switch is not needed. The amount of passes depends on the amount of steering mirrors.

The main advantage of regenerative amplifiers is the preservation of the *eigenmode*. If the input beam corresponds to the eigenmode (which is defined by the resonator structure), it preserves the size and divergence after the full propagation through the resonator and starts the next iteration with the same propagation properties. Beams, that do not match the eigenmode, change their size after each iteration and experience much worse amplification due to non-optimal size on the crystal and higher losses related to exceeding the optics aperture. Due to this property the amount of iterations can exceed 100 and the amplification factor can reach  $10^8$ – $10^9$  while the beam preserves high quality. This is very beneficial for amplification of weak seed beams up to millijoule-level within a single resonator.

In contrary to regenerative type, multipass amplifiers do not need any switching elements. They consist of an active medium crystal and a set of mirrors that steer the beam into the crystal several times. This makes the optical scheme simpler in terms of polarization optics and removes all the problems and constrains connected to the optical switch allowing to use higher pulse energies. On the other hand every new iteration requires a new beam path and extra mirrors – or in some special cases additional surface area on the same mirror. Thus building a setup with many passes through the crystal becomes complicated, what means that the energy extraction is usually not as efficient as in the resonator-type. The solution is to have much higher input pulse energies, which automatically means lower amplification factors. Typical beam quality is also lower and decreases with every additional iteration.

## Chapter 3: Thin-disk based high power pump laser

This property of a multipass amplifier motivates to use it as a secondary, high-energy amplifier that follows a primary regenerative amplifier in order to additionally increase the output pulse energy. This will be demonstrated in the next chapter.

### 3.2.5 CPA principle and dispersion control

Most of the modern laser amplifiers are based on *chirped pulse amplification* (CPA) principle, that was invented in 1980s by D. Strickland and G. Mourou [53] and awarded with the Nobel Prize in 2018 (sharing it with few other optical methods). The main idea is to stretch the pulse in time (in a reversible way) before the amplification in order to reduce the peak intensity, corresponding unwanted nonlinear effects and the damage probability. Of course, the intensity can be easier reduced by increase of the beam diameter, but a lot of different optical components (including gain media and crystals performing optical switching) have limited apertures and do not support big beams.

In order to create controlled and compensable stretching of a laser pulse its spectral phase should be modified in a way, that some spectral components obtain a temporal delay. Laser pulse is called positively or negatively *chirped* when the red (long wavelengths) part of the spectrum gets ahead or behind the blue (short wavelengths) part respectively. Conventional optical *stretcher* consists of a pair of gratings and lenses aligned in a way that propagation length of the red part of the spectrum is shorter than for the blue part, which corresponds to a positive pulse chirp. After amplification the beam is usually enlarged in order to compensate the intensity increase and is sent to the compressor, where the red part of the spectrum is delayed relatively to the blue part and the chirp is eliminated. **Figure 3-8** demonstrates one of the possible schemes of a gratings based compressor.

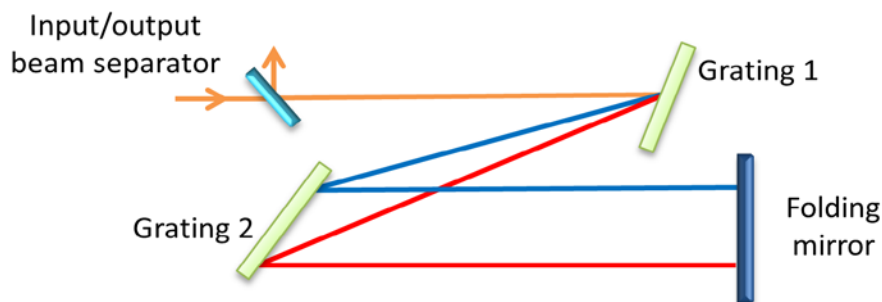


**Figure 3-8: Principle scheme of a grating compressor.**

Two reflective gratings create different paths for the red and blue part of the spectrum, leading to a temporal delay. The folding mirror is used to send the beam back and compensate spatial/angular separation of the spectral components. Input and output beams are separated by the polarization optics (thin film polarizer + quarter wave plate that is crossed twice).

As the result of propagation through a stretcher an input pulse obtains a chirp that depends on the setup geometry and can be expressed via the temporal delay per nm of spectrum, for example 200ps/nm. Thus a perfectly (near Fourier limit) compressed pulse having the 2nm FWHM bandwidth around 1030nm (which means ~800fs duration) will be stretched to ~1.4ns at FWHM, what proportionally reduces the peak intensity ~1750 times. Thereby the seed pulse

can be amplified while staying within the intensity range that does not lead to any unwanted effects. After amplification the chirp has to be compensated by a properly adjusted compressor with the opposite delay of -200ps/nm. If the pulse did not experience any phase modification during the amplification process, it will be compressed back to its original duration. Taking into account that the peak intensity of the amplified pulse is supposed to be significantly higher, its size in the compressor and afterwards should be adjusted to keep the intensity on the gratings and mirrors within acceptable values.

It is also important to mention that not only an unwanted phase modification can affect the duration of the amplified output pulse. Since the gain coefficient has an exponential behavior (equation 3.33) and emission cross-section of Yb:YAG is a narrow peak around 1030nm, the central part of the spectrum is always amplified more than the sides. It leads to a natural reduction of the FWHM bandwidth and corresponding increase of the Fourier limit. Physically it can be understood as a disturbance in the interference between different spectral components. In a perfectly compressed pulse with a given spectrum  $S_1(\omega)$  all the spectral components of the electric field interfere in a way that at the time  $t = \pm t_{FWHM}$  total field intensity falls twice and decays further outside this time frame. When the central part of the spectrum  $S_1(\omega)$  is amplified more than the sides, the interference pattern – which is the temporal shape of the pulse – changes, though the phase of the corresponding spectral components stays perfectly the same. This effect is called *gain narrowing* and plays an important role especially for the high-gain regenerative amplifiers.

## 3.3 Thin-disk lasers

### 3.3.1 Thin-disk geometry

The key point of the thin-disk lasers concept is a significant shortening of the active medium in the longitudinal direction down to a few hundreds of micrometers, while the transverse dimension can stay within a couple of centimeters. Therefore a traditional laser rod shrinks to a very narrow disk, whose front side is used for pumping and seeding and the rear side is attached to a heat sink via a diamond substrate (**Figure 3-9a**). Such a geometry provides not only an efficient cooling of the whole crystal due to the high cooling surface-to-volume ratio, but also a near homogeneous heat flow independent on the radial coordinate, what eliminates the transverse heat gradient typical for rod crystals. All this leads to a significant reduction of the thermally caused deformations and lens effects allowing for high power pumping with minimal distortions of the amplified beam [54].

Since the rear side of the crystal is used for heat sink, both the pump and seed beams have to enter and leave the crystal from the only available front side. It is possible through the use of anti-reflection coating (up to 99.99% transmission) on the front and a high-reflective coating (up to 99.99% reflectance) on the rear side of the crystal, which turns it into a mirror with an active medium layer in front – so called *active mirror*. Like ordinary mirrors, disks can also have some curvature: from almost flat ( $RoC \approx 20m$ ) up to significantly curved ( $RoC \approx 1.5 \div 2m$ ).

### Chapter 3: Thin-disk based high power pump laser

Providing excellent cooling properties, small thickness of the disk on the other hand raises the problem of efficient pumping and energy extraction. As it was shown in paragraph 3.2.3, absorption of the pump light depends exponentially on the propagation length  $I(L) = I_0 e^{-\alpha L}$ , where  $I_0$  is the initial light intensity,  $\alpha$  is the coefficient encoding material properties and  $I(L)$  is the intensity after propagation of distance  $L$ . Thus a decent material thickness is required for efficient pump light absorption, which in case of thin-disk can be accumulated only by multiple passes through the crystal. Special *pump head* provides several tens of bounces leading to efficient absorption of the pump light. **Figure 3-9b** shows the internal structure of a pump head. It contains a big parabolic mirror with a hole for the seed beam and several roof prisms. The curvature of the parabola and the distance to the folding prisms are matched and provide re-imaging of the pump beam back to the disk multiple times. Additionally an extra folding mirror can be installed in the end of the chain for doubling the amount of bounces and insuring almost complete absorption of the pumped light. Special collimation optics outside the pump head is required for proper in-coupling and controlling the pump beam size on the disk.

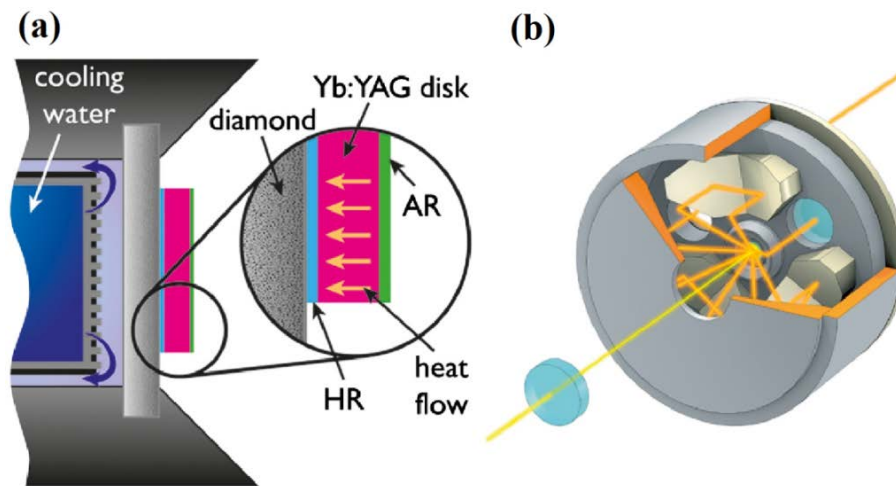


**Figure 3-9: Thin-disk geometry.**

(a) A thin-disk on a diamond substrate is attached to a heat sink. The front and rear sides of the disk are coated with anti-reflection (AR) and high-reflection (HR) coatings respectively. The diamond substrate is water cooled. (b) Structure of the disk pump head (courtesy of TRUMPF GmbH). Pump beam enters the head from the opening on the rear side and then is being several times imaged to the disk by the prisms and the parabolic mirror. Optionally a folding mirror can be installed for sending the pump beam back and doubling the amount of bounces over the disk. The front opening serves for the seed beam in-coupling. Figures are taken from [17].

In contrary to the pump light absorption efficient energy extraction can be performed in two different ways. The first is to use enough passes through the disk to extract all the stored energy. This principle is used in regenerative amplifiers, where the seed beam can perform more than hundreds passes until the disk is completely depleted<sup>1</sup>. The second method is based on the fact, that stimulated emission is proportional to the intensity of stimulating light. Thus using a high-intensity seed beam allows to extract almost the whole energy within a relatively low amount of passes. Such an approach takes place in multipass amplifiers where the amount of passes is limited.

<sup>1</sup> Here and later in the text depletion of the disk should be understood as depletion of the upper energy level in the pumped area of the disk.

### 3.3.2 Thin-disk based 1kW sub-picosecond pump laser

Current state-of-the-art high power and repetition rate pump laser is the 1kW, 200mJ sub-picosecond class thin-disk laser [18]. It is a CPA based system with a ring-type regenerative main amplifier. The front-end consists of a commercial fiber oscillator (*Menlo Systems YLMO*), pulse picker, stretcher and a pre-amplifier. The last element of the system is a grating compressor that compensates the chirp of the output pulses (**Figure 3-10**).

Menlo YLMO is an ytterbium fiber oscillator with ~14nm bandwidth centered at 1030 nm. It provides 4nJ, ~120fs pulses at 50 MHz repetition rate which is reduced down to 5kHz with a pulse picker (*Bergmann Messgeräte Entwicklung KG*). Afterwards the pulses are chirped in a grating stretcher that supports up to 10nm spectral bandwidth with the 55% throughput and the stretching factor of 500ps/nm. Thus 1.5nJ pulses stretched to 5ns are seeding the pre-amplifier that is an ytterbium-based linear type thin-disk based regenerative amplifier. It has a single thin-disk pumped with ~170W and 350 roundtrips, amplifying the input to 0.8mJ with 5nm FWHM spectral bandwidth.

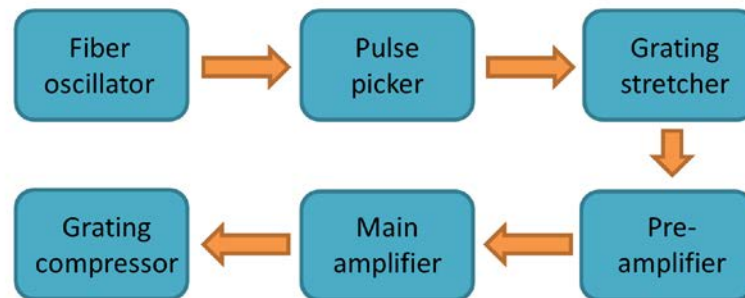


**Figure 3-10: Principle scheme of the source laser.**

The main idea behind the pre-amplifier is to reduce the gain-narrowing effect. Seeding the main amplifier with 1.5nJ would require amplification factor of  $\sim 10^8$  in order to reach 200mJ output pulses energy. Such a high amplification would significantly reduce the output spectrum bandwidth, which would lead to increase of the output pulse duration. Pre-amplifier gain medium CAIGO (ytterbium doped with  $\text{CaGdAlO}_4$ , [55]) has the amplification bandwidth of 80nm centered around 1030nm, which is almost 10 time broader than the material of the main amplifier, Yb:YAG. On the other hand CAIGO has worse thermal and optical properties [56], which prevent it from being used in the main amplifier. Thus a broad-band pre-amplifier partially counteracts the gain narrowing and allows to keep the spectrum broad enough to support 800fs Fourier limit (instead of 1200fs that would be a limit in case of using only Yb:YAG). Additionally to this advantage the pre-amplifier allows to decrease the amount of roundtrips inside the main amplifier what positively affects the overall stability of the system [19, p74].

Further amplification takes place in a ring-type regenerative amplifier with two Yb:YAG disks, pumped with 1kW each. Only a small portion (300 $\mu$ J) of the pre-amplifier output is used, and after 32 roundtrips within the main resonator it is amplified up to 220mJ. Gain narrowing reduces the spectral bandwidth to 2nm, what corresponds to ~1ns pulse duration with the above

### **Chapter 3: Thin-disk based high power pump laser**

mentioned stretching factor. Last part of the system is a grating compressor that compensates applied chirp (in a cost of 6% pulse energy losses) leading to an output pulse having ~205mJ energy and duration of ~800fs.

# Chapter 4

## Multipass amplifier

The following chapter describes the development of the amplifier aimed to improve the output power of existing pump laser described in paragraph 3.3.2. Optical element limiting the output power of such a resonator-based system is the Pockels cell crystal performing the optical switch function. The most advanced currently available Pockels cell operates close to its average power limit [19, p46-48] providing ~220mJ pulses at 5kHz repetition rate, what means that further amplification is only possible with a multipass type amplifier. Good beam quality simultaneously with above 1kW average power, leading to several kilowatts of average power inside the gain medium, requires extremely good cooling properties. Thus only Yb:YAG thin-disks can perform the gain medium function in such amplifier.

Due to the long lifetime (around 1ms) of Yb:YAG and 5kHz repetition rate of the seed laser (meaning 0.2ms interval between sequential pulses), pulsed pumping is not necessary and the disks can be efficiently pumped with a CW (continuous wave) laser. According to the emission cross-section pumping can be performed at 940nm or 969nm. Though 969nm is more beneficial in terms of 30% lower quantum defect and thus lower thermal load to the material, high power configuration of lasers are significantly more expensive. Thus two industrial 4kW, 940nm pump lasers were chosen as the pump light source. Details connected to the pump beam delivery are given in section 4.1.

For optimal amplification the seed beam should be precisely aligned relatively to the pumped area of the disk. Its size should be optimized, balancing between the energy extraction efficiency and possible aperture effects. There are two fundamentally different designs of multipass amplifiers, which preserve optimal beam properties at each propagation iteration. The first method is based on imaging: the system design leads to a uniform transformation matrix within a single iteration. In this case regardless of the input beam parameters every new cycle starts with exactly the same beam. The second possible solution is a quasi-resonator design that preserves only some exact beam called *eigenmode*. Both methods have their own advantages and problems and will be explained in details in the following sections.

Regardless of the design, the developed amplifier consists of two disks ( $D = 20mm$ ,  $RoC \approx 20m$ ) installed in pump heads, which provide 44 bounces of the pump beam. Both pump heads are allocated on separate optical breadboards installed in two vacuum chambers, which can be used for air evacuation or just as a protection. Both chambers are connected by a big vacuum tube. Pump light is delivered to the chambers via a multimode optical fiber and reimaged to the disks via special pump optics. A set of 40 mirrors can be installed in each chamber, providing up to 10 iterations of the seed beam bouncing between the two disks (up to 19 total bounces over the disks). Detailed description is given in the corresponding paragraphs.

## 4.1 Pump and seed beams

### 4.1.1 Pump laser and imaging optics

The Yb:YAG disks used in the system are pumped by 940nm CW lasers *LDM 4000-100* from *Laserline GmbH*. They provide up to 4kW of output power that can be delivered to the disks via 10m long flexible glass fibers with the core the diameters  $d_{core} = 1\text{mm}$ . The fiber output presents a divergent multi-mode beam: it is a combination of several TEM combined into an almost flat-top beam. The beam is collimated with one of the manufacturer-provided water-cooled collimation units equipped with two inches diameter lenses with different optical powers. The smallest available (by using one of those standard collimation units) beam diameter  $d_p = 34\text{mm}$  corresponds to the collimation lens with a focal length  $f_{col} = 80\text{mm}$ . This value is important for controlling the pump beam size on the disk.

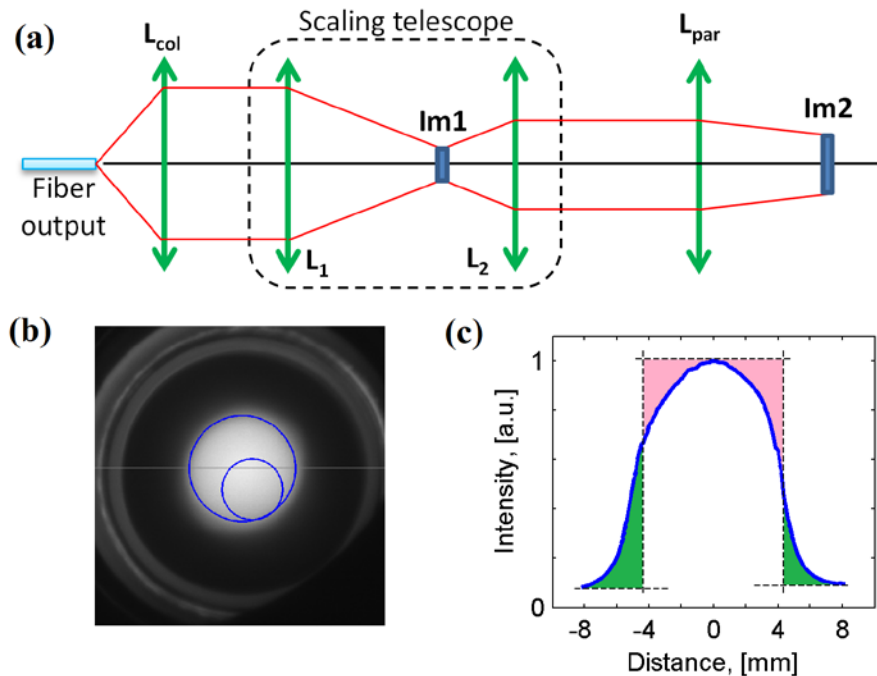


**Figure 4-1: Pump beam imaging.**

(a) A multi-mode beam with the divergence of  $0.22\text{rad}$  is collimated with a lens  $L_{col}$ . The lenses  $L_1$  and  $L_2$  scale the beam to the proper size. The final image of the fiber output ( $Im2$ ) is re-imaged to the disk several times by roof prisms and a parabolic mirror, creating a pump spot. Its size can be calculated via the equation 4.1. (b) Fluorescence of the pumped disk recorded with a camera. The pump spot diameter is  $10\text{mm}$ , the disk –  $20\text{mm}$ . (c) Horizontal lineout of the pump spot intensity profile (along the gray reference line). Due to imaging imperfectness it has not an ideal flat-top shape, but rather a super-Gaussian shape. The effective diameter corresponds to the rectangular approximation with the equivalent peak and integral intensities (the green and the pink areas are equal).

As it is described in section 3.3.1, a disk pump head has a parabolic mirror inside that with the help of roof prisms images the pump beam to the disk. The pump heads used in the current system provide 44 bounces, all of which present a scaled and stretched to an ellipse (the stretching factor depends on the internal pump head structure) image of the fiber output. In case of correct in-coupling all those ellipses partially overlap and form a round pump spot with a relatively sharp edge of the intensity profile (**Figure 4-1b**). The final pump spot size depends

on the collimation unit, scaling lenses, parabola curvature and the ellipse-stretching factor  $\alpha$  that is also defined by the pump head structure. This dependence can be expressed by the following equation:

$$D_{PS} = d_{fiber} \frac{f_1 f_{par}}{f_2 f_{col}} \alpha \quad (4.1)$$

where  $f_1, f_2$  and  $f_{col}$  are the focal lengths of the scaling lenses and the collimation unit,  $\alpha \approx 1.3$  and  $f_{par} = RoC_{par}/2 = 80mm$ .

### 4.1.2 Pump and seed spot sizes

For efficient energy extraction the amplified beam should stay within the pumped area at each iteration. The size ratio between the pump and the seed spots is an important parameter, affecting the system stability, amplification and the output profile. It can be numerically expressed as  $R_{SP} = D_{SS}/D_{PS}$  with a remark, that the seed beam is almost Gaussian and its diameter is defined at  $1/e^2$  level while the pump spot profile looks more like a super-Gaussian (**Figure 4-2a**) and the best way to define its size is to use 50% of the maximum intensity level. This is important for numerical calculations, where the pump spot has to be approximated with a perfect flat top shape with the equivalent peak (plateau) and integral intensities (**Figure 4-1c**).

With a fixed pump power smaller spot size means higher photon flux, which according to the electron dynamics equations **3.21–3.23** increases the population of the upper energy level and thus improves the gain. Theoretically the gain cannot continuously increase with the pump intensity because of saturation of the upper level: at some pump intensity the inversion of the population is so high, that the probability of the pump photon absorption is lower than the total emission probability (spontaneous and stimulated) at the pump wavelength, which means that further increase of the pump flux does not lead to a higher gain. But in reality the amplifier is aimed to work in kilohertz regime, what corresponds to  $<1ms$  between sequential seed pulses with hundreds millijoules of energy. The upper state population should be significantly depleted by such a strong seed and will not reach saturation within 200ms while being pumped by a CW laser.

Moreover, the bigger is the pump spot, the higher are the losses for *amplified spontaneous emission* (ASE), which takes place when a spontaneously emitted photon propagates – in random direction – within the pumped part of the disk. Presence of such photons can also trigger stimulated emission, which is not coherent to the seed beam and therefore just depopulates the upper state. If a spontaneously emitted photon propagates in the normal (or close to normal) direction, its path within the inversely populated area is very short and the probability of unwanted stimulated emission is quite low. But if it propagates in the longitudinal direction, the propagation path and time can be significantly longer and the corresponding probability is proportionally higher. Furthermore, according to the equation **3.23** emission of a new coherent photon additionally increases the probability of each consecutive emission event, which means that the losses grow nonlinearly. Thus making the pump spot smaller is beneficial for amplification not only because of the higher pump flux, but also because of strong dependence of the ASE losses on the pump spot size [57].

## Chapter 4: Multipass amplifier

However, there are some limiting factors that do not allow to decrease the pump area too much. The first limit is directly connected to the crystal damage that could occur due to high pump intensity. Though the low thickness and good thermal properties of Yb:YAG provide very efficient cooling, a pumped disk experiences significant mechanical stress caused by the temperature gradient between the pumped and not pumped areas [58]. With a sufficient cooling and energy extraction by the seed beam (which reduces non-radiative relaxation and corresponding temperature increase) a thin-disk can be safely pumped with the intensity of 6–8kW/cm<sup>2</sup>. With the maximal power of the pump lasers  $P_{p\ max} = 4kW$  such intensity can be reached by using a 9mm pump spot. It is of course possible to use a smaller pump spot, but then the full power of the pump units cannot be utilized and the upper limit of the pump power should be correspondently recalculated and controlled.

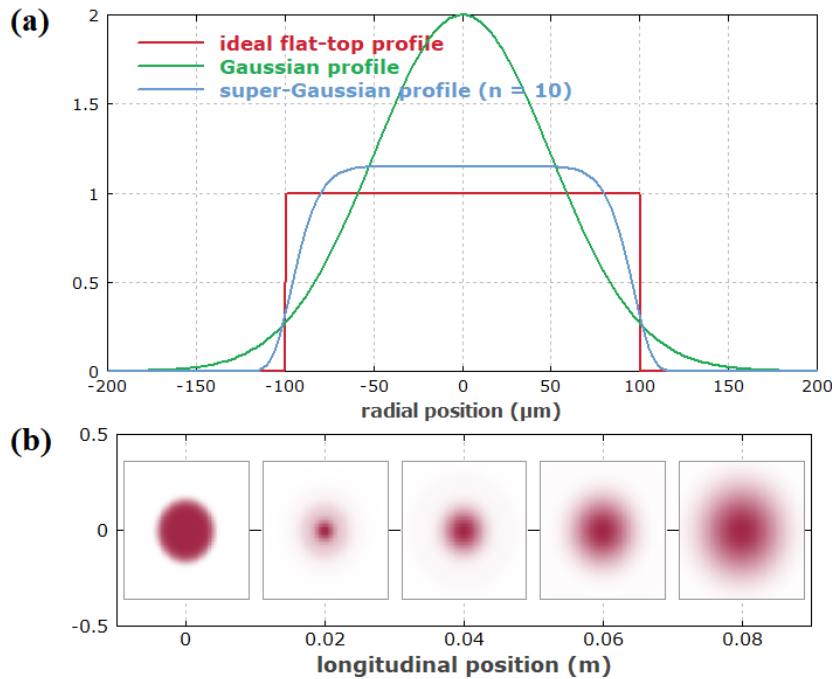


**Figure 4-2: Super-Gaussian beam.**

(a) Comparison of intensity profile (1D) of a pure Gaussian, flat-top and a super-Gaussian beam. (b) Change of the intensity profile (2D) during propagation for a super-Gaussian beam. Figures are taken from [59].

Another factor affecting the pump spot dimension is connected to the seed beam size and the damage threshold of the disks and mirrors: smaller beams have higher probability to damage the optics. Due to this the beam is usually as big as the laser system can support without having any clipping and aperture effects. When the mirror or just an opening is not big enough for a given beam ( $d_A \leq 2D_{seed}$ ), it reflects or transmits only the central part of the Gaussian beam. Though the energy content in the external part does not exceed 5%, the reflected/transmitted beam is not a Gaussian anymore and its propagation is different from the expected: a beam that is different from the free space modes does not preserve its intensity distribution and its wavefront evolves differently while propagating through a system designed for a Gaussian mode. A good example is a super-Gaussian (high order Gaussian) beam [59]:

$$I(r) = I_0 e^{-\frac{(r-r_0)^2}{2\sigma^2}}^n \quad (4.2)$$

## 4.1 Pump and seed beams

It is just a Gaussian beam with an exponent in the power of  $n$ , which leads to smoothing of the peak into a flat plateau and increase of the side slopes. The corresponding intensity profile is shown in **Figure 4-2a**. During propagation such a beam changes: being almost flat-top in the beginning, it can turn into a normal Gaussian or even into *Airy pattern* [60] – a high-intensity spot, surrounded by the regions with higher and lower intensity, which can be described by Bessel functions. The more often a beam passes through an aperture and the smaller this aperture is, the more it behaves like a super-Gaussian beam. In order to avoid this *hard aperture effect* all the optics should have a size of at least 3 times the beam diameter. This automatically means that the seed beam size should not exceed 7mm for 20mm disks used in the system. But there are additional spatial problems caused by the pumping and amplification.

While being pumped, disks experience thermal deformation. The pumped part of the disk rises above the rest of the disk surface what increases optical path of the central part of the beam comparing to the external part (**Figure 4-3a**) [61, 62]. This difference is quite small, but the seed beam is supposed to bounce many times over the disks surface, which means that the total accumulated difference might be significant. Moreover, only the central part of the seed beam (which overlaps with the pumped area) is amplified, while the outer part is just reflected. A single pass just creates a small break in the slope curvature, but repeating it multiple times leads to a sharp cut in the intensity profile, that is comparable to passing through a real aperture (**Figure 4-3b**). Such spatial beam distortions – they can be called *soft aperture effects* – also lead to degradation of the beam quality.

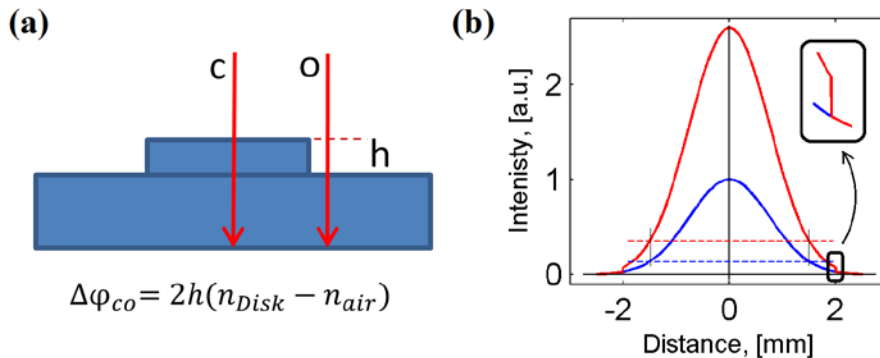


**Figure 4-3: Spatial beam distortions related to the pump spot size.**

(a) Pumped area of the disk rises above the rest of the surface. Due to this the central part of the seed beam (marked with C) accumulates a phase difference  $\Delta\varphi_{CO}$  relatively to the outer part of the beam (marked with O) at each bounce over the disk. (b) Demonstration of the break in the seed beam intensity profile at the edge of the pump spot. A Gaussian seed beam (blue) with  $D_{SS} = 3mm$  is amplified  $\sim 2.7$  times (red) only within the pump spot having the size  $D_{PS} = 4mm$ . Though the beam diameter does not change and stays smaller than the pump spot (shown with the dashed lines for both curves), a break in the intensity profile (shown zoomed) appears.

Due to these effects the originally estimated spot sizes ratio  $R_{SP} \approx 80\%$  – which is safe for the pump power of 4kW, pump spot  $D_{PS} = 9mm$  and the seed spot  $D_{SS} = 7mm \approx \frac{1}{3}D_{disk}$  and which would lead to very efficient pumping, energy extraction and low damage probability – is expected to be too high and is reduced to 50% ( $D_{PS} = 10mm$  and  $D_{SS} = 5mm$ ) for the first amplification tests. The exact numbers and the corresponding analysis of the beam quality will be described in section 4.2.

## Chapter 4: Multipass amplifier

One more important point to discuss is the change of the beam profile in case of significant depletion of the disk. The stronger is the seed, the lower is the population inversion after every bounce and the lower is the gain at the next iteration. But a Gaussian beam is always much more intense in the center what leads to spatial inhomogeneity in the upper level population and thus in the gain. This effect is almost negligible when the seed is relatively weak (for a given pump intensity) and the population does not change a lot even in the area corresponding to the center of the seed beam. But if the seed is too strong, it can be immediately seen in the output beam profile. This process can be well described by a simple 1D numerical model, based on few assumptions:

1. Single disk is presented by a 2-level system; the upper level is initially homogeneously populated while the lower one is empty. There are only stimulated emission and absorption at  $\lambda = 1030nm$  (no pump, no spontaneous emission). The total energy stored in the disk (within the pump spot) is  $E_{total} = 300mJ$ .
2.  $D_{PS} = 10mm$ , seed beam is a Gaussian with  $D_{SS} = 3mm$  at  $1/e^2$  level. Its energy is defined by the corresponding integral:  $E_{in} = \int I(x)dx$ .
3. Amplification at every iteration follows the next equation:

$$I_{k+1}(x) = I_k(x)e^{(N_{up_k}(x)\sigma_{em} - N_{low_k}(x)\sigma_{abs})} \quad (4.3)$$

The emission and absorption cross-sections are based on real values ( $2.5 \times 10^{-20}cm^2$  and  $0.5 \times 10^{-20}cm^2$  correspondently) and calibrated for 1D case.

4. After amplification the population distribution of the upper and the lower levels is recalculated according to the differential energy growth at the given coordinate:

$$\begin{aligned} N_{up_{k+1}}(x) &= N_{up_k}(x) - \frac{I_{k+1}(x) - I_k(x)}{\hbar\omega} \\ N_{low_{k+1}}(x) &= N_{low_k}(x) + \frac{I_{k+1}(x) - I_k(x)}{\hbar\omega} \end{aligned} \quad (4.4)$$

The results of such a simulation are presented in **Figure 4-4**. Subfigures (a), (b) and (c) correspond to 5, 15 and 150mJ input pulse energies and 17 bounces over a single 150 $\mu$ m disk, i.e. 34 passes through the active medium. Comparison of the blue and the red lines gives an idea of amplification while the dashed blue line serves as a reference of a normal Gaussian shape with the same 3mm diameter. It is clearly seen how a normal Gaussian beam turns into a triangular shape when population of the upper state reduces. For 15mJ the central part of the pump spot is already strongly depleted, but according to the equation 3.33 such a ratio ( $N_{1:2} \approx 1 : 5$ ) still provides some positive, though quite low, gain – because for 1030nm the emission exceeds the absorption  $\sim 25$  times. For 50mJ there is almost no gain for the very center of the beam because the population distribution reaches the ratio  $N_{1:2} \approx 1 : 20$  (according to equation 3.33 ratio  $N_{1:2} = 1 : 25$  corresponds to  $g = 0$ ). At the same time the outer part of the beam experiences significant amplification, what rises the sides intensity relatively to the peak, transforming a Gaussian into a triangle.

## 4.1 Pump and seed beams

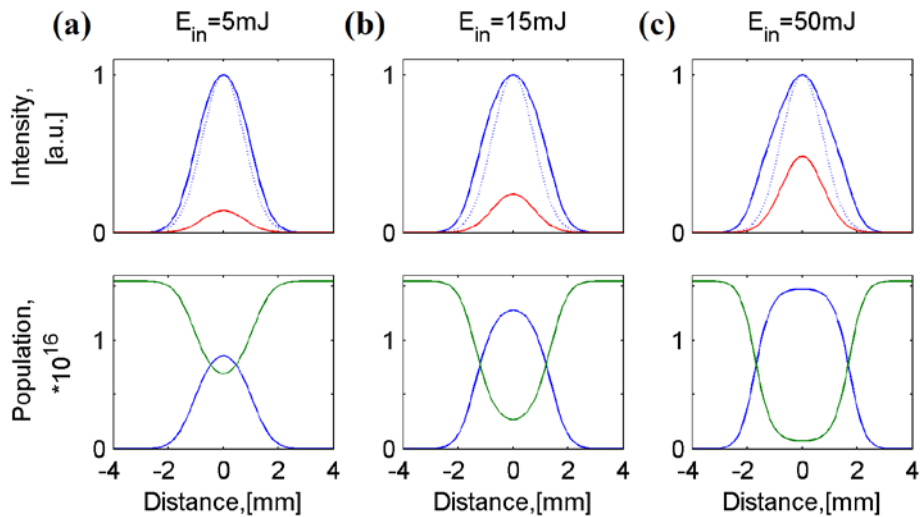


**Figure 4-4: Simulation of the population depletion for different seed powers.**

Subfigures (a), (b) and (c) correspond to 5mJ, 15mJ and 50mJ input pulse energies respectively. Top figures represent the normalized intensity profile of the output beam (blue). Red curves show the input Gaussian beam. Dashed blue lines show the reference Gaussian with the diameter equal to the input beam. Bottom figures show the spatial population distribution of the upper (green) and the lower (blue) level.

This process can be better understood by controlling the shape change at different iterations. **Figure 4-5** shows the intermediate profiles, corresponding to 50mJ input pulse energy. It nicely demonstrates that the beam slowly degrades from the very beginning and preserves acceptable shape until the bounce 9. Starting from this point the intensity profile changes (degrades) much faster due to significant difference of the gain in the depleted center and relatively well populated sides.

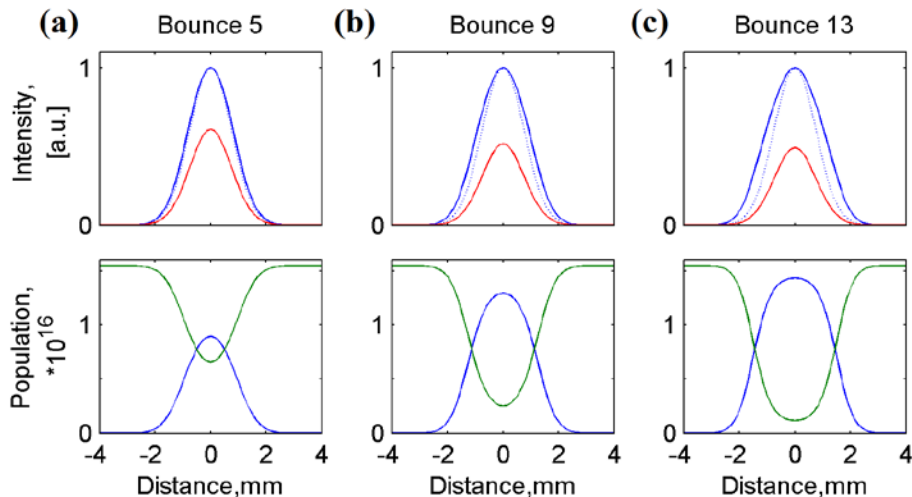


**Figure 4-5: Progressing population depletion during strong seed amplification.**

Subfigures (a), (b) and (c) correspond to 5, 9 and 13 bounces respectively. Top figures represent the normalized intensity profile of the output beam (blue). Red curves show the input Gaussian beam. Dashed blue lines show the reference Gaussian with the diameter equal to the input beam. Bottom figures show the spatial population distribution of the upper (green) and the lower (blue) level.

## Chapter 4: Multipass amplifier

Of course, the real process is more complicated: spontaneous emission plays an important role in the population dynamics, initial distribution is far from being homogenous, etc. But this effect was well reproduced in the lab (**Figure 4-6**), which means that in a first approximation the above described model is good enough. Detailed explanation of the optical scheme will be given in the next section. Subfigures (a) and (b) demonstrate two output beam profiles with the same seed power  $P_S = 100W$  (20mJ at 5kHz) and two times different pump powers. At  $P_P = 500W$  the output beam profile has a smaller slope and a significantly bigger (+17%) diameter. In this example the beam still stays Gaussian, but in general a strong inhomogeneity of the gain caused by depletion can modify the intensity distribution so much, that the beam stops being a free-space mode. Thus the beam will not only have worse quality and focusability, but also unwanted modifications of the intensity profile during propagation (as it happens with a flat-top beam) that can lead to optics damage. At  $P_P = 1000W$  the output beam returns to its normal size, which means that the initial population of the upper level is higher and it does not drop so much during amplification. Notably, the normal beam size at this pump power is  $\sim 5\%$  smaller than in a cold state (**Figure 4-6c**) due to a slight increase of the disk curvature caused by the pumping. This effect will be discussed further in paragraph 4.2.3.

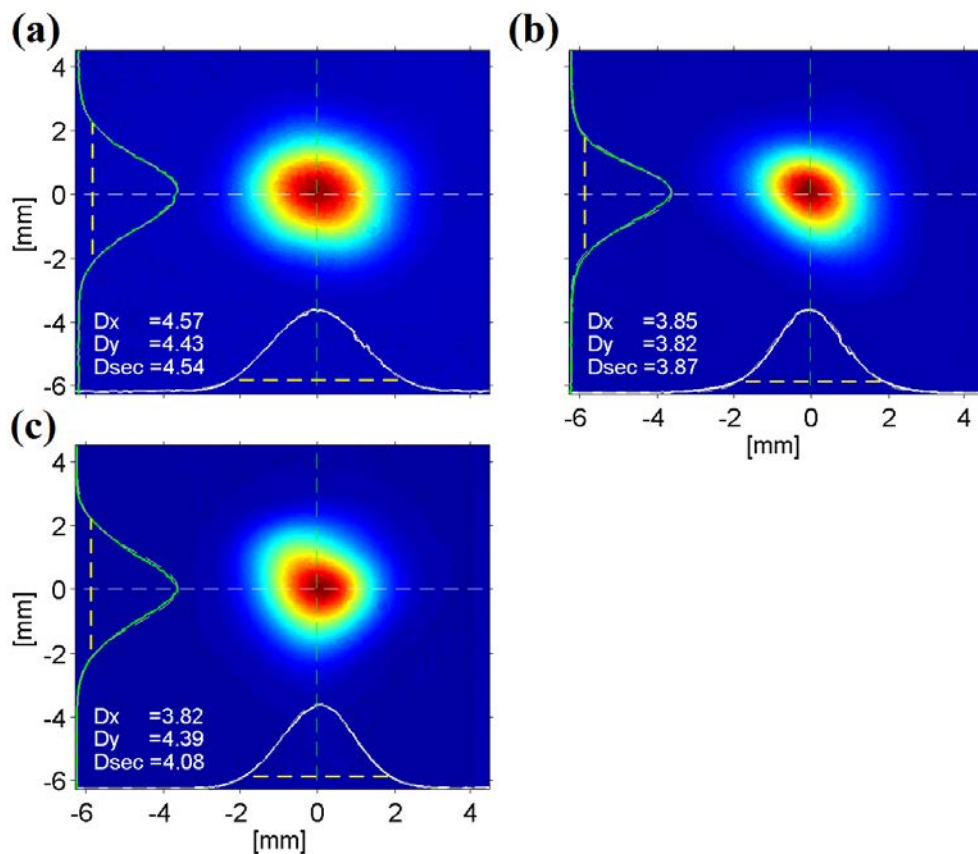


**Figure 4-6: Output beam profile in case of significant depletion.**

(a) Pump power is not enough for a given seed. Lower gain in the center leads to relative magnification of the sides. Beam profile still stays Gaussian, but its diameter increases.  $P_P = 500W$  ( $I_P \approx 630W/cm^2$ , CW),  $P_S = 100W$  ( $E_S = 20mJ$ , 5kHz). (b) Increase of the pump power to  $P_P = 1000W$  ( $I_P \approx 1260W/cm^2$ ) makes the gain spatially more homogeneous, output profile returns to its normal size and shape. (c) Output beam profile in case of weak seed ( $P_S = 1W$ ) and no pump. Slightly triangular shape in (b) and (c) is normal and connected to the triangular shape of the source laser mode.

## 4.2 Imaging configuration

These simulations and experimental observations lead to an important conclusion: amplification of a too strong seed can lead not only to a low gain factor, but also to the change of the beam profile. Such a change implies a different evolution of the beam during propagation through the system, which can induce the optics and crystals damages. In order to get a reference value for this phenomenon, the pumped energy can be compared with the extracted energy. In the first case a 100W (20mJ at 5kHz) seed was amplified twice, what means that ~10mJ is extracted from each of the two disks within 0.2ms. Taking into account  $P_p = 500W$ , ~45% seed-to-pump spot sizes ratio and 9% quantum defect loses, the maximum energy available in the seed area (without any loses) is ~40mJ. Thus 25% extraction of the maximal available energy is too much and leads to ~17% bigger beam size comparing to the well-pumped case, which corresponds to ~12% extraction and a normal beam size and shape. Of course, the upper level population depends also on the spontaneous emission, non-radiative relaxation and the repetition rate. Moreover it cannot be depleted completely, so not all the stored energy is available for extraction. But these two numbers can serve as reference values for estimation of the minimal necessary pump power for further amplification.

## 4.2 Imaging configuration

### 4.2.1 Principle of $4f$ -imaging

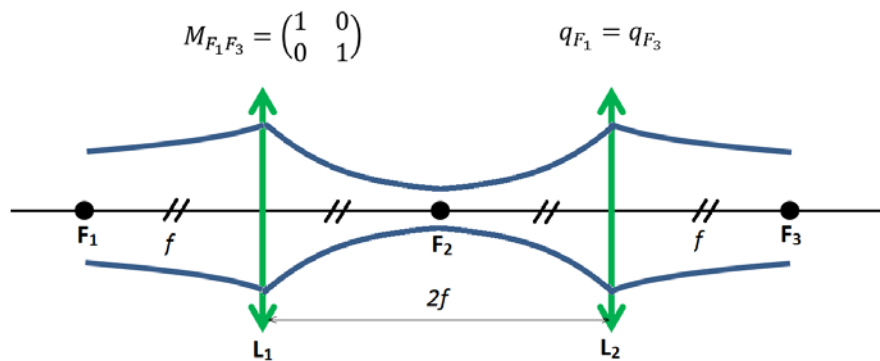


**Figure 4-7:  $4f$ -imaging.**

Two lenses (or curved mirrors) with the focal length  $f$  are separated by the distance  $2f$ . Beam transformation matrix between the points  $F_1$  and  $F_3$  is uniform, thus beam size and divergence (as well as Rayleigh range) do not change. Repeating this structure several times leads to completely identical beam propagation at each iteration.

Due to low thickness of the gain medium efficient energy extraction requires significant amount of passes, which in turn means significant total propagation length in the amplifier. In contrary to resonators, where a seed beam bounces over the same optical elements allocated on the plane optical table or breadboard, in a multipass it leads to a large number of the beam segments laying in different planes at different heights. For efficient amplification all the *bounces* – segments of the seed beam that belong to different iterations – should overlap within the pump spot and form a single seed spot. Long and complicated beam path raises the problem of preserving this overlapping during the operation at high power: high thermal load causes the heating of mechanical components, which are responsible for the alignment, and thus disturbs the correct propagation of the seed beam through the amplifier.

## Chapter 4: Multipass amplifier

The imaging concept [63, 64] is one of the simplest and most reliable solutions of the overlapping problem. The idea is that at each iteration the seed spot on the disk is reimaged to the same position preserving its size and shape. It can be performed by using curved mirrors for imaging and flat mirrors for steering the beam. **Figure 4-7** shows the optical scheme of  $4f$ -imaging. Two lenses with the focal length  $f$  are separated by a distance  $2f$ . In such a configuration any object placed at the front focus of the first lens is one-to-one reimaged to the rear focus of the second lens. It can be easily shown in terms of ABCD approach:  $M_{full} = M_f M_{2f} M_L M_f = \begin{pmatrix} 1 & 0 \\ 0 & 1 \end{pmatrix}$ . So if a Gaussian beam reaches the point  $F_1$  having the waist  $\omega_0$  and being perfectly centered relatively to the central optical axis, it has exactly the same size and divergence and is also perfectly centered at the point  $F_3$ . Thus repeating the imaging several times allows to reproduce exactly the same beam at each iteration.

From the imaging point of view such an optical system does not require the input beam to be collimated – any beam is reimaged. But if the divergence is too big, the beam can expand too much while propagating and its size can exceed the value supported by the used optics. It does not disturb the imaging, but causes energy losses and clipping on the edge of the optics, which in turn negatively affects the beam profile between the imaging planes and can lead to optics damages. Thus it is safer to image a roughly *collimated* beam – its waist  $\omega_0$  should be as close to the input image plane (point  $F_1$ ) as possible.

### 4.2.2 Realization of $4f$ -imaging with two disks

Development of the resonator-based laser demonstrated, that usage of two thin disks is very beneficial for amplification, though it is much more complicated in alignment and operation. Numerical simulations (see **Appendix A**) also show that a single disk is not enough for reaching the output pulse energy above 200mJ (maximum pulse energy of the source laser in the normal 5kHz operation regime). In order to realize  $4f$ -imaging approach with two disks within some reasonable dimensions extra folding mirrors are required. **Figure 4-8** demonstrates the corresponding optical scheme with the beam propagation path within the first iteration.

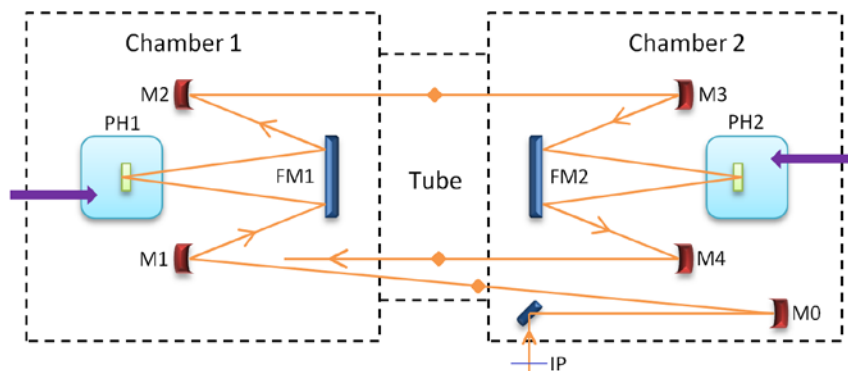


**Figure 4-8: Multipass  $4f$ -imaging scheme.**

Single iteration includes 4 bounces over the imaging mirrors (M1–4), two disks (green rectangles in the pump heads PH1–2) and two flat folding mirrors (FM1–2). After the last mirror M4 the beam is sent to the M1 belonging to the next iteration. Rhombus show the foci position. Mirrors M0 and M1 also perform the function of the input imaging cell that images the input plane (IP) to Disk1. Purple arrows correspond to the position of the pump beam in-coupling optics. Dashed lines present the borders of the vacuum chambers and the connection tube.

## 4.2 Imaging configuration

The key elements are the curved mirrors (M1–4) that perform the imaging. Their curvature and positions correspond to the scheme presented in **Figure 4-7** with  $f = 1.5m$ . The folding mirrors are needed for optimization of the lab space usage. Without them the disks would have to face into opposite directions, what would significantly increase the setup dimensions due to the free space behind the pump heads necessary for the pump optics. Each iteration contains two foci, where the light intensity is significantly higher than at any other part of the beam path. Though the seed pulse is stretched to 2ns duration, such a tight focusing can induce the air ionization when the seed pulses become significantly amplified. To avoid the energy losses and the beam degradation caused by the ionization all the setup is sealed in a vacuum cell, consisting of two big chambers and a connecting tube (**Figure 4-9**). Usage of a vacuum scroll pump unit allows to keep the pressure inside the chambers below 1mBar, what should completely solve all the ionization-related problems.

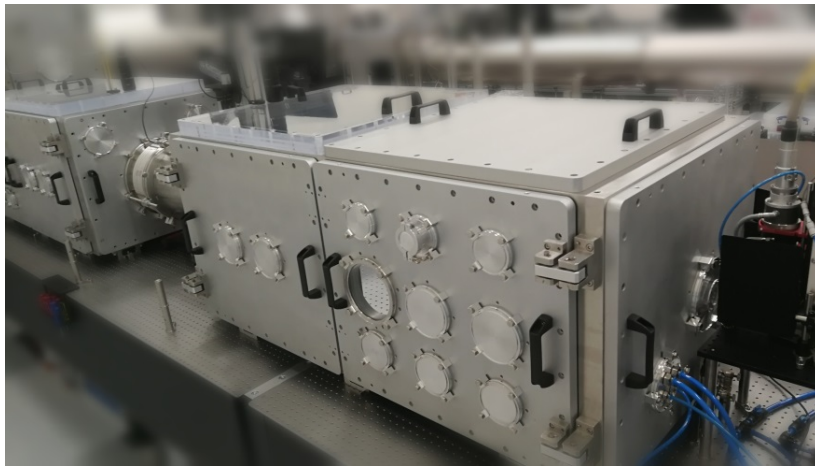


**Figure 4-9: Vacuum chambers.**

Optical components of the amplifier are installed in two vacuum chambers with the dimensions of 0.65x0.75x1.6m, which are connected with a 1m length 0.32m diameter tube. Optical breadboards inside the chambers are attached to the optical tables and are mechanically isolated from the chambers frame via special flexible bellows-tubes in order to avoid possible misalignment during the air evacuation. Front doors of the chambers are installed on the hinges for easier access to the optical components. In- and out-coupling of the seed and pump beam occurs via the windows on the rear and side walls of the setup according to the scheme presented in the **Figure 4-8**.

Mirror M0 together with M1 (1<sup>st</sup> iteration) present an additional  $4f$ -imaging cell that helps controlling the beam propagation. First of all it gives access to the beam that is sent to the system. According to the imaging principle, the beam that comes to the first disk is continuously re-imaged to the second disk and back. But all the imaging planes lay within the disk pump heads and are not accessible for diagnostics. The input imaging cell sends to the system (to the first disk) the image of the beam from the input imaging plane (IP, shown with a blue line in **Figure 4-8**), which is easily accessible for any measurements. The second advantage of using this cell is that a special imaging-based method can be used for precise alignment of the beam position within the pumped area of the disk. A thin needle inserted in the input beam at the IP creates a sharp (in case of properly defined optics position) shadow in the beam on both disks at each iteration. Since human eye distinguishes sharp edges much better than the intensity distribution within a round beam, such an approach makes overlapping of the seed bounces significantly more precise.

## Chapter 4: Multipass amplifier

At each iteration  $k$  all the segments of the beam between M1 and M4 lay in a single plane. The last mirror M4 sends the beam to the mirror M1 of the next iterations  $k+1$  and the full propagation cycle repeats: the beam is again send to FM1, then to Disk1 and so on. Such propagation scheme is realized by using metal frames (so called *mirror wheels*) that are holding twenty 1-inch imaging mirrors, symmetrically located around the axis Disk1–Disk2. This axis appears to be an intersection of all the twenty planes which are tilted by  $360^\circ/20 = 18^\circ$  relatively to each other. **Figure 4-10** demonstrates a part of a mirror wheel and a folding mirror with scattered beams.

This optical setup provides in total 19 bounces (38 passes through the crystal thickness) over two disks: 9 full iterations where the beam bounces over both disks and one additional bounce over the first disk. Afterwards, instead of sending the beam to the 20<sup>th</sup> bounce over Disk2, mirror M3 (10<sup>th</sup> iteration) is used for the beam out-coupling. Together with mirror M4 (10<sup>th</sup> iteration) it forms the output imaging cell, which in analogy to the input imaging cell brings the beam from the last bounce over Disk1 to the output imaging plane, which is located outside the vacuum chambers.

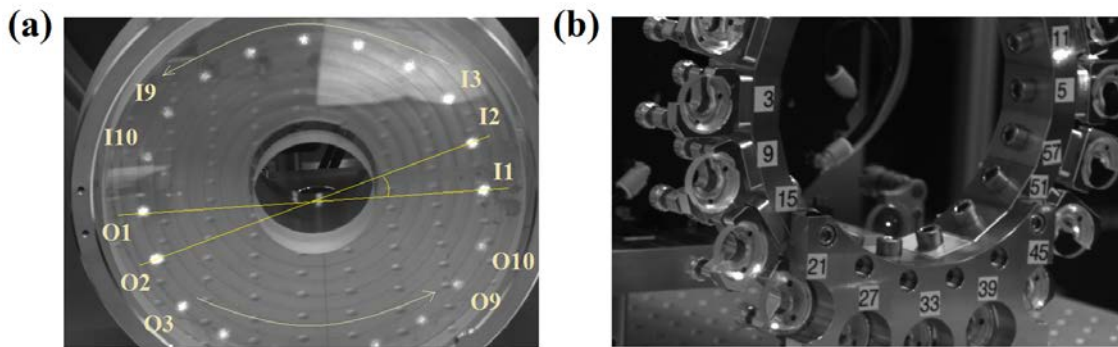


**Figure 4-10: Folding mirror and imaging mirrors.**

(a) 7-inches flat folding mirror. A 2-inches hole in the center is used for observing the disk with a camera in order to control the seed beam position during operation. The top half-circle (scattered light) correspond to the beams that are sent to the disk (I1–10), the bottom – reflected from the disk (O1–10). (b) The frame of the imaging mirrors array – mirror wheel. Top mirrors sent the beam to the folding mirror and the disk, bottom ones steer the beam returning from the disk to the second frame and the second disk. Big openings in the frames are needed for propagation of the beam between the disks and the folding mirrors.

### 4.2.3 Beam propagation

Completely identical propagation of the beam at each iteration requires the disks to be flat and installed exactly at the front and rear focii of the curved mirrors. However the most flat available samples have the curvature of  $\sim 20\text{m}$ , which means that they have the optical power equal to a mirror having 10m focal length. In this case full transformation matrix of a single iteration is not uniform, but has a non-zero element  $C$ . Optical system with such a matrix still images the beam from the input to the output plane and its size there stay the same. But its divergence changes after each iteration:  $d_{i+1} = d_i$ ,  $\alpha_{i+1} = \alpha_i + D_i C$  – this leads to a change of the beam size between the disks. Thus on some curved mirrors the beam becomes too big and cannot be properly reflected while on the others it decreases and can be even focused what in turn can cause damage of those mirrors. This unwanted change of the beam divergence can be

## 4.2 Imaging configuration

compensated by changing the distance between the mirror wheels. For the mirrors used in the laboratory setup ( $f = 1.5m$ ) the distance between them should be reduced from 3m, corresponding to the pure  $4f$ -imaging scheme shown in **Figure 4-7**, to 2.77m. Such a shortening compensates the curvature of the disks and transformation matrix turns to unity again. **Figure 4-11** demonstrates the evolution of the seed beam inside the amplifier according to this compensated matrix. Beam size on the disk is always equal to the waist of the input beam. On the curved mirrors it is smaller, but also stays constant.

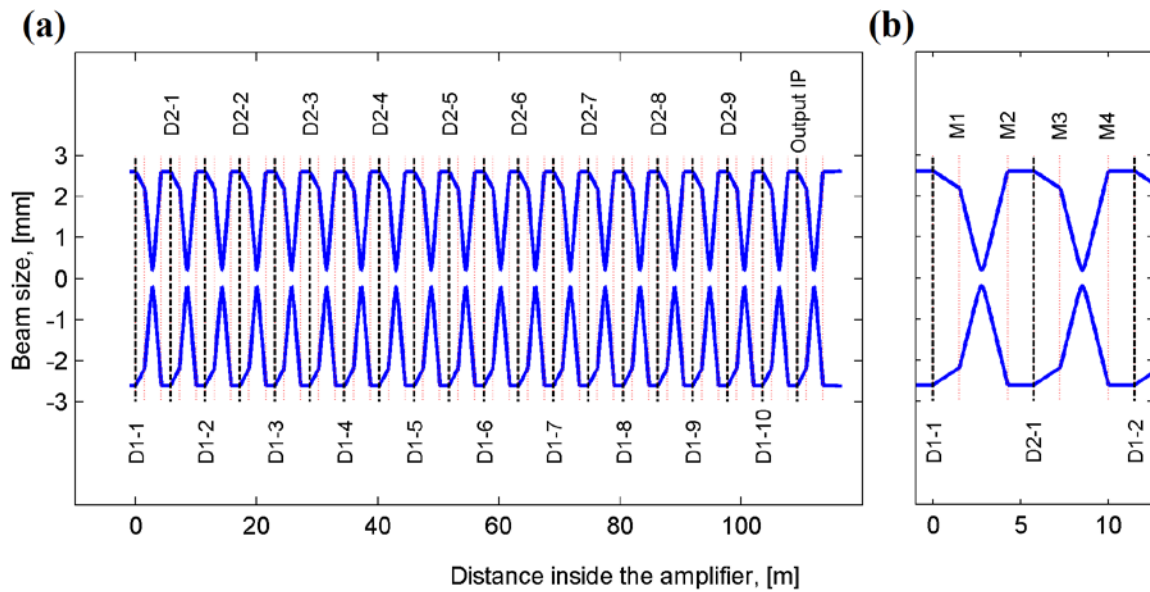


**Figure 4-11: Correct propagation of the seed beam inside the amplifier.**

(a) Full propagation through the system Blue dashed lines show the curved mirrors positions, black dashed lines – the disks positions and the output imaging plane. X axis shows the total propagation distance starting from the first bounce over Disk1. Y axis corresponds to the beam diameter scale: blue solid line shows the beam radius (at  $1/e^2$  level) in positive and negative direction. Collimated beam with the waist  $\omega_0 = 2.6mm$  experiences 9 full iterations plus one more bounce over Disk1, afterwards it is sent to the output imaging plane. (b) Magnified image of the first iteration. M1, M2, M3 and M4 – curved imaging mirrors of the first iteration. Second iteration starts at D1-2 – the second bounce over the first disk.

As it was discussed in paragraph 4.1.2, pumping of the disk creates a temperature gradient and a corresponding mechanical stress. This in turn affects the refractive index of the disk material making it spatially inhomogeneous. Such a change is called *thermal lens effect* [65] and is especially important for the regenerative amplifiers, because it modifies the eigenmode of the resonator. Thermal lens effect can be quantitatively described as modification of the disk effective radius of curvature – pumped disk becomes effectively flatter. According to some reports [65, 66] the change of the disk optical power can reach  $15\text{--}25\text{cm}^{-1}$ . Since the effective radius of curvature changes, the transfer matrix in pumped state is also different. **Figure 4-12** shows simulation of a moderate curvature change of  $30\%$ <sup>1</sup>. A non-uniform transformation matrix leads a continuously increasing deviation of the beam from its normal propagation. On some mirrors it becomes significantly bigger, what might cause clipping and/or lead to aperture effects, while on the other mirrors the beam is almost focused (**Figure 4-12b**). Such a

<sup>1</sup> Such a scale of the curvature change was experimentally during optimization of the source regenerative-type laser, described in paragraph 3.3.2.

## Chapter 4: Multipass amplifier

significant size decrease – almost 8 times in terms of area – inevitably leads to damages of those mirrors at high power operation.

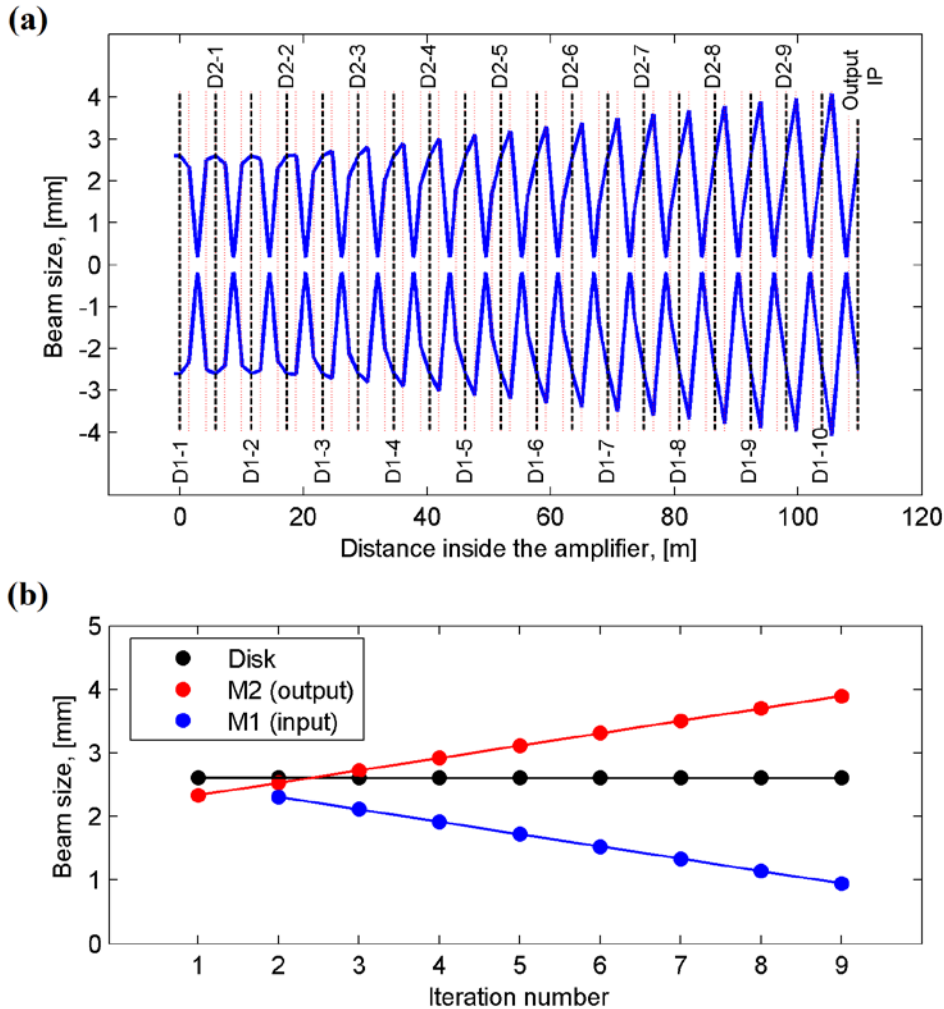


**Figure 4-12: Propagation change caused by the thermal lens effect.**

(a) This figure corresponds to **Figure 4-11** with a 30% bigger curvature of the disks. (b) Corresponding beam size on different optical elements. Input beam is collimated – its size is equal on M1 and Disk 1 at the first iteration.

Counteraction to this effect would be a partial back-shift of the curved mirrors towards original 3m distance – then the propagation would be wrong (similar to **Figure 4-12a**) without pumping, but would return to a normal one (**Figure 4-11**) when the effective curvature of the disks changes due to pumping. Unfortunately, this effect is too complicated for exact prediction and compensation. First of all it depends on the temperature distribution, which means that for every pump power, pump and seed spot sizes and seed input and output power (affecting the energy extraction) it will be different. The second point is that thermal lens effect can be well described as an effective change of the radius of curvature only in a resonator: non-spherical wavefront distortions just increase the losses, while the mode adjusts itself to the size that corresponds to the new effective curvature. This mode-size change can be canceled by recalculation of the resonator based on effective disks curvature at the given pump and seed beam power. In an imaging multipass amplifier all the distortions induced by the disk pumping are not suppressed but oppositely multiplied by re-imaging of the disk surface to itself leading

to significant degradation of the beam quality. It cannot be compensated by adjusting the distance between the curved mirrors – as it would be possible in case of pure spherical changes – and leads to a different propagation and degradation of the beam quality at high pump power.

### 4.2.4 Amplification and beam quality

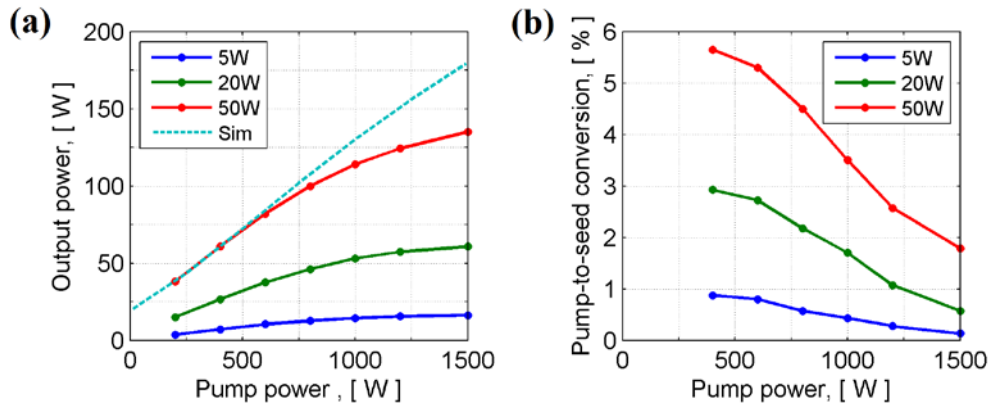


**Figure 4-13: Amplification curves.**

(a) Output power as a function of the pump power. Different colors correspond to different seed beam powers. Gray dashed line represents the numerical simulation the case of 50W see. (b) Discrete derivatives of the curves from the first subfigure – the growth of the output power normalized to the pump power increase. It shows how much power the seed beam obtains from each extra watt of pump power (0.5W per disk). Parameters:  $D_{PS} = 10\text{mm}$ ,  $D_{SS} = 5.2\text{mm}$ ,  $N_{bounces} = 19$ .

**Figure 4-13** shows the output power of the amplifier depending on the pump and seed power. Presented curves are in a good qualitative agreement with the basic light amplification principles described in paragraph 3.2.3: the output power demonstrates continuous sub-linear growth with the pump power increase. Subfigure (b) presents the corresponding derivative  $\frac{\partial P_{out}}{\partial P_p} \cdot 100\%$ , which can be interpreted as optical-to-optical efficiency of the amplifier and shows how much of each additional watt of pump power is transferred to the seed beam. Such a plot is useful to highlight few important points that are not obvious from the output power curves. The first one is better extraction of the pump energy by a stronger seed. The second one is the increase of the ASE at high pump power. Even for  $P_S = 5\text{W}$  the energy extraction efficiency decreases for higher pump powers which means a strong depopulation of the upper energy level. Since the stimulated emission is too weak (extracted power is below 10W for 1500W pump power per disk), the only mechanism left is the spontaneous emission and losses for its amplification.

Dashed line in **Figure 4-13a** presents the result of numerical simulations (see **Appendix B**) for the given pump and seed spot sizes. It agrees very well with the measured curve up to  $\sim 700\text{W}$  of pump power, but then demonstrates continuously growing disagreement that reaches +25% at  $P_p = 1500\text{W}$ . Such a difference is connected to the significant change of the seed beam profile (details are discussed later in this paragraph), that leads to worse energy extraction and does not allow reaching the expected values.

As it can be seen from the plot, applied pump power was limited by 1500W. This is connected to the thermally induced misalignment of the system. During amplification a significant shift of

## Chapter 4: Multipass amplifier

the seed beam, proportional to the total pump power applied to both disks, was observed. Imaging properties of the system preserve good overlapping of the seed bounces and their position within the pump spot on both disks, but not on the imaging mirrors. Beam displacement is proportional to the propagation length in the system, i.e. it is almost invisible during the first iterations but causes beam clipping on the edge of the mirrors that belong to the last iterations. All attempts to compensate this displacement by tilting the mirror wheels or folding mirrors were not successful, but similar behavior was obtained (without pumping) when disks were slightly misaligned by purpose. Moreover the observed translation is reproducible with respect to the pump: switching off the pump laser brings the seed to its correct position on the imaging mirrors within a few seconds, while switching the pump on again leads to the shift in the same direction and the same amplitude on all the mirrors. These observations indicate a disks-related genesis of the translation. Due to high thermal load some minor deformation in the substrate, glue layer or even the crystal volume lead to a small change of the beam reflection direction, which accumulates to a visible displacement after several iterations.

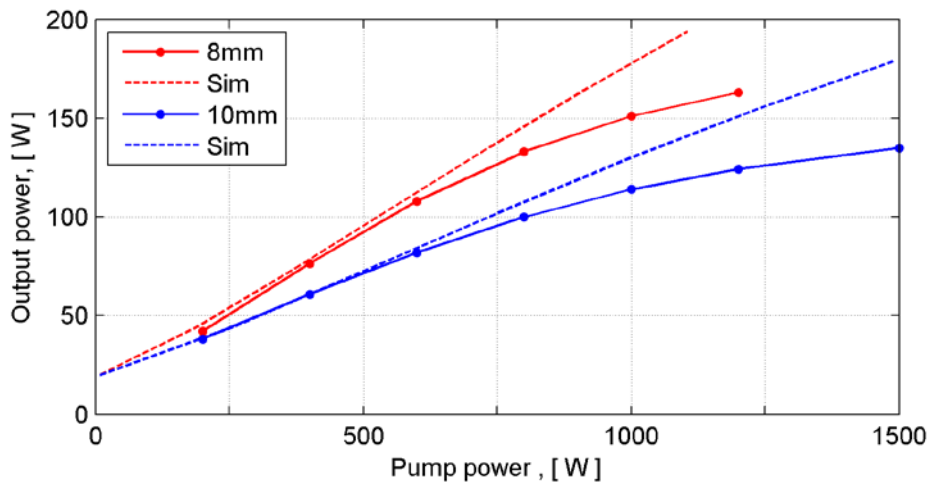


**Figure 4-14: Amplification in case of smaller pump spot.**

Comparison of the output power in case of 8mm (red) and 10mm (blue) pump spot. Dashed lines correspond to the simulations. Parameters:  $D_{SS} = 5.2mm$ ,  $P_S = 50W$ ,  $N_{bounces} = 19$ .

Beam deviation on the mirrors appears to be proportional to the total pump power and thus limits the amplification. On the other hand gain depends on the pump flux that can be increased by reducing pump spot size for the same pump power. **Figure 4-14** demonstrates comparison of the output power for two different pump spot diameters. For 8mm pump spot the pump flux ( $\sim 1/D^2$ ) is almost 30% higher what according to the simulations should lead to a comparable increase of the output power. The measured curve shows the same increase of the output power while the displacement on the mirrors does not change. Notably the difference between the measured and the simulated curves is bigger for 8mm spot: at 1kW pump power the difference is -12% for  $D_{PS} = 10mm$  and -17% for  $D_{PS} = 8mm$ . This observation agrees very well with the assumed reason: the bigger is the seed-to-pump spot sizes ratio, the stronger is the soft aperture effect and the corresponding beam degradation, which in turn leads to worse energy extraction.

However, increase of the seed-to-pump spot sizes ratio causes the problems with the beam profile, which were discussed earlier in paragraph 4.1.2. **Figure 4-15** demonstrates how the

## 4.2 Imaging configuration

beam changes after propagation through the amplifier. The input beam has the diameter ( $1/e^2$ ) of 5.2mm and an almost perfect Gaussian profile (subfigure **a**), that is significantly distorted after the full propagation through the system even without pumping (subfigure **b**). This effect can be connected to the natural roughness of the disk reflective surface or some minor spatial modulations of its thickness or refractive index: single reflection does not change the wavefront a lot, but imaging effectively multiplies the amplitude of any smallest single-pass phase distortion to the amount of bounces leading to such a significant change. Pumping makes the beam profile even worse, what is shown on subfigure (c).

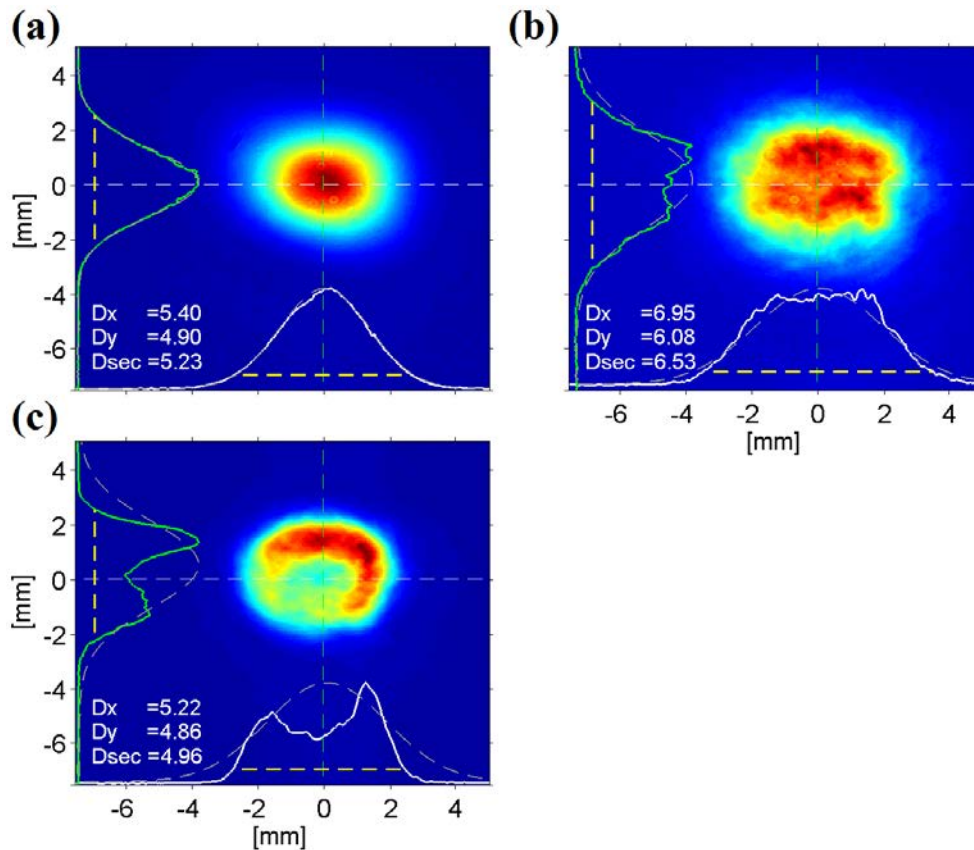


**Figure 4-15: Distortions in the output beam.**

(a) Input Gaussian beam with 5.2mm diameter ( $1/e^2$ ). (b) Corresponding output of the amplifier without pumping. (c) Output beam profile in case of pumping both disks with  $P_p = 1000W$ . Parameters:  $D_{SS} = 5.2mm$ ,  $D_{PS} = 10mm$ ,  $P_S = 1W$ ,  $N_{bounces} = 19$ .

The beam size does not change a lot, but a strong gap in the center appears. It corresponds to a significant increase of the intensity in the narrow circle between the center and the edge of the beam and can increase the probability of the disk damage. Evolution of these distortions can be well understood by comparing the output beam profiles with the intermediate ones corresponding to the half-propagation through the amplifier (after 5 iterations). **Figure 4-16** shows the beam that is sent to Disk1 on the 6<sup>th</sup> iteration and its modification caused by the pumping. In case of no pump (subfigure **a**) the output beam already looks worse than the input, but still much better than after the full propagation. It supports the idea of accumulation of the non-spherical distortions of the reflective surface after each additional bounce over the disk. Subfigure (b) shows further change of the beam profile caused by increase of the pump power to  $P_p = 1000W$ . Additionally to ~10% size reduce the genesis of the central gap can be

## Chapter 4: Multipass amplifier

distinguished: in the y-axis lineout its already a small dip in the intensity while in the x-axis lineout it's just a flattening of the peak and a relative rise in the near-peak area. It could be explained by the soft aperture and thermal lens effects that were described in paragraph 4.1.2. Comparison of these intermediate profiles with the output beam (**Figure 4-16b** and **c**) shows, that the pump-caused distortions add up with the disk surface imperfectness. The resulting beam degradation grows in nonlinear manner with the increase of the pump power and the amount of bounces over the disks.

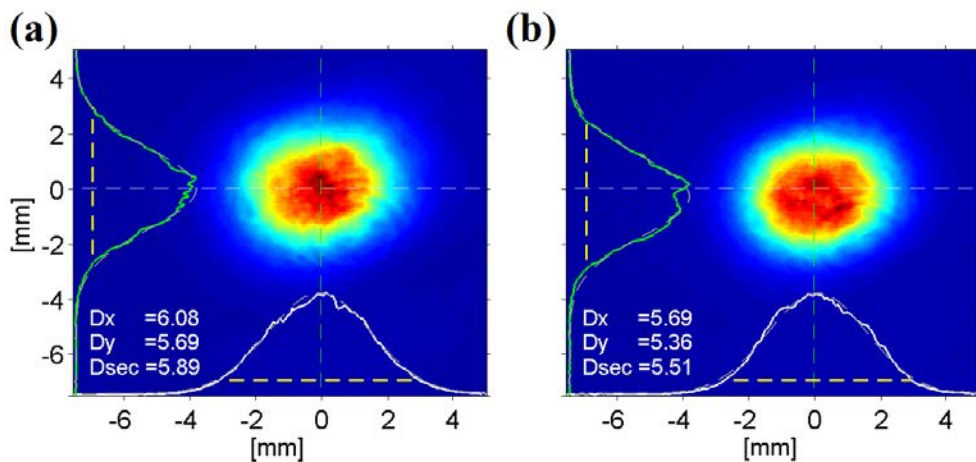


**Figure 4-16: Accumulation of the beam distortions.**

This is the beam profile corresponding to the 11<sup>th</sup> bounce over the disk. The beam is sent to a camera instead of the disk – with the same imaging distances. (a) No pumping. (b)  $P_p = 1000W$ . Parameters:  $D_{PS} = 10mm$ ,  $D_{SS} = 5.2mm$ ,  $P_s = 1W$ .

Even a stronger change in the seed beam intensity distribution can be observed on the curved mirrors that perform imaging during the last iterations. Increase of the pump power from 0 to 800W leads to approximately 25% change of the beam waist: increase on the output mirrors and decrease on the input ones (**Figure 4-12b**). Further pump power increase – up to  $P_p=1500W$ , which is a limit defined by thermal misalignment of the beam – not only changes the beam size, but also causes a pronounced aperture effect. On the input mirrors of the last 10<sup>th</sup> iteration (M1 and M3 in **Figure 4-8**) the beam profile turns into a narrow hot-spot surrounded by the rings of lower and higher intensity, similar to Airy pattern. Depending on the initial beam size its peak intensity can be 2–5 times higher than the value that corresponds to the normal propagation of a Gaussian seed beam. **Figure 4-17** demonstrates an example of such a hot-spot pattern, recorded during investigation of the aperture effects for different beam sizes.

As the result of such strong beam degradation, the above mentioned input mirror (M1 of the 10<sup>th</sup> iteration) was damaged several times consecutively by exceeding the output power of 300W. In order to reach this output power the pump power of 1700W ( $D_{PS} = 10mm$ ) was applied to both disks amplifying a 100W, 5.2mm diameter seed. Increase of the pump power above 1500W was only possible due to pre-compensation of the seed beam position on the imaging mirrors - by tracking the displacements on all the mirrors for a given pump and seed power and correcting it during the initial alignment of the system. It gave some extra space for the beam (before reaching the edges of the mirrors), which was utilized for applying higher pump power.

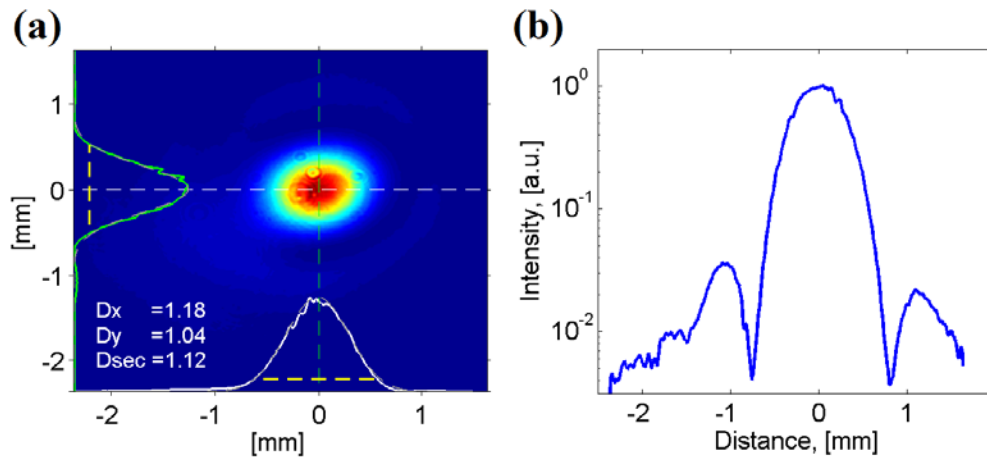


**Figure 4-17: Example of Airy pattern.**

(a) Beam profile corresponding to mirror M1 of the 10<sup>th</sup> iteration in case of a pronounced aperture effect. (b) Vertical lineout in logarithmic scale.

In order to investigate the beam degradation more detailed, another measurement with a significantly smaller  $R_{SP}$  was performed. For this purpose the seed spot was reduced to  $D_{SS} = 3.3\text{mm}$ , what in combination with a 10mm pump spot corresponds to the conventional empirical rule of triple-size apertures:  $D_A \geq 3D_{beam}$ . The obtained output beam profiles are presented in **Figure 4-18**. They clearly show that beam degradation is significantly lower in both pumped and unpumped conditions. It is expected for the soft aperture effect, but leads to a new conclusion for propagation through the unpumped system. Such an improvement is only possible, if the central part of the disk (within 3mm according to the beam size) is more homogeneous comparing to the outer area – which could mean roughness and sphericity of the disk reflective side or spatial homogeneity of its thickness and refractive index – and a smaller beam experiences less wavefront distortions at each iteration.

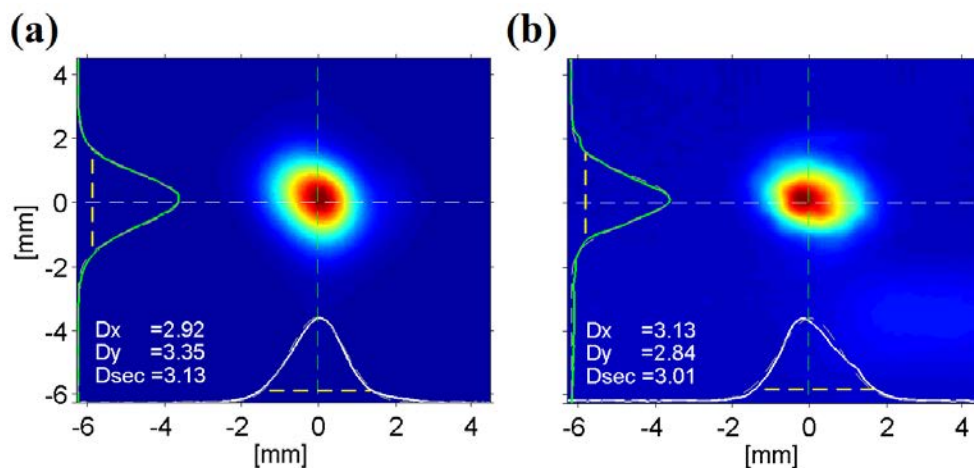


**Figure 4-18: Output beam profile in case of smaller seed beam.**

(a) No pumping. (b)  $P_p = 1400\text{W}$ . Parameters:  $D_{PS} = 10\text{mm}$ ,  $D_{SS} = 3.3\text{mm}$ ,  $P_S = 1\text{W}$ ,  $N_{bounces} = 19$ .

## Chapter 4: Multipass amplifier

Unfortunately such a modification cannot provide any significant amplification due to extremely low efficiency: the energy extraction area reduces  $\sim 2.5$  times, which leads to a comparable drop of the total gain (in comparison with  $D_{SS} = 5.2mm$ ). Numerical simulations (**Figure 4-19**) show the same: up to 1700W of pump power only a weak 50W seed demonstrates any significant, though quite low, amplification with the total gain  $G \approx 3.5$ . For a stronger seed amplification is lower or even turns to absorption, because the seed flux becomes too high for the pump flux, which is limited by thermal misalignment. Thus such a big seed-to-pump spot sizes ratio cannot be used for efficient amplification and reaching high output power.

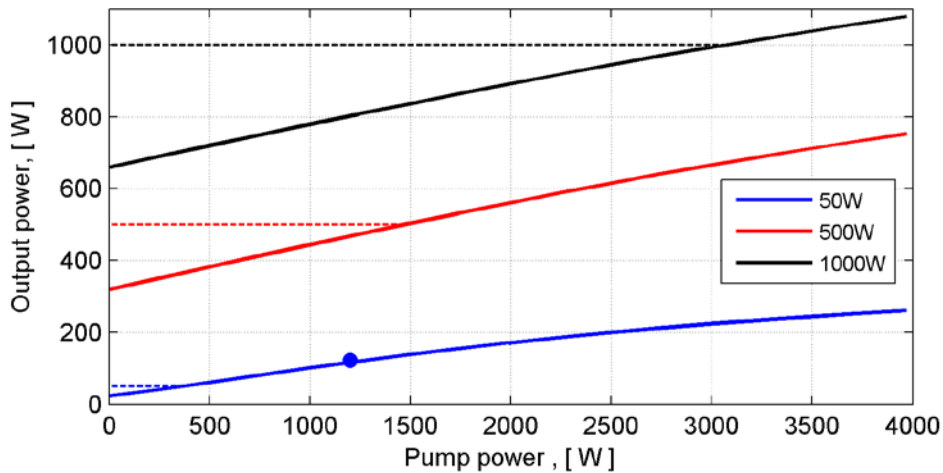


**Figure 4-19: Simulation of the output power for bigger seed-to-pump spot sizes ratio.**

Dashed horizontal lines show the seed power, i.e. switching point between the absorption and the amplification regimes. Blue spot at  $P_p = 1200W$  corresponds to 122W of measured output power with a 50W seed. Parameters:  $D_{PS} = 10mm$ ,  $D_{SS} = 3.3mm$ ,  $N_{bounces} = 19$ .

### 4.2.5 Results and conclusions

Imaging is the most simple and obvious solution for a multipass amplifier with a relatively big amount of bounces. It has an important alignment advantage: all the bounces can be precisely aligned and overlapped within the pump spot (using reference) in the unpumped state and keep this alignment during the operation. This property allows for a big seed-to-pump spot sizes ratio which should lead to a very efficient energy extraction at every single bounce.

However the imaging design multiplies the expected problems caused by high power pumping to the degree that makes the developed amplifier not usable. The soft aperture and thermal lens effects, which are applied to the seed beam on every bounce over the disk, add up and lead to a significant wavefront degradation, which in turn causes deviation from the planned beam propagation and a critical increase of the laser light intensity on some optics. Thus a reproducible damage of one of the imaging mirrors did not allow exceeding 300W of output power. It was reached at 1700W of pump power and 100W seed with the spot sizes of 8mm and 5mm respectively ( $G = 3$ ).

Notable improvement of the beam quality was demonstrated by decreasing  $R_{SP}$  to 33% ( $D_{PS} = 10mm$  and  $D_{SS} = 3.3mm$ ). However such a small seed beam extracts the energy from a very small part of the pumped area which leads to strong reduction of the gain. Simulations prove

## 4.3 Quasi-resonator configuration

that efficient amplification in this condition is not possible. Improving the gain – or at least keeping it at the same level for higher seed powers – requires significant increase of the pump power and thus is not possible due to thermal misalignment of the system. Moreover, higher pump power is expected to enhance the soft aperture and thermal lens effects, which can additionally worsen the beam quality even with a low  $R_{SP}$ .

All this results in a conclusion that the imaging scheme is not acceptable for the given purpose and another design is required.

## 4.3 Quasi-resonator configuration

### 4.3.1 Eigenmode preservation

The main requirement for efficient and stable amplification in a multipass amplifier is the reproducibility of the seed beam: every time the seed beam hits the disk for a new iteration it should have the same size and position within the pumped area. This main requirement for the beam size can be extended to the divergence, otherwise the beam will not reproduce the same propagation. Mathematically these requirements are defined as  $q_{i+1} = M \times q_i$  and the most obvious solution for any given beam is a uniform matrix  $M = \begin{pmatrix} 1 & 0 \\ 0 & 1 \end{pmatrix}$  that corresponds to the  $4f$ -imaging scheme, described in the previous section. However this requirement can be also fulfilled for  $M \neq 1$ . Any linear operator  $\bar{P}$  has a set of vectors, called eigenvectors, which are just stretched to a factor  $\lambda$  when are being modified by this operator:  $\bar{P}x = \lambda x$ . So if  $q_E$  is an eigenvector for a matrix  $M \neq 1$ , that has an eigenvalue  $\lambda_E = 1$ , it is also reproduced after each iteration (**Figure 4-20**).

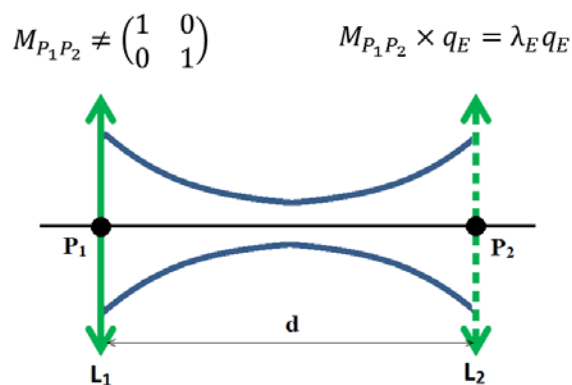


**Figure 4-20: Eigenvector preservation.**

Each iteration consists of just a single lens  $L_j$  and a propagation distance  $d$ . Second lens is shown with a dashed line indicating, that it belongs to the second iteration and corresponding transformation matrix is not included in the transformation matrix  $M_{P_1P_2}$  between points  $P_1$  and  $P_2$ . If the input beam is matched to the eigenvector  $q_E$  with a corresponding eigenvalue  $\lambda_E = 1$ , it is preserved after propagating through the cell.

In this case a multipass amplifier operates like a resonator, where the amount of roundtrips is defined by the amount of optical components rather than by the optical switch. The simplest resonator requires just two concave curved mirrors, whose function can be performed by the curved disks separated by a distance  $d$ . Then the full iteration matrix is

## Chapter 4: Multipass amplifier

$M = M_d M_D M_d M_D$  and for any given values  $d$  and  $D$  the eigenvector can be numerically calculated via solving the linear system  $Mq_E = q_E$ . **Figure 4-21** shows the diameter of the eigenmode depending on the distance between the disks.

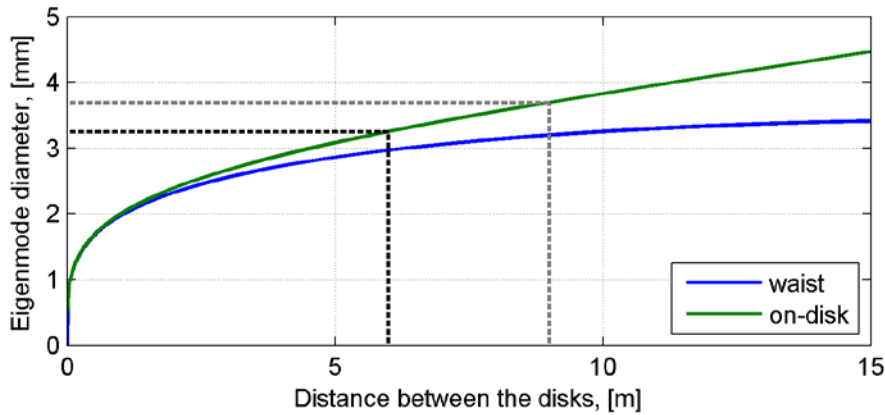


**Figure 4-21: Dependence of the eigenmode from the propagation distance.**

Blue curve shows the calculated waist diameter in case of  $RoC = 20m$  for both disks. The waist should be located at the distance  $d_{DD}/2$  in front of the first disk. Green curve shows the beam size on the disks  $D_{SS}$ . The first dashed line (black) points out the parameters in case of  $d_{DD} = 6m$  that corresponds to the optical scheme with the folding mirrors (**Figure 4-8**), the second dashed line (gray) – for  $d_{DD} = 9m$  without folding mirrors (**Figure 4-22**).

Just replacing the imaging mirrors with flat ones (**Figure 4-8**) leads to the disk-to-disk distance  $d_{DD} = 6m$  and the eigenmode diameter on the disk  $D_E = 3.25mm$ , what is expected to be too small for the planned output pulse energy and can lead to high damage probability. According to **Figure 4-21** eigenmode grows quite slowly and requires a big increase of the distance between the disks for any significant change. However this distance can be easily enlarged for 50% without fundamental changes in the existing amplifier setup – by exclusion of the folding mirrors. In this case the distance between the disks  $d_{DD}$  is roughly 9m, which leads to  $D_E = 3.7mm$  meaning  $\sim 30\%$  bigger area and lower damage probability. Corresponding system layout is presented in figure **Figure 4-22**.

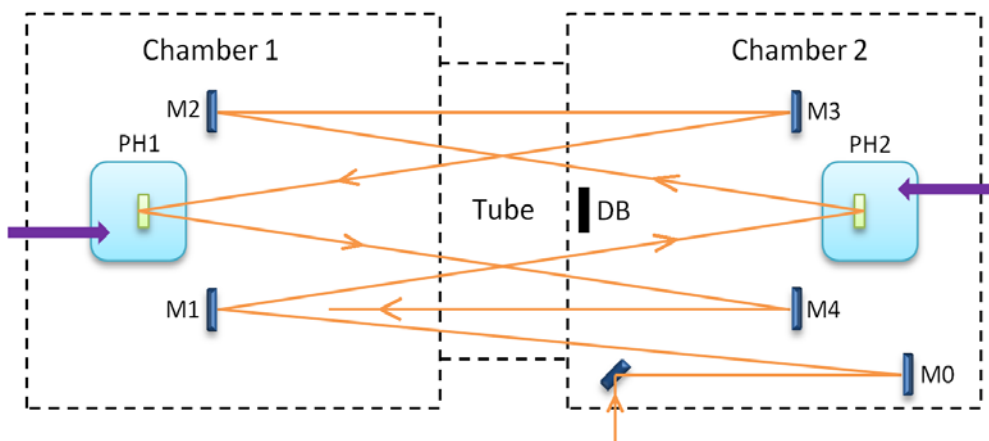


**Figure 4-22: Quasi-resonator scheme.**

In contrary to **Figure 4-8** all mirrors M0–M4 are flat. DB is the disk blocker.

### 4.3 Quasi-resonator configuration

Such optics allocation requires a special *disk blocker* – a small, non-transparent round screen that blocks the straight path between two disks, preventing them from forming an extra resonator. and lasing towards each other. If it happens, the generated beam is bouncing between the disks and is being amplified without any out-coupling, which inevitably leads to damages. In the imaging configuration it was not needed because the optical path between the disks were blocked by the cameras, which were installed behind the folding mirrors for alignment of the pump and seed spots.

**Figure 4-23** shows the evolution of the eigenmode in the system. The obvious difference of this setup comparing to the imaging configuration is the avoidance of the focusing between the disks. Beam size between the disks decreases but only down to the input waist diameter  $D_{waist} = 3.3\text{mm}$ , which solves the problem of air ionization and eliminates the need to run the system in vacuum. This in turn removes additional alignment distortions caused by evacuation of the air from the chambers.

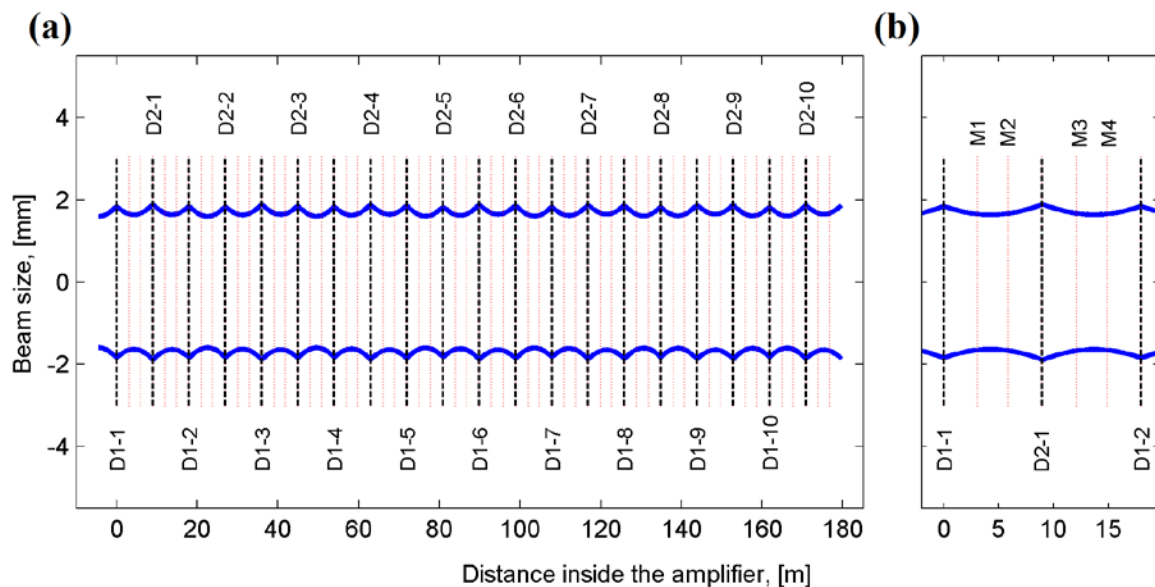


**Figure 4-23: Evolution of the eigenmode inside the amplifier.**

If the waist and position of the input beam are matched to the eigenmode, it reproduces the same propagation at each iteration. (a) Full propagation through the system. (b) Magnified image of the 1<sup>st</sup> iteration. M1–4 – plane steering mirrors of the first iteration. Second iteration starts at D1–2 – second bounce over the first disk.

However the total propagation distance inside the amplifier increases almost twice and the seed position on the disk is not defined by the imaging properties anymore. This makes the system quite sensitive to possible any misalignment of the seed beam, what will be discussed later in section 4.3.4

#### 4.3.2 Deviation from the eigenmode

One important advantage of using this quasi-resonator scheme is its high robustness to the wavefront change caused by thermal load. According to **Figure 4-12** in case of imaging configuration a 30% change of the effective disk curvature leads to such strong deviation from the ideal propagation that at the last iterations beam focusing happens close to the mirrors

## Chapter 4: Multipass amplifier

instead of being exactly in the middle of the imaging cell. On some other mirrors the beam becomes two times bigger, which together with thermal misalignment causes the clipping and thus limits the maximal possible pump power. **Figure 4-24** shows the result of such a 30% change of the effective disks curvature to the eigenmode evolution.

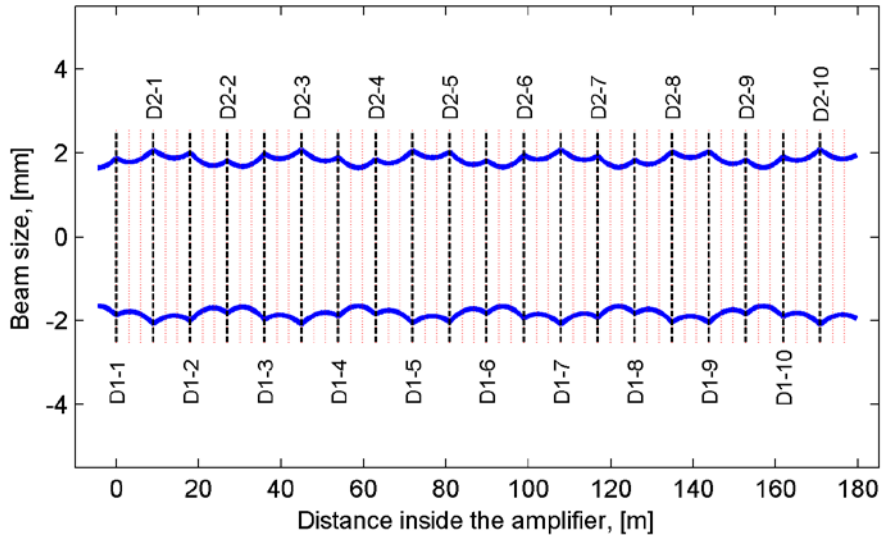


**Figure 4-24: Eigenmode robustness.**

Here the input beam corresponds to the eigenmode of the unpumped state (**Figure 4-23**), while the effective radius of curvature of the disks is 30% bigger.

Maximal beam size deviation from the eigenmode does not exceed  $\pm 14\%$  on the disks and  $\pm 12\%$  on the steering mirrors, which is quite robust in comparison with the imaging configuration. Such a change in the system can be considered as a mismatch of the input beam to the new eigenmode  $q_{E_{pumped}}$  corresponding to a different effective radius of curvature of the disks. In analogy to **Figure 4-21**, the dependence of the eigenmode size on the disks curvature can be calculated.

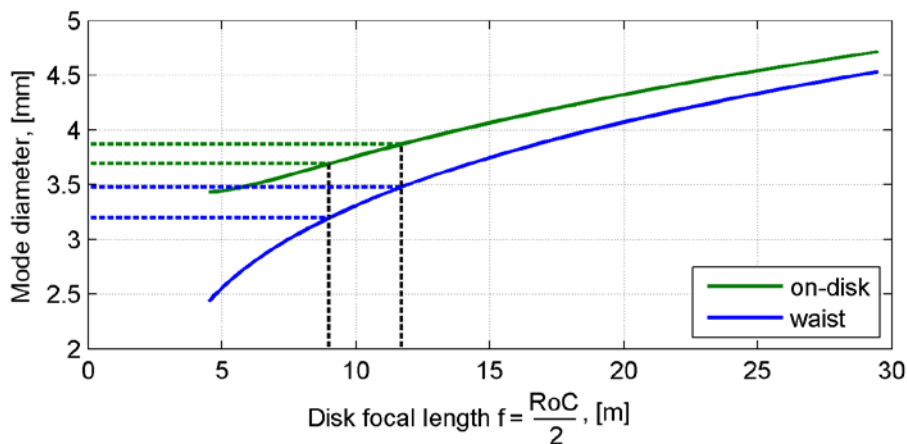


**Figure 4-25: Dependence of the eigenmode from the disks radius of curvature.**

Distance between the disks ( $d_{DD}$ ) is fixed and equal to 9m. Blue line corresponds to the mode diameter on the first disk, red line – its waist diameter, which for correct propagation should be located at  $d_{DD}/2 = 4.5m$  in front of the first disk. Vertical dashed lines indicate the normal (unpumped condition) and the 30% bigger disk curvatures. Their intersection with the blue and red curves is marked with dashed lines of the corresponding color.

### 4.3 Quasi-resonator configuration

Thermally induced change of the eigenmode, demonstrated by the dashed lines in **Figure 4-25**, can also be interpreted differently. For a given mismatch between the input beam and the eigenmode, beam size on the disk (blue curve) differs by only 5%, while its waist size (red curve) differs by almost 10%. It means that during a real mode-matching the input beam has to be controlled by its waist size rather than its size on the disks due to higher sensitivity. Position of the waist does not depend on the disk curvature and is defined only by the disk-to-disk distance.

Though the propagation of the mismatched input beam (**Figure 4-24**) looks complicated, comparison of the beam size on the disks or steering mirrors shows pure sine oscillations around some average value. **Figure 4-26** shows the beam size on the disk and on the output steering mirror at each iteration. Relative phase shift between two sequential points is constant and depends on the deviation from the eigenmode. For both sets of points a sine fit is performed. Dashed lines show the size that would correspond to the correct mode propagation.

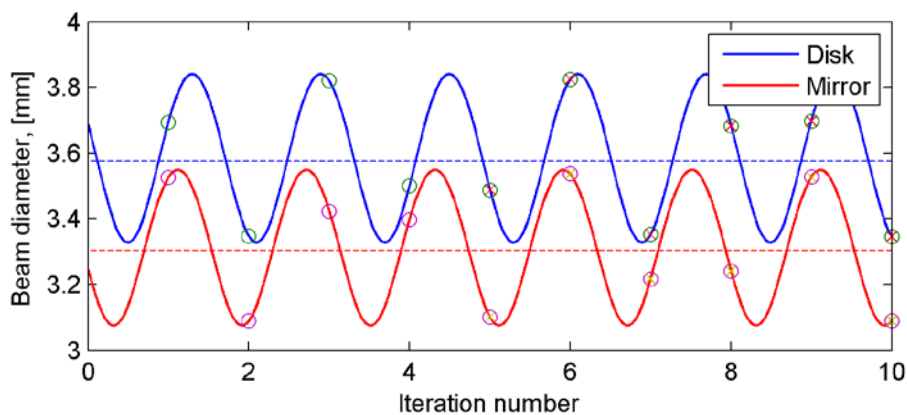


**Figure 4-26: Oscillation of the beam size.**

Sine fit of the beam size on Disk1 (blue) and the input steering mirror (red). Empty circles correspond to the calculated values from **Figure 4-24**. Crosses correspond to the prediction of the beam size based on the first four iterations. Predicted values perfectly match the calculated values

This phenomenon plays an important role in the real mode matching procedure in the laboratory setup. Since a full sine curve can be defined based on just 4 points – according to the equation  $\omega = \omega_0 \sin(fT + \varphi_0)$  – and the relative phase shift between two consecutive points is constant, measuring just 4 beam profiles from any 4 iterations allows to predict the beam size on all the mirrors and thus to estimate how big the mismatch between the given input and the real eigenmode of the system actually is.

#### 4.3.3 Mode matching

In case of  $4f$ -imaging the position of the input beam waist does not play any important role. As it is mentioned in section **4.2.1**, it is preferable to use a collimated or close to collimated input beam, but only because it should fit the mirrors size along the whole propagation.

Matching the input beam to an unknown eigenmode that does not exactly correspond to the value obtained from simulations is much more complicated. It is an iterative process that starts (*Step 1*) with preparing the input beam based on the calculated value. This beam should have

## Chapter 4: Multipass amplifier

the waist corresponding to the calculated one and located exactly  $d_{DD}/2$  in front of the first disk, where  $d_{DD}$  is the distance between the disks. This adjustment is performed by using an input scaling telescope that should scale the seed beam obtained from a source laser. It consists of consecutive concave and convex curved mirrors with the same radius of curvature. In principle the focusing mirror should have a longer focal length to perform the scaling, but due to the significant seed beam divergence caused by a long beam path on the optical table, correct adjustment requires both mirrors to have the same absolute optical power just with the different sign. **Figure 4-27** demonstrates the scheme of the input scaling telescope.

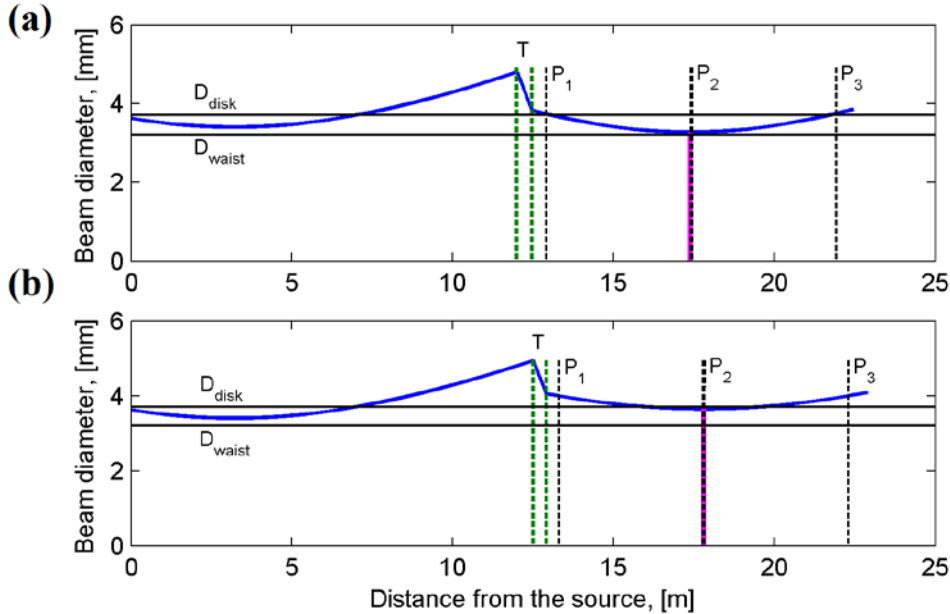


**Figure 4-27: Input scaling telescope.**

Telescope lenses (green dashed lines, mark  $T$ ) collimate the divergent beam coming from the source laser. Three dashed black lines show three planes  $P_1$ ,  $P_2$  and  $P_3$  where the beam size is measured (right after the telescope, +4.5m and +9m).  $P_3$  also corresponds to the position of the first disk. Horizontal black lines are the eigenmode references: a correct input beam should have the size  $D_{waist}$  at  $P_2$  and  $D_{disk}$  at  $P_1$  and  $P_3$ . Purple line shows the beam waist after the telescope. The waist size and the beam divergence are controlled by the propagation in front of the telescope and the lens-to-lens distance. Subfigure (a) shows the correct mode matching. Subfigure (b) shows a wrong input beam. Longer (+0.5m) propagation before the telescope and shorter telescope length (-6cm) leads to a bigger waist located at the same position.

The waist position and size after the telescope have a complicated dependence on the input beam and position of the lenses. For example, fine tuning of the output waist size can be performed by increasing the propagation of the beam in front of the first lens, what leads to increase of the input beam size. But such a change also affects the divergence of the output beam and thus requires an extra adjustment of the lens-to-lens distance. The entanglement of the telescope beam transformation can be easily demonstrated by comparison of the changes in the output beam, caused by a small individual deviation of the two input parameters (analogy to the partial derivatives). If  $L_0$  and  $T_0$  are the distance to the source and the lens-to-lens distance in the optimal condition, i.e. corresponding output beam has the necessary waist  $\omega_0$  and the waist position  $W_0$ , the relative change of the output beam parameters can be described by **Table 4-1**.

### 4.3 Quasi-resonator configuration

**Table 4-1: Influence of the input telescope**

Input parameters change		Resulting output beam change	
$\Delta T/T_0$	$\Delta L/L_0$	$\Delta\omega/\omega_0$	$\Delta W/W_0$
+10%	0	-8%	0
-10%	0	+8%	-8%
0	+10%	+2%	+23%
0	-10%	-3%	-21%

*Step 2* of the mode matching procedure is checking the beam size oscillations inside the system based on four measurements. For this purpose the beam size at the input or output steering mirrors is measured for four consecutive iterations. A sine fit is applied to the obtained data, allowing to predict the beam size on the rest of the mirrors, which are not always reachable for measurements because of the convoluted beam propagation scheme around the steering optics. These measurements are performed while sending to the system a very weak seed beam and pumping the disks with 50–60% of the pump power that is normally used for amplification. Sending the full pump power without extracting the energy by a high power seed can lead to a damage, but due to the high robustness of the system to the effective disks curvature the change of the eigenmode in a fully pumped condition can be well approximated by this method.

If the error of the waist size or position is too big (the minimal and maximal measured beam sizes differ more than two times), it is possible to predict the necessary correction by comparison of the obtained sine fit with the simulated propagation of the wrong input beam – too big/small waist and too far/close waist position. Then *Step 1* and *Step 2* are repeated again and a new measurement of the beam profiles is performed. When the error of both parameters is comparable and is below 20%, it becomes almost impossible to predict the necessary correction. Further optimization can be performed only by a systematic comparison of several telescope configurations, for example 3 different telescope lengths  $T$  (with a step of 3–4cm) for 3 different distances to the source  $L$  (with a step of 0.5m). Theoretically an almost perfect mode matching can be performed by careful systematic comparison of the beam propagation for many – for example 10 by 10, instead of 3 by 3 – different configurations, i.e. using smaller steps. But in reality a single measurement requires about 30–45 minutes, because the only possible way to measure the beam profile without misaligning the system is to insert a small wedge in the beam path at the desired iteration and to match the distance between the wedge and corresponding mirror. The results of several different input beams can be compared in order to choose the best one.

**Figure 4-28** demonstrates several fits, performed during optimization of the mode matching. Subfigures (c) corresponds to the best of them – the corresponding input beam was used for

## Chapter 4: Multipass amplifier

amplification. There the beam size still oscillates (with ~10% amplitude) around the value  $D = 3.64\text{mm}$  but such a small deviation is acceptable and can be hardly improved without big systematic scan as it was described before. Moreover, at full pump power the effective curvature of the disks and the corresponding eigenmode will be slightly different, what makes too high precision during such a mode-matching useless for further operation.

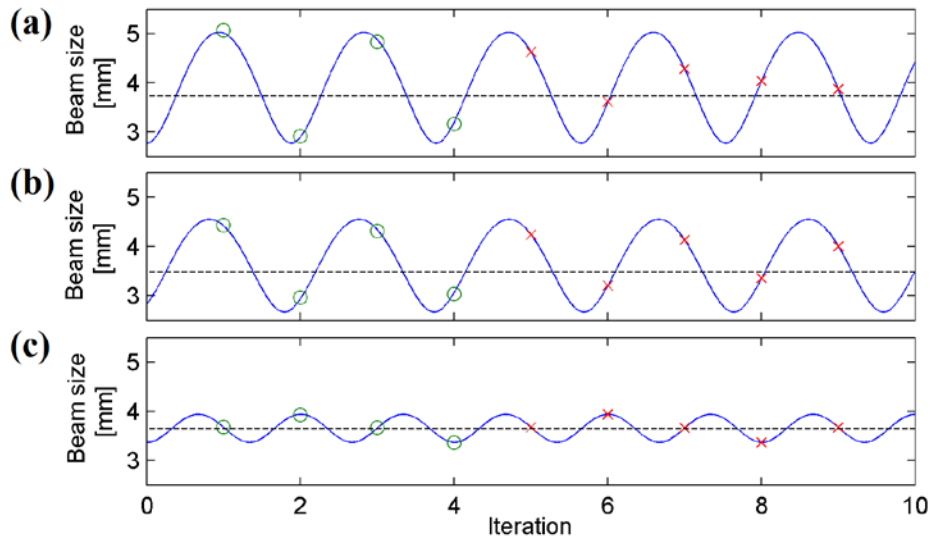


**Figure 4-28: Sine fit in case of different input beams.**

Here the beam size measurements and the consecutive sine-fits were performed for three different input beams (i.e. configurations of the input telescope). Round markers correspond to the measured beam sizes at the first 4 iterations, crosses – to the fit-based prediction. Main criteria of the comparison are the smallest oscillation amplitude and the biggest minimal size. According to them the input beam leading to (c) is chosen as the best one.

### 4.3.4 Stability and alignment

Besides the complicated mode matching, overlapping of the seed bounces at different iterations is also not trivial in the non-imaging configuration. First of all the alignment itself is less precise: without imaging the shadow-based alignment method is not available and overlapping is only controlled by observing the brightness-symmetry of the resulting spot. For human eyes it is much more complicated than distinguishing positions of the sharp edges of the shadow. Additionally to this any deviations of the input beam or a slight tilt (for example thermally caused) of involved optics disturbs the initial overlapping. In the  $4f$ -imaging case all such distortions led to displacement of the beam on the imaging mirrors while the bounces on the disks stayed perfectly overlapped.

There are two different types of the seed beam misalignment that can take place in a quasi-resonator amplifier. The first type is related to the input beam deviation. In perfect case the input beam hits the center of the input steering mirror (M1 in **Figure 4-22**) that sends it to the center of the pump spot on the disk. If the disk and the mirror wheel are correctly aligned, the beam is reflected to the center of the output steering mirror (M2) that sends it to the second disk and mirror wheel, where the beam hits all the optics exactly in the center again. It happens at each iteration and leads to a good spatial overlap. But if the input beam deviates from the correct direction and hits the first disk not in the center all the propagation changes. **Figure 4-29** demonstrates such a change in the seed beam overlapping.

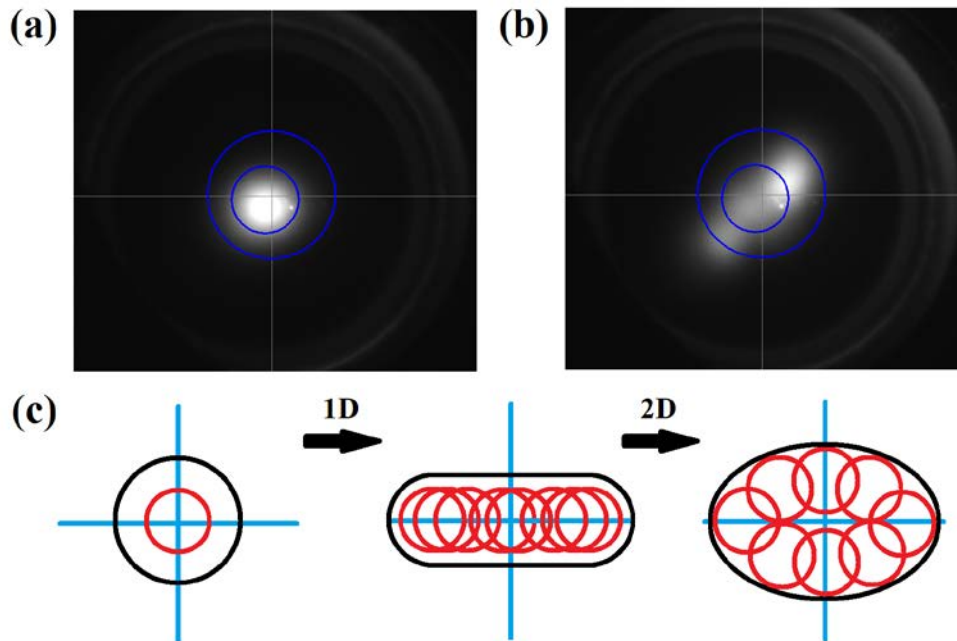


**Figure 4-29: On-disk seed pattern in case of the input beam misalignment.**

(a) Well overlapped seed bounces form a single bright seed spot. (b) Misalignment of the seed beam in one direction leads to a spreading of the seed bounces along a line. Blue circles – the alignment references. Gray cross shows the center of the disk, which coincides with the pump spot center. (c) Scheme of transformation of a well aligned seed spot into a line and ellipse, whose axes size is proportional to the degree of the input beam misalignment in the corresponding direction. Red circles indicate the individual bounces, black line – the shape of the final pattern. In the aligned condition intensities of all the bounces add up forming a circle with a bigger radius. In both misaligned cases (1D and 2D) the new seed patterns stay centered at the original position (blue cross).

If the input beam is tilted relatively to the main optical axis of the system, the seed beam does not completely deviate from its path and does not stop hitting the mirrors, as it could be expected in case of almost 200 meters of propagation. A well overlapped seed spot turns into a line filled with bounces from different iterations and located symmetrically relatively to the center of the original seed spot position. The change of the beam position on the steering mirrors has a similar scale, so it does not get clipped and reaches the output having completely the same size and divergence. This effect can be generalized based on the propagation of the beam in real (closed) resonators, where off-axis propagation of the mode leads to an elliptic [19, p14–16] pattern of individual bounces, as it is shown in **Figure 4-29c**. Thus a line pattern on subfigure (b) is just an ellipse with one axis degraded to almost zero length. Such a deviation from the correct propagation can also occur somewhere in the middle of the system, when for example a single steering mirror is misaligned. Then some first bounces stay overlapped, but the rest are shifted to the positions allocated on the corresponding ellipse.

Another type of misalignment is connected to the disks. High thermal load causes the beam translation which can be described as an effective tilt of the disks central axis. Such a tilt changes the main optical axis of the system in a way, that the originally correct input beam obtains an offset relatively to the new optical axis and forms an ellipse again. But in this case the center of the ellipse also shifts relatively to the center of the original seed spot. **Figure 4-30** shows the intentional reproduction of this effect by applying a small tilt to one of the disks: it

## Chapter 4: Multipass amplifier

slightly stretches the seed spot into an ellipse (its axes are very small), but significantly shifts its position relative to the original one and thus relative to the pump spot.

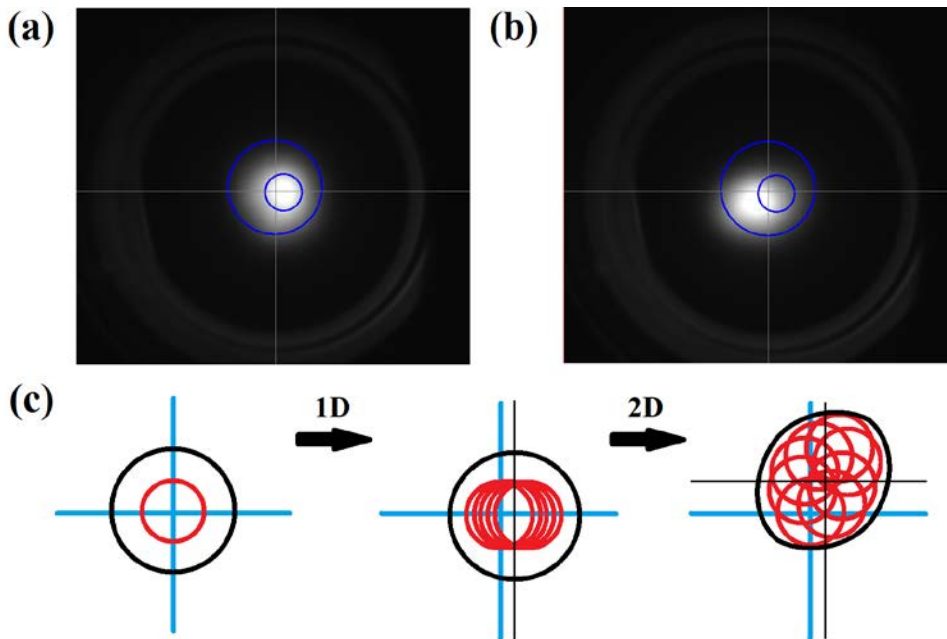


**Figure 4-30: On-disk seed pattern in case of the disk misalignment.**

(a) Normal aligned state. (b) Misalignment caused by the disk tilt. (c) Scheme of the demonstrated misalignment. Red circles indicate the individual bounces, black line – the shape of the final pattern. In contrary to **Figure 4-29**, such a misalignment shifts the center of the final pattern (black cross). Realignment of the system with only steering mirrors, i.e. without compensation of the disk tilt, would collect all the bounces into a single point again, but it would be located at this new position.

Combination of both mentioned effects can cause a significant displacement of the seed beam relative to the pump spot. If some seed bounces are just located too close to the edge of the pump spot, the beam profile can slightly degrade due to inhomogeneous amplification, while a bigger displacement can even cause a significant drop of the output energy due to absorption in the unpumped region of the disk. This can be controlled by observing the depletion pattern within the pump spot.

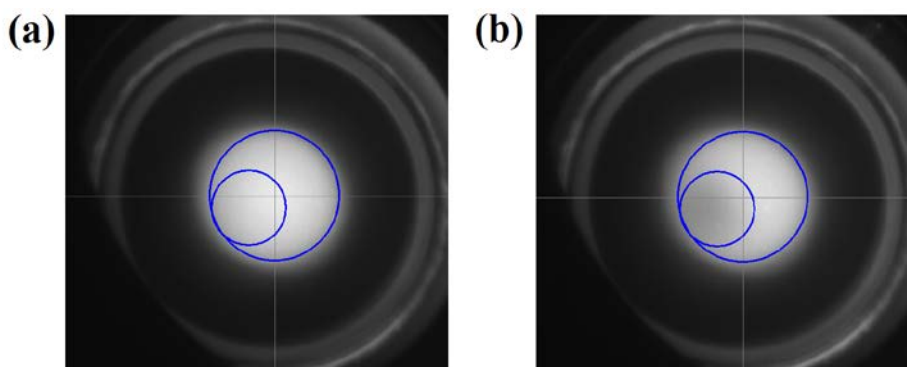


**Figure 4-31: Depletion observation.**

(a) Symmetric luminescence of a 10mm pump spot.  $P_S = 1W$ . (b) The same pump power,  $P_S = 100W$ . Darker area within the small blue circle corresponds to the depleted part of the pumped area. Seed spot is located close to the left-bottom edge of the pump spot by purpose for pre-compensation of thermal misalignment. Details are discussed later in paragraph 4.3.6. Parameters:  $D_{PS} = 10mm$ ,  $D_{SS} = 4.4 \pm 0.7mm$ ,  $P_P = 500W$ .

### 4.3 Quasi-resonator configuration

**Figure 4-31** demonstrates the camera image of the pump spot without any depletion **(a)** and with significant energy extraction **(b)** by a 100W seed. Energy extraction in corresponding region reduces the population of the upper energy level, which in turn reduces the probability of spontaneous emission. Luminescence observed with the camera is proportional to the amount of spontaneously emitted photons and thus is lower in the depleted region. Unfortunately depletion can be recognized in the image only in case of significant energy extraction, what happens when the pump power is low while the seed is strong and all the seed bounces stay well overlapped (depleting the same area).

For example, the output power in **Figure 4-31b** is 250W what corresponds to  $\sim 75W$  energy extraction from a single disc pumped with 500W. In high power operation regime (which will be discussed later) the ratio between the extracted and pumping powers stays roughly the same, but high thermal load on the disks leads to an elliptic seed pattern. Thus the energy extraction is distributed over a bigger area and is not so pronounced. In this regime only the stability of the output power and the output beam shape can serve as indirect indication of correct positioning of the seed within the pump spot.

#### 4.3.5 Beam quality

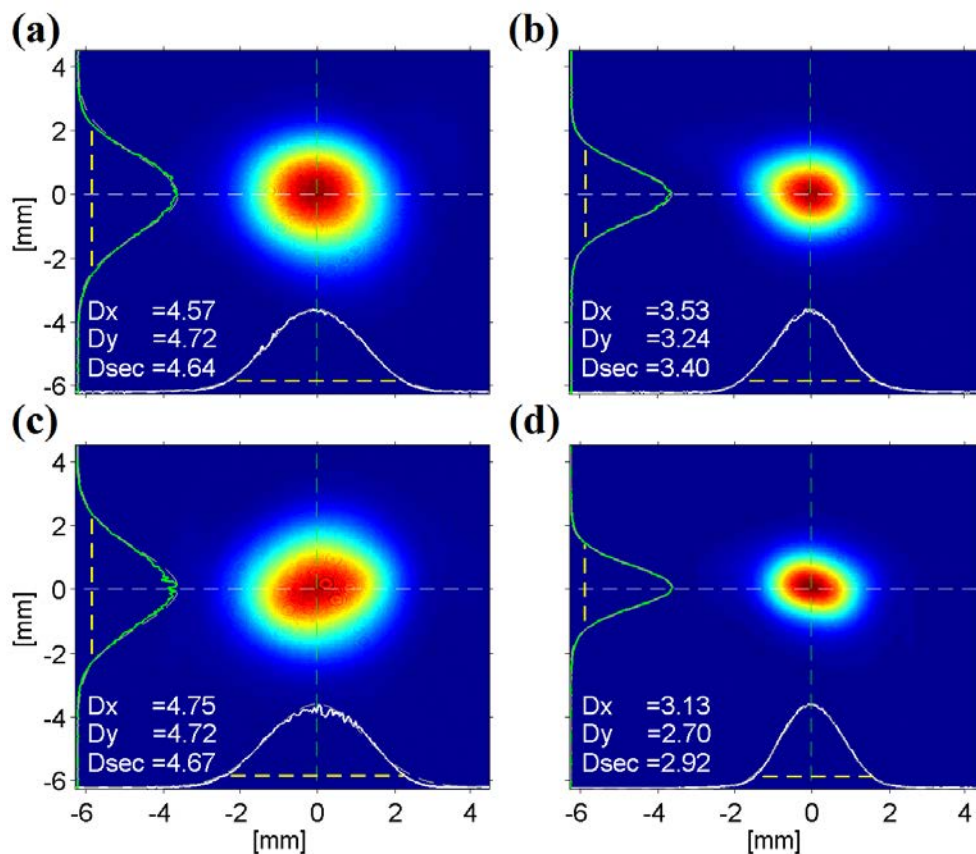


**Figure 4-32: Beam quality without pumping.**

Beam profile on the disks from **(b)** 1<sup>st</sup>, **(c)** 6<sup>th</sup> and **(c)** 9<sup>th</sup> iterations. **(d)** Beam profile on the input steering mirror from the 10<sup>th</sup> iteration. Parameters:  $D_{PS} = 10mm$ ,  $D_{SS} = 4.4 \pm 0.7mm$ ,  $P_p = 0$ ,  $P_s = 1W$ .

## Chapter 4: Multipass amplifier

Regardless of the disadvantages that the non-imaging design has – lower alignment precision and no preservation of seed bounces overlapping – it solves the main problem that limited the output power of  $4f$ -imaging configuration, namely significant degradation of the beam profile leading to the optics damage. The weakest point in that case was the input imaging mirrors (M1 in **Figure 4-8**) of the last 10<sup>th</sup> iteration, where due to pumping initially normal Gaussian beam was transformed into the Airy pattern (**Figure 4-17**) with a peak intensity exceeding the designed value.

Even the propagation through the non-pumped system led to significant distortions of the input beam (**Figure 4-15b**). In contrary to this quasi-resonator scheme demonstrates almost no change in the beam quality caused by propagation. **Figure 4-32** shows the beam profiles on the disks at different iterations and on the input steering mirrors (M1 in **Figure 4-22**) of the last iteration. Besides the beam size change, caused by not perfect mode matching, no difference is observed. If the seed beam stays within the pump spot at each iteration (i.e. it is always amplified proportionally to Gaussian intensity distribution), increase of the pump power also does not affect the beam quality. **Figure 4-33** (subfigures **a** and **b**) demonstrates corresponding change of the output beam profile.

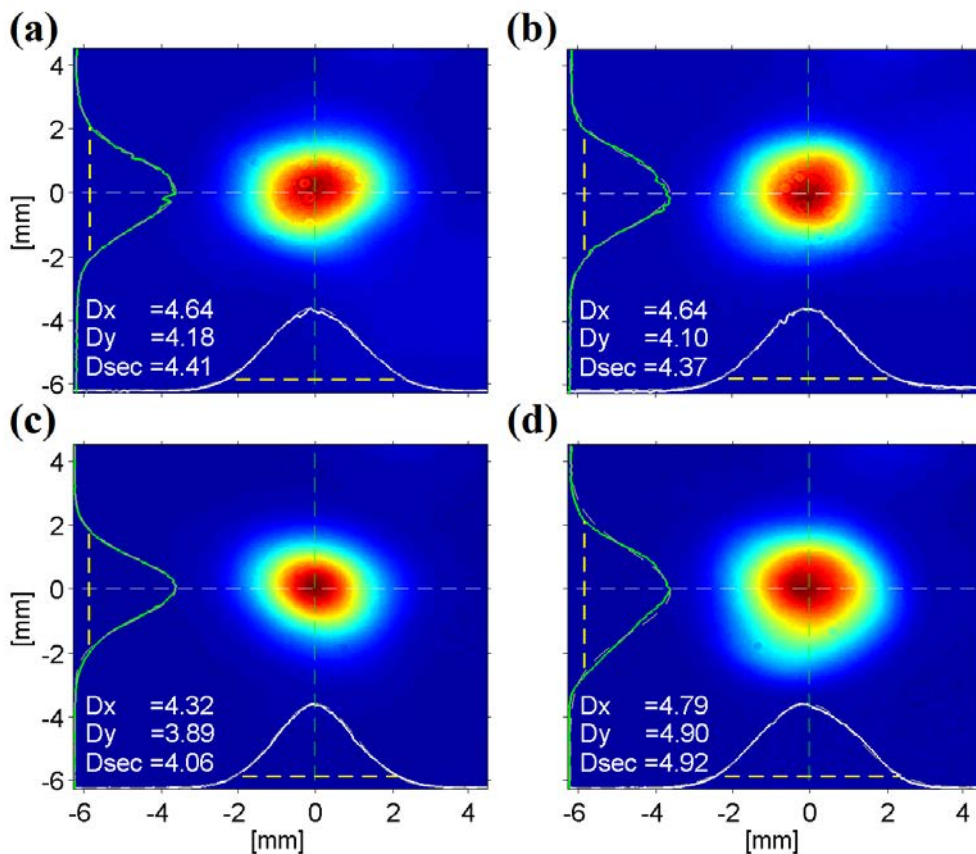


**Figure 4-33: Influence of the pump power on the output beam profile.**

(a) Normal alignment of the seed,  $P_p = 500W$ . (b) Increase of the pump power to  $P_p = 1300W$  does not affect the beam quality (c) Seed spot is aligned close to the edge of the pump spot,  $P_p = 500W$ . Seed pattern stays within the pump spot. (d) Further increase of the pump power to  $P_p = 800$  leads to increase of the seed pattern size. It crosses the pump spot edge, beam profile degrades. Parameters:  $D_{pS} = 8mm$ ,  $D_{SS} = 4.4 \pm 0.7mm$ .

### 4.3 Quasi-resonator configuration

Though the seed-to-pump spot sizes ratio is close to 50% ( $D_{PS} = 8\text{mm}$ ,  $D_{SS} = 4.4 \pm 0.7\text{mm}$ ), the output beam stays close to Gaussian even for the pump power of 1300W. Such an improvement is the result of two factors: avoiding the multiplication of the surface imperfectness caused by imaging (discussed in paragraph 4.2.4) and a resonator-like mode cleaning. The amount of roundtrips is of course much smaller than in normal resonators, but it follows the same principle. The eigenmode (in real setup an input beam that is close to the eigenmode) is efficiently amplified at each roundtrip because of the optimal seed beam size and position within the pump spot, while distorted part of the beam propagates incorrectly and thus has much worse amplification.

However further increase of the pump power above 1400W leads to significant instability of the output beam. In the imaging configuration high thermal load causes a translation of the beam on the imaging optics, while the seed bounces stay perfectly overlapped. Maximal pump power was limited by reaching the edge of the output imaging mirror at the last iterations. In a resonator-like system thermal load changes the eigenmode (paragraph 4.3.4) what causes a displacement of the seed beam on the disks and mirrors. A round seed spot turns into an ellipse and shifts towards the edge of the pumped area. Thus some bounces are not amplified smoothly (spatially) and the beam profile degrades. Subfigures (c) and (d) of **Figure 4-33** give an example of such a change caused by a manual alignment of the seed spot close to the edge of the pump spot. In this case even at low pump power a significant change in the beam profile can be observed. Moreover, crossing the pump spot edge “resonates” with small instabilities of the seed beam, transmitted from the input or generated by the air heating inside the system. Seed spot shakes around the sharp edge of the pumped area, continuously changing the profile and thus the propagation of the beam, which in turn amplifies on-the-disk position instability. Critical shift of the seed bounces pattern cannot be precisely recognized by the disks depletion observation, but it immediately leads to a strong shaking of the output beam accompanied by fast and unpredictable changes of its shape.

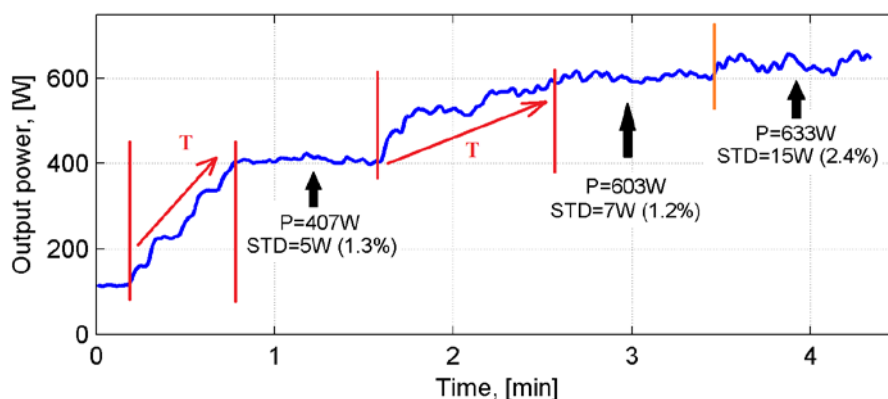


**Figure 4-34: Stability drop in case of reaching the edge of the pump spot.**

Seed beam position is not optimized inside the pump spot. Stepwise increase (transition regions a marked with red letters *T* and arrows) of the seed power up to  $P_S = 200\text{W}$  and the pump power up to  $P_P = 1100\text{W}$  allows reaching the output power of 603W with the standard deviation  $STD = 1.2\%$ . Further increase of the pump power to  $P_P = 1200\text{W}$  increases the standard deviation twice. Parameters:  $D_{PS} = 10\text{mm}$ ,  $D_{SS} = 4.4 \pm 0.7\text{mm}$ .

## Chapter 4: Multipass amplifier

Reaching the edge of the pump spot can be also seen in the output power trace. **Figure 4-34** demonstrates an example, recorded during the investigation of the seed beam misalignment. It is important to note, that such a value ( $STD = 2.4\%$ ) alone does not necessarily indicate the discussed effect. The key indicators are a significant stability degradation observed simultaneously with the output beam shaking and shape changing, which appear as immediate reaction for a relatively small ( $\sim 100\text{W}$ ) increase of the pump power.

### 4.3.6 Amplification

Good output beam quality simultaneously with a high seed-to-pump spot sizes ratio allows for a high total gain. **Figure 4-35** shows the amplification of a  $50\text{W}$  seed beam. At the pump power of  $1300\text{W}$  the output power is  $500\text{W}$ , what corresponds to the gain factor  $G = 10$ .

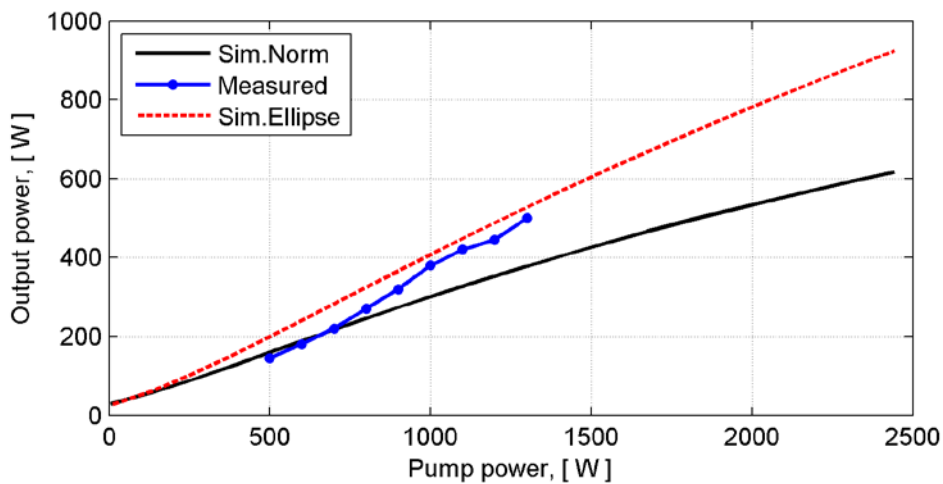


**Figure 4-35: High-gain amplification.**

Blue curve represent the measured output power as a function of pump power. Specified value is applied to both disks. Black line shows the simulations result. Increasing disagreement is referred to increase of the seed ellipse pattern. Red dashed line corresponds to the modified simulations (see **Appendix A.2**), which shows a better agreement for the pump power above  $1000\text{W}$ . Parameters:  $D_{PS} = 8\text{mm}$ ,  $D_{SS} = 4.4 \pm 0.7\text{mm}$ ,  $P_S = 50\text{W}$ .

Notably, the presented curve is very close to the simulations in the beginning, but significantly exceeds it for a higher pump power. Such a behaviour can be assigned to increase of the energy extraction area caused by the ellipse growth. The higher is the pump power, the bigger is the ellipse formed by the seed bounces. Though the bounces from different iterations stay partially overlapped (as it is shown in **Figure 4-30**), each of them has a small pumped region that is used exclusively by this bounce. The bigger is the ellipse, the bigger is this individual part and thus the gain at each iteration. It could be expected that partial overlapping of the bounces may lead to inhomogenous amplification, but according to the measured output (and also in-system) beam profiles this effect is negligible. It is either smoothed out by the seed pattern symmetry or is not strong enough because of relatively low single-pass energy extraction: in normal operation the intensity flux ratio between the seed and the pump beams doesn't allow for significant depletion after a single bounce (two passes through the crystal thickness), so spatial modulation of the gain are not strong enough to cause any significant degradation. Extra gain caused by the ellipse expansion can be included in simulations by using a special approach described in **Appendix A.2**.

### 4.3 Quasi-resonator configuration

Further increase of the seed power to 200W and the pump power to 1400W per disk led to 950W of the peak output power, but observed oscillations of the beam position and shape indicated reaching the edge of the pump spot. This thermal drift of the seed appeared to be reproducible for a given system alignment. The ellipse size and the translation direction of its center depend on the pump power: it returns back to the original alignment position when the pump power is switched off, but experiences the same shift as soon as the pump is on again. Observed misalignment consists of a fast reaction of the disk that disappears immediately after switching off the pump power (it was also observed in 4f-imaging configuration) and some slower component, which is probably connected to heating of some mechanics – it keeps the seed bounces slightly misaligned for 10–15 minutes after removing the power, afterwards they converge to a single spot again. The absence of this effect in 4f-imaging case was probably connected to a much lower power of the seed beam inside the amplifier.

Nevertheless this thermal drift of the seed can be partially counteracted by its *pre-compensation*. Such a pre-compensated alignment is the reason of non-centered position of the seed beam in **Figure 4-31**. Pump power there is 500W, which does not cause a big shift yet. All the seed bounces are well overlapped close to the bottom-left edge of the pump spot. When the pump is increased to 1500W, the ellipse moves up and right and such a pre-compensation provides few extra millimeters before reaching the edge of the pump spot. However the absolute amplitude of the translation and the ellipse size are dependent on the starting alignment position, which means that the same 1500W of pump power lead to a different translation for this exact pre-compensated position and any other, including the alignment to the pump spot center without any pre-compensation. Moreover, it counteracts only the shift of the ellipse center, but its size still grows. Thus such a pre-compensated alignment of the system allows for extra 300–500W of pump power, but does not solve the problem completely. The only possible way to keep the seed spot within the pumped area (without using motorized mechanics to adjust the disks central axes during the operation) is to increase the pump spot size. However this will reduce the intensity and total gain and increase the ASE losses, what means that for reaching the same output power a higher pump power will be needed. But higher pump power increases thermal load and can lead to an opposite effect.

Besides thermal misalignment of the seed position another unwanted effect was observed: clipping of the beam by the mechanical structure of the disks blocker. One possible solution of this problem would be changing the design of the vacuum chambers or developing some special blocker, installed on a platform that could slide inside the connecting tube, where the distance between the beams is bigger. Another way to avoid clipping is to remove some bounces over the disks. This solution was chosen for saving time and testing the system usability.

Of course, reduction of the passes through the gain medium reduces the gain. In order to estimate corresponding losses of the output power a set of measurements with different amount of bounces was performed. Corresponding measurements are presented in **Figure 4-36**. There a 10mm pump spot was used, because  $D_{PS} = 8mm$  appeared to be too small for stable amplification at high pump power.

## Chapter 4: Multipass amplifier

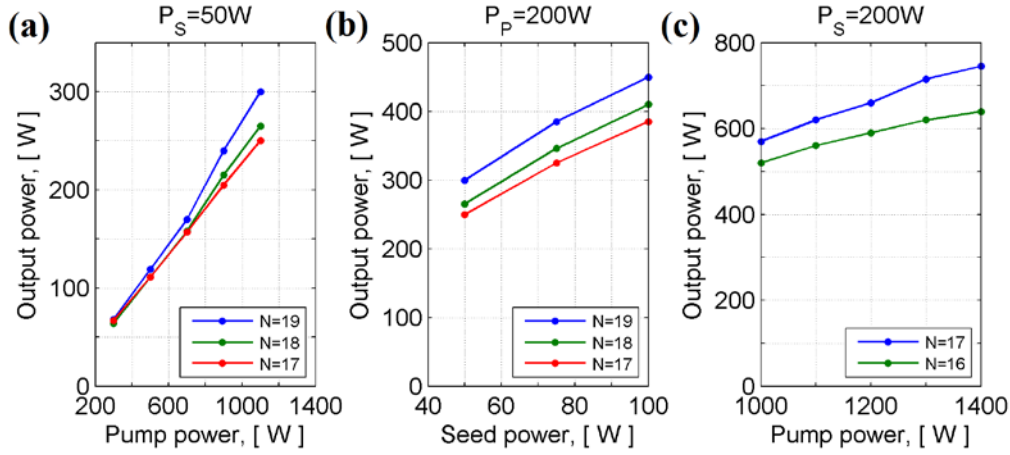


**Figure 4-36: Amplification with reduced amount of bounces.**

(a) Fixed seed power  $P_s = 50W$ . (b) Fixed pump power  $P_p = 1100W$ . (c) Fixed seed power  $P_s = 200W$ . Parameters:  $D_{P_s} = 10mm$ ,  $D_{S_s} = 4.4 \pm 0.7mm$ .

As subfigure (a) shows, relative difference in the output power increases with the pump power, but stays constant during increase of the seed with a fixed pump power. Estimated losses caused by reduction of the amount of passes are approximately 10% and 8% for 19<sup>th</sup> and 18<sup>th</sup> bounces, which means ~20% reduce of the total output power. Due to specific geometry of the laboratory space both last bounces have been removed for convenient access to the output beam. The last subfigure (c) corresponds to the high power seed (200W) amplification and is aimed to check, if the pump power is high enough and the disks are not absorbing the seed during the last iterations due to complete depletion of the upper energy level (UEL). According to this measurement, the last 17<sup>th</sup> bounce gives extra 14% of the output power indicating that UEL is far from being completely depleted and that the disks still contain a lot of energy, which can be utilized in the future upgrades of the system. Theoretically every additional bounce should provide less amplification because of the energy extraction and decreasing the ratio between the population of the upper and lower energy levels  $N_2$  and  $N_1$ , which according to equation 3.33 reduces the gain. But in a real setup the seed beam size is slightly different at each iteration (because of non-perfect mode matching) and the bounces are not perfectly overlapped, which leads to a different gain at each iteration. Another important result of these measurements is the expected drop of the gain due to the pump spot increase. Here a 50W seed was amplified up to 300W with the pump power  $P_p = 1100W$  (19 bounces case), what is ~35% less than the output power in case of 8mm pump spot (410W, **Figure 4-35**). It exactly corresponds to the decrease of the pump flux, which is inversely proportional to the pump spot area:

$$F_{10mm} = \left(\frac{8}{10}\right)^2 F_{8mm} = 0.64 F_{8mm}.$$

Significant increase of the output power connected to the seed ellipse expansion motivated another experiment: manual alignment of the seed into two spots (inside the pumped area) instead of one. When a round seed spot turns into an ellipse, all the individual bounces are still partially overlapped around the ellipse center. The most effective energy extraction happens during the last several bounces, while the first bounces deplete the UEL much less. This means, that if some of those last bounces are more separated from each other and extract the energy from different areas, the gain can be higher.

### 4.3 Quasi-resonator configuration

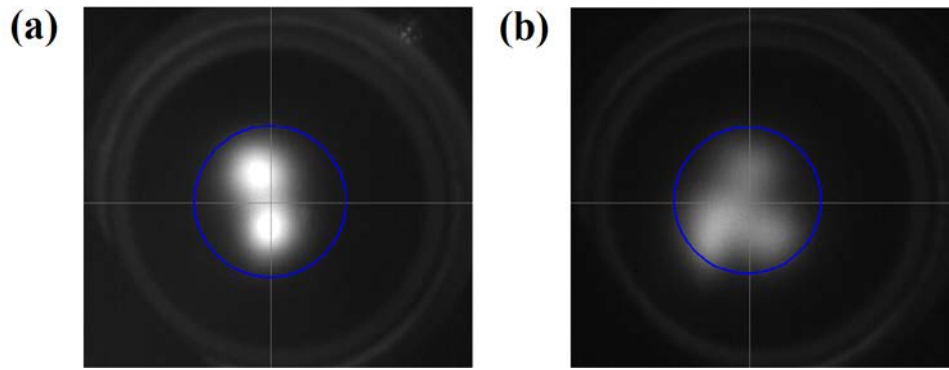


**Figure 4-37: Double seed spot alignment.**

(a) Nine seed bounces aligned into two different spots on Disk1. (b) Thermally induced displacement pattern of the double seed spot corresponding to the pump power  $P_p = 1100W$ . Blue circles represent the references of the pump spot.

Splitting the seed into two different spots from the beginning is one of the possible realizations of this idea, because the respective parts of the pump spot transfer the energy to only half of the bounces. **Figure 4-37a** demonstrates such an alignment within a 10mm pump spot. Resulting output power is shown in **Figure 4-38**.

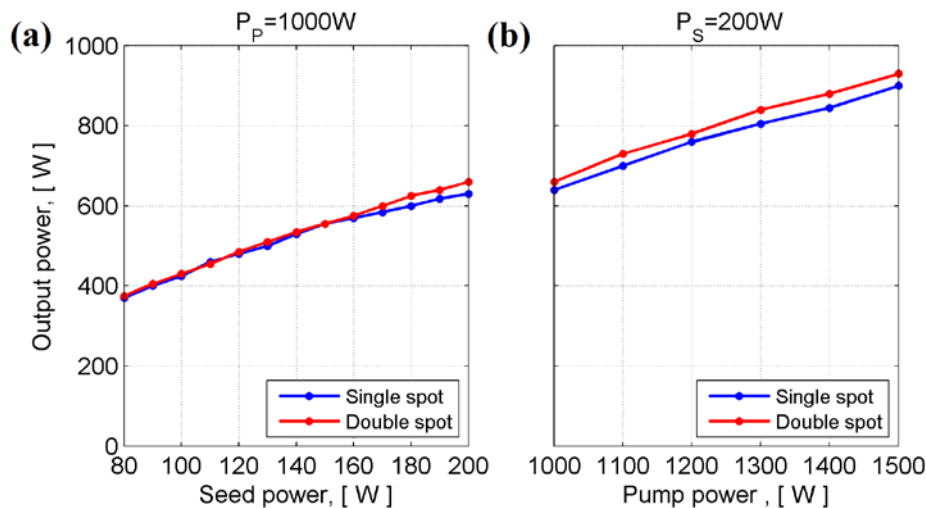


**Figure 4-38: Double seed spot amplification.**

(a) Fixed pump  $P_p = 1000W$ . (b) Fixed seed  $P_s = 200W$ . Parameters:  $D_{PS} = 10m$ ,  $D_{SS} = 4.4 \pm 0.7mm$ .

At low seed power there is no difference, because the UEL is almost not depleted. Starting from 100W seed the double spot alignment demonstrates a visible improvement, which grows up to almost 10% with the seed increase (due to stronger depletion of the disk in case of single seed spot). Increase of the pump power with a fixed seed does not change the output power ratio, what is expected. Such a strong seed leads to significant depletion within all the presented pump power range, thereby a stronger pumping just leads to a higher *equilibrium population* (see **Appendix B**) of the upper level. Thus both curves show proportional growth, which does not change their relation. Theoretically further increase of the pump power to some extreme values – so high, that either (*case 1*) extraction of the energy by 200W seed would be compensated before the next bounce happens, or (*case 2*) that it would lead to such a high equilibrium population, that all the 17 bounces would not noticeably deplete it any much –

## Chapter 4: Multipass amplifier

would make both curves merge again. But both of these cases are impossible in Yb:YAG, so a double spot alignment inevitably leads to a higher output power in case of such a strong seed.

However increase of the pump power above 1500W significantly reduced the stability of the system. It is again connected to the thermal drift of the seed bounces, which in case of a double seed spot is more chaotic than just an elliptic expansion. **Figure 4-37b** demonstrates such a displacement pattern corresponding to  $P_p = 1600W$ . There 930W of output power were obtained by amplifying a 200W seed with 1500W of pump power applied to both disks. In order to investigate the possibility of using double seed spot alignment more detailed, the same measurement with a bigger pump spot was performed. In analogy with the previous pump spot change (from 8mm to 10mm), it is expected to preserve the output power stability at higher pump power by keeping the seed beams inside the pumped area. **Figure 4-39** demonstrates the comparison of double seed spot amplification in case of 10mm and 11 mm pump spot size.

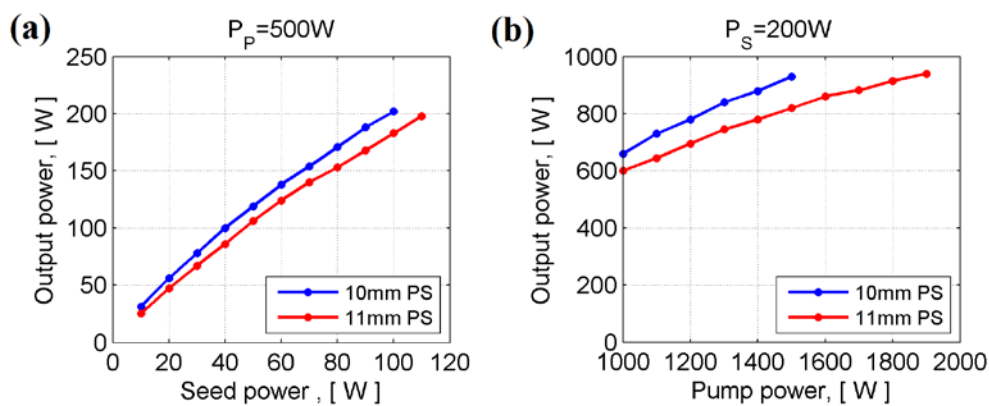


**Figure 4-39: Double seed spot amplification in case of bigger pump spot.**

(a) Fixed pump  $P_p = 500W$ . (b) Fixed seed  $P_s = 200W$ . Parameters:  $D_{SS} = 4.4 \pm 0.7mm$ .

Up to 1500W of pump power the bigger pump spot leads to just a 10% lower output power – it is even less than the pump flux drop, which in this case equals to 17%. But beyond 1500W the growth of the output power slows down - red curve on subfigure (b) deviates from its almost linear behavior. Increase of the pump spot to such a big value causes significant increase of the ASE losses, which also grow with the pump increase. In the end the same 930W of output power can be reached only at 1900W of pump power, when increased thermal load again shifts the seed to the edge of the pump spot and the system becomes unstable.

Thus usage of a double seed spot is only beneficial when the pump power is relatively low and corresponding thermal misalignment is small. But in this regime a single seed spot and smaller (8mm) pump spot would be even better, because the elliptic misalignment is predictable and can be partially pre-compensated. Another possibility to make use of double seed spot is to compensate the displacement of the seed by using adjustable disks optomechanics (will be discussed in the last chapter). If such compensation appears to be possible, a double seed spot might become beneficial. For a single seed spot the energy extraction area is limited by the eigenmode size, which is defined by the propagation length of a single iteration and according to **Figure 4-21** can hardly be significantly increased within reasonable physical dimensions of the amplifier.

## 4.3.7 Characterization of the output beam

Based on all the experiments with different amplification conditions, the best configuration in terms of output power and stability is a partially pre-compensated single seed spot and a 10mm pump spot. Such parameters allowed to reach above 1000W of output power with a good beam quality and stability. Corresponding measurements data will be demonstrated below.

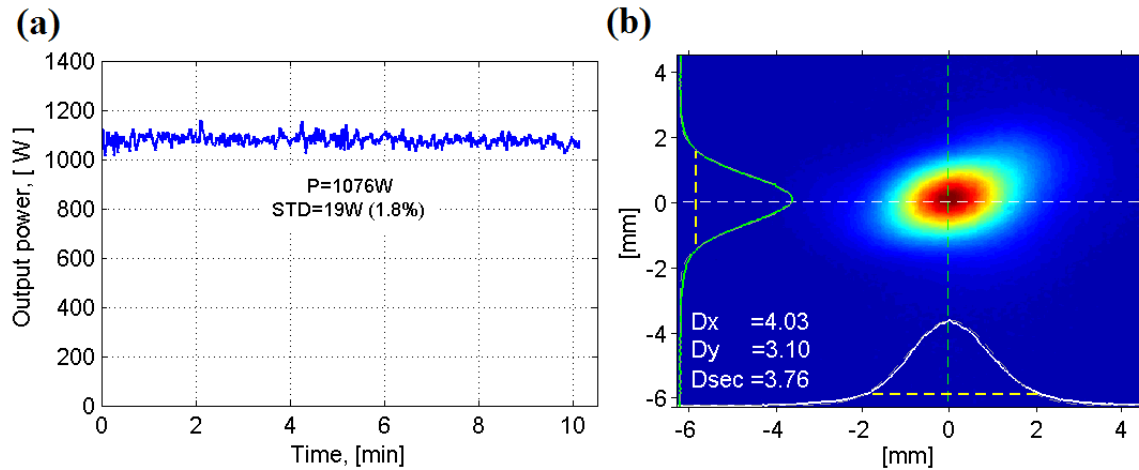


**Figure 4-40: Stable operation at 1kW.**

(a) Output power trace. (b) Output beam profile. Parameters:  $D_{PS} = 10\text{mm}$ ,  $D_{SS} = 4.4 \pm 0.7\text{mm}$ ,  $P_S = 230\text{W}$ ,  $P_P = 1900\text{W}$ .

Maximal reached output power of 1200W ( $P_S = 250\text{W}$ ,  $P_P = 2000\text{W}$ ) has been being observed for roughly 10 seconds. At 1076W ( $P_S = 230\text{W}$ ,  $P_P = 1900\text{W}$ ) the amplifier demonstrated stable operating for more than 10 minutes. Corresponding power trace and the output beam profile are presented in **Figure 4-40**. For a complete characterization of the beam quality several  $M^2$  measurements with the beam propagation analyzer *Ophir Spiricon M2-200* were performed. Without amplification  $M^2$  values are  $M_X^2 = 1.09$ ,  $M_Y^2 = 1.07$ , what is comparable with the input beam and indicates the absence of any significant wavefront distortions by the mirrors and unpumped disks.

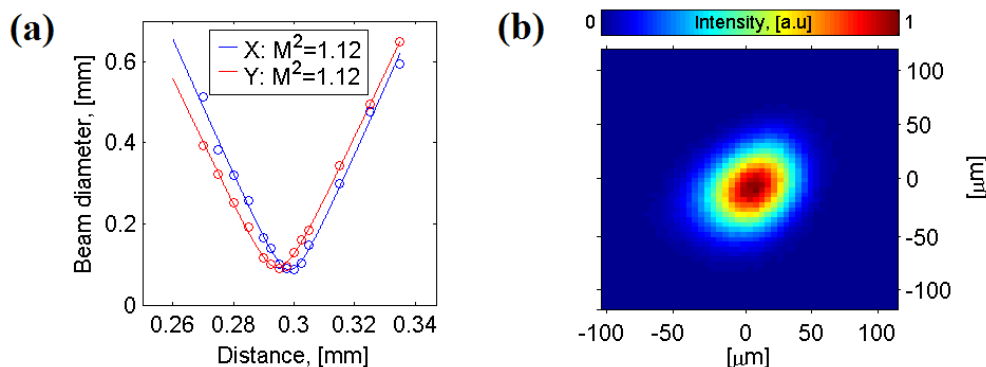


**Figure 4-41:  $M^2$  measurement at 1kW output power.**

(a) Beam diameter ( $1/e^2$ ) along the  $z$ -coordinate. (b) Beam profile in the focus. Before being sent to the  $M^2$ -meter, the beam is attenuated using two fused silica wedges.

## Chapter 4: Multipass amplifier

**Figure 4-41** shows the measurement corresponding to 1kW of output power, which also demonstrates a perfect beam quality with slightly bigger values  $M_X^2 = M_Y^2 = 1.12$ . Demonstrated beam quality is unique for multipass amplifiers operating at such high average power and pulse energy [67, 68, 69] and can be considered as the result of using the quasi-resonator optical scheme with its mode-preserving property.

In contrary to the beam quality, the spectrum and pulse duration cannot be preserved because of the physical processes laying behind the amplification. Exponential law of the light amplification and non-homogeneous, narrow-peak shape of Yb:YAG emission cross-section lead to the gain narrowing effect. Usually multipass amplifiers have much less passes through the active medium and thus significantly smaller total gain  $G$  than the resonators, but 17 bounces and  $G = 5$  is already enough to observe this effect. Corresponding input and output spectra are presented in **Figure 4-42** and demonstrate a 5% narrowing at half maximum level (7% at  $1/e^2$ ), which corresponds to increase of the shortest possible (Fourier limited) pulse duration from 800fs (that the input beam would have in case of perfect compression) to ~850fs.

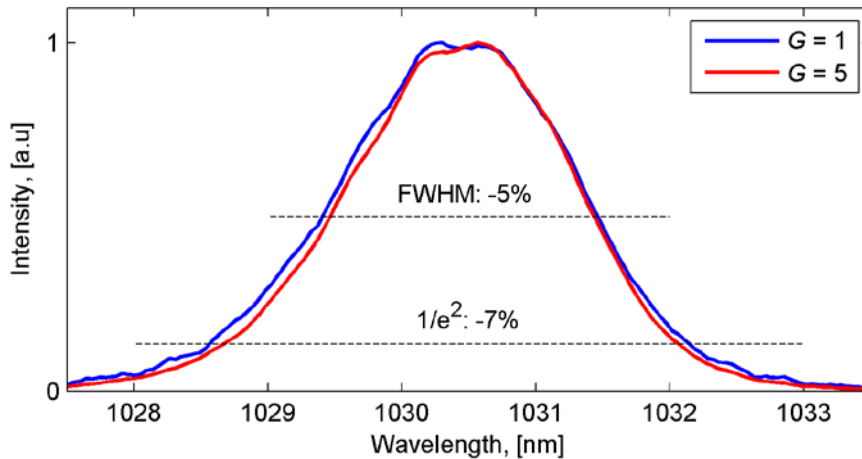


**Figure 4-42: Narrowing of the output spectrum.**

Comparison of the normalized output spectrum with ( $G = 5$ ,  $P_p = 1250W$ ) and without ( $G = 1$ ,  $P_p = 250W$ ) amplification for the same seed power. Dashed lines with specified values show the relative change of the bandwidth at half maximum and  $1/e^2$  levels. Parameters:  $D_{PS} = 10mm$ ,  $D_{SS} = 4.4 \pm 0.7mm$ ,  $P_S = 100W$ .

For a given combination of the active medium (namely, its emission cross-section) and the seed beam spectra, this effect is natural and unavoidable, so it is more important to check, that amplification does not corrupt the phase of the stretched pulse and it can be recompressed afterwards. For this purpose a portion of the output beam is sent to the same compressor setup that was used to demonstrate compression of the seed laser. This compressor supports up to 1kW power, what was demonstrated in [18]. In order to avoid possible compressor optics damage due to a different output beam profile from the amplifier (comparing to the source laser) only 15W from a kilowatt were used to show the compressibility of the output pulse. After the compression the beam was characterized using a home-made second harmonic FROG setup [70]. Measured signal and its retrieval, corresponding to 1kW output power are presented in **Figure 4-43**.

### 4.3 Quasi-resonator configuration

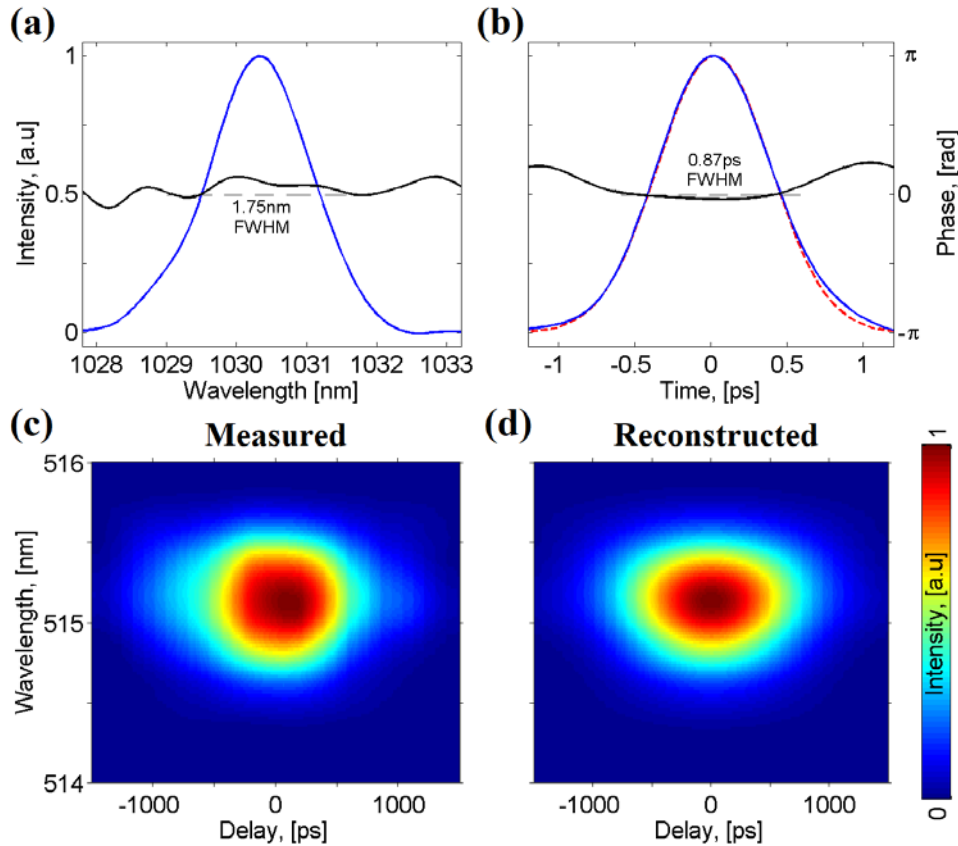


**Figure 4-43: Measurement of the output pulse duration.**

(a) Reconstructed spectrum (blue) and spectral phase (black). (b) Corresponding temporal intensity profile (blue) and temporal phase (black). Dashed red line shows the Fourier limited pulse. (c) and (d) – measured and reconstructed FROG traces respectively. G-error is 0.65%

Demonstrated FROG data show, that the output pulse is almost perfectly compressed: its temporal profile perfectly matches the Fourier limited pulse within FWHM and only a small elongation on the bottom part of the slopes indicates existence of some uncompensated spectral phase. But taking into account, that the compressor was not optimized at all – it is aligned for optimal compression of the source laser – such a compression quality is more than satisfactory and implies a complete absence of any unwanted phase modification during the amplification process. Spectral bandwidth is 1.75nm, which corresponds to ~13% narrowing comparing to the input spectrum and leads to 9%<sup>1</sup> longer pulse duration:  $\tau_{FWHM} \approx 870fs$ . Such values are comparable with the spectral narrowing measured at lower seed power (**Figure 4-42**). A low G-error of 0.65% indicates good reconstruction quality and thus reliability of the output pulse characterization.

<sup>1</sup> Discrepancy between the calculated spectrum narrowing (13%) and the pulse extension (9%) appears from the fact, that they are defined at half maximum level, while the spectrum is not purely Gaussian and contains more spectral components outside the FWHM range.

## 4.4 Potential for further development

At the current stage of development the presented multipass amplifier demonstrates reliable operation at 5kHz providing above 200mJ well-compressed sub-picosecond pulses with a good beam quality. However the measurements aimed for characterization and understanding of the amplification process revealed several promising modifications, which might significantly improve the system. These modifications are explained in the next two paragraphs and will be tested in the nearest future.

### 4.4.1 Amplification enhancement

One of the possible system upgrades is the so called *double passing*, which means back reflection of the seed beam in the completely opposite direction and reproducing exactly the same path backwards. It multiplies the amount of passes through the gain medium twice but requires some special polarization-based separation of the input and output beams. The principle of realization is explained in **Figure 4-44**.

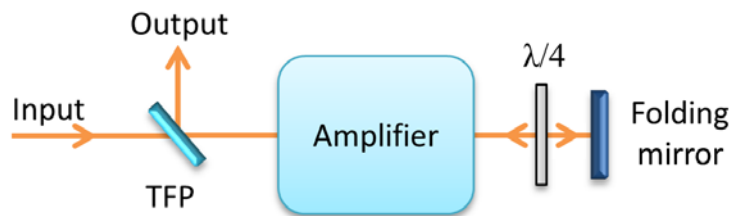


**Figure 4-44: Double-passing principle.**

A thin film polarizer in front of the amplifier transmits the input beam, but reflects the output, whose polarization was rotated by  $90^\circ$  by passing twice through a quarter-wave plate.

A linearly polarized input beam propagates through a polarizer whose orientation is matched to the transmission. After complete propagation through the system the output beam is sent backwards by a folding mirror. In order to separate the input and the output beams (after double propagation through the whole system) a quarter-wave plate is installed in front of the folding mirror. Two passes through a quarter-wave plate (there and backwards) rotates the polarization of the beam by  $2 \times 45^\circ = 90^\circ$ , which leads to reflection of the output beam by the first polarizer.

Such a method has been tested in a different setup with 9 bounces over a single small disk in  $4f$ -imaging configuration – at the stage of testing the circular geometry of the multipass. Though the parameters were different ( $D_{disk} = 9mm$ ,  $D_{PS} = 3.9mm$ ,  $D_{SS} = 2.5mm$ ), an obvious improvement of the gain was observed: in the small signal regime (5W seed and 500W pump power) the output power of 18.5W was obtained after 9 passes while double passing led to 51W. Total gain of the first 9 passes is  $G_{1-9} = 18.5/5 \approx 3.7$ , which corresponds to the average single bounce gain  $G_{ASB1-9} = 3.7^{1/9} \approx 1.16$ . Additional gain of the double-passing is  $G_{10-18} = 51/18.5 \approx 2.76$  with the corresponding average single bounce gain  $G_{ASB10-18} = 2.67^{1/9} \approx 1.12$ , which is  $\sim 4\%$  lower. It can be explained by stronger depopulation

## 4.4 Potential for further development

of the upper energy level due to higher energy extraction (46W against 13.5W with the same 500W of the pump power).

Of course this extra gain will be significantly lower in case of high power seed because of much stronger depletion of the disks. It can even lead to an opposite effect due to complete depopulation of the UEL and breaking of the inversed population condition. However high power seed amplification with 17 and 16 bounces (**Figure 4-36c**) indicates, that even at  $P_p = 1000W$  there is enough energy left in the disks and additional bounces would increase the total gain factor. Based on the simulations (**Figure 4-45**) full doubling ( $2 \times 17 = 34$ ) is not needed, because after 32 bounces absorption exceeds the energy extraction and the output power decreases. Moreover, increase of the propagation distance inside the amplifier will negatively affect the stability of the system. Therefore using more than 24 bounces is absolutely inefficient: at this point 97% of the maximum possible power is reached within  $\sim 215m$  of propagation while the last 3% would require 70m more. Thus 4 last iterations of the current configuration can be removed and double passing should be applied to the first 6 iterations providing 12 bounces over each of two disks.

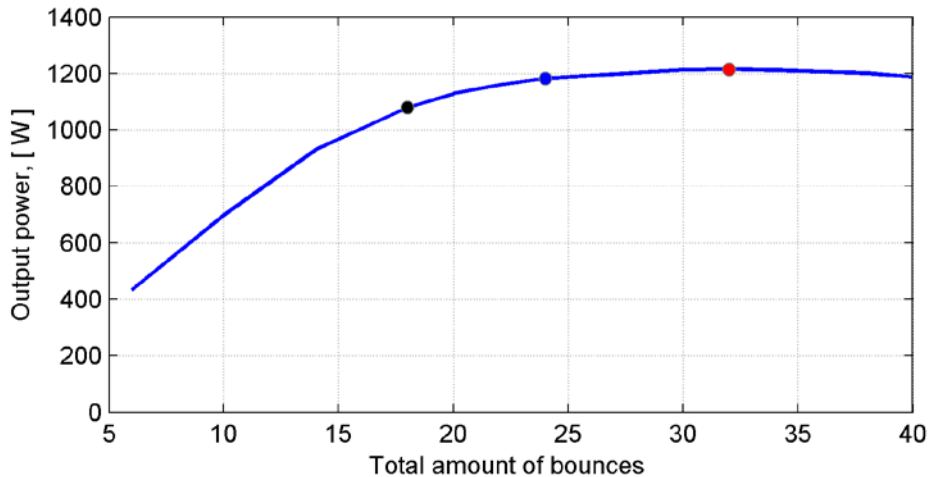


**Figure 4-45: Optimal amount of bounces.**

Simulation of the output power as a function of the amount of bounces over the disks. Black dot corresponds to 18 bounces, which is close to the experimental conditions described in paragraph 4.3.7. Red dot corresponds to 32 bounces leading to the maximal possible (theoretically) power. Blue dot – estimated optimal (includes the stability consideration) corresponding to 24 bounces. Parameters:  $D_{PS} = 10mm$ ,  $D_{SS} = 4.4 \pm 0.7mm$ ,  $P_S = 200W$ ,  $P_p = 1900W$ .

The drawback of double passing approach is the need for a *Faraday rotator* for isolation of the source laser from the leakage light that can pass through the TFP regardless of its polarization. It is based on the magneto-optic Faraday effect, that leads to a different propagation of the light through the crystal (usually terbium gallium garnet) in forward and backward direction in a presence of a strong magnetic field. However thermal lensing effects in Faraday rotators can significantly worsen the beam quality and thus limit the power of the seed beam [71].

Non-imaging configuration is also expected to perform differently from 4f-imaging in terms of seed beam alignment and system stability. It requires correct preservation of the eigenmode while sending the beam back. But it should anyway provide a higher output power or at least the same output power with a significantly lower seed power, leading to a higher total power of

## Chapter 4: Multipass amplifier

two beams: the output of the multipass amplifier and the unused part of the source laser output – both can be utilized as pump beams in the OPA amplification stages.

Another improvement that is expected to be highly beneficial is the motorization of the disk mounts. Since the applied pump power was limited by thermally induced seed misalignment, compensation of this effect should lead to improvement of the total gain via increase of the pump flux. Investigation of this effect showed, that manually introduced misalignment of the disk (described in paragraph 4.3.4) partially reproduces the elliptic expansion of the seed spot and its translation within the pump spot without any noticeable change of the pump spot shape or its position. Taking into account that the seed misalignment depends on the applied thermal load, motorization of the disk mounts should allow for a real-time compensation during the stepwise increase of the pump and seed powers while controlling the stability of the output power and the output beam profile. Due to high sensitivity of the seed beam propagation to any small tilt of the disk – which also leads to small maximal amplitude of the tilt and consequently small adjustment range – precise piezo motors are expected to be the best tool for realization of this idea.

If thermal misalignment can be counteracted by the motorization, linear scaling of the setup dimensions would allow for some increase of the eigenmode size (according to **Figure 4-21**). One extra meter of the central connecting tube length increases the disk-to-disk distance from 9m to 12m, which leads to a 14% bigger eigenmode. It would not only reduce the seed flux on the mirrors (by ~30%) allowing for a higher maximum pulse energy, but would also improve the energy extraction by increase of the seed-to-pump spot sizes ratio. Without compensation of thermal misalignment by using motorized disk mounts such a linear scaling of the setup is expected to additionally increase the amplitude of the seed displacement (the ellipse axes size) which will reduce the maximal possible pump power even more. Alternatively to such increase of the mode size the energy extraction can be improved by using the double seed spot alignment, which increases the effective seed-to-pump spot sizes ratio without changing the setup design. However it is impossible to predict, which approach is more beneficial and both of them have to be tested.

### 4.4.2 Operation at 1kHz

Though the amplifier did not exceed the maximum power of the source laser (which is 1.2kW) yet, it has a great usability reserve in terms of scaling the output pulse energy by changing the repetition rate. All the measurements and tests demonstrated in sections 4.2 and 4.3 were performed at the seed pulses repetition rate of 5kHz, what correspond to 200mJ of pulse energy at 1kW output power. However modern high average power OPA systems [72, 73] – aimed for driving different XUV sources [74] and approaching the pulse features that allow for generation of isolated attosecond pulses [14, 24] – operate at 1kHz and thus would benefit more from higher pulse energy of the pump laser than from its higher repetition rate. Since the main goal of this work is to push the development of the pump lasers towards the parameters, that would improve such high average power few-cycle lasers, investigation of 1kHz operation regime is also important.

## 4.4 Potential for further development

From this point of view the developed multipass amplifier is quite flexible. Reduction of the seed pulses repetition rate down to 1kHz should increase the gain, because according to equation 3.21 a longer pumping between two consecutive seed pulses leads to a higher population inversion. Though this will also increase the ASE losses, the gain raise should dominate due to the relatively long upper level life time of 1ms. In order to fully utilize the advantage of the lower repetition rate, the amplifier can be also switched to pulsed pumping [75] which is expected to reduce thermal load and associated problems. In order to estimate the gain increase in 1kHz regime a set of simulations was performed. **Figure 4-46** demonstrates the results of these simulations.

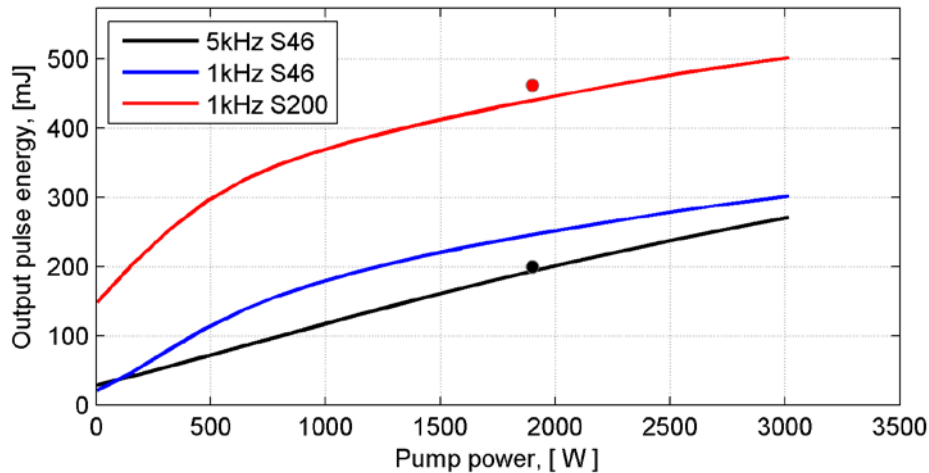


**Figure 4-46: Simulation of the output pulse energy at 1kHz.**

Black line shows simulation for 5kHz, 230W (46mJ) seed. Black dot – measured output power at this condition. Blue line corresponds to 1kHz with the same seed pulse energy, red line – 1kHz and 200mJ seed pulses. Red dot – estimated experimental output power. All three curves already include the additional gain caused by the seed ellipse expansion.

Here the output pulse energy at the pump power of 1900W is important since any higher pump power leads to the seed misalignment and amplification instability<sup>1</sup>. According to the numerical model reduce of the repetition rate down to 1kHz increases the output pulse energy by 25%. Such an improvement is quite small comparing to 80% decrease of the repetition rate and the resulting output power is 4 times lower. However at lower repetition rate the average seed power inside the disks is also lower. Thus the output pulse energy can be increased by increasing the seed pulse energy, which is for currently available source laser is 200mJ. In a first approximation it should not lead to any extra damage probability until the same average output power of 1kW is reached. For a 200mJ seed simulated output pulse energy is 440mJ at 1.9kW pump power. In 5kHz regime measured output power was 5% higher than the calculated value, so around 460mJ can be estimated. This value corresponds to the peak flux of  $\sim 5\text{J}/\text{cm}^2$  on the disks and  $\sim 7\text{J}/\text{cm}^2$  on the steering mirrors, which lay within the estimated damage threshold (see **Appendix C**).

<sup>1</sup> Thermally induced problems should diminish at 1kHz, especially if the pulsed pumping is used. But the same time additional gain related to the seed ellipse expansion can vanish. Thus the same behavior as for 5kHz regime was assumed for estimation of the possible output pulse energy.

## **Chapter 4: Multipass amplifier**

Summarizing all these numbers it can be concluded, that without any design changes the developed multipass amplifier can also operate at 1kHz providing almost 0.5J pulses. If the upgrades and modifications that are discussed in the previous paragraph succeed and help to suppress thermally induced misalignment of the seed beam, the output pulse energy can be additionally increased by using higher pump powers and a bigger seed-to-pump spot sizes ratio.

# Summary and outlook

The most intense few-cycle laser to date [12] was used for generation of isolated attosecond pulses via relativistic interaction with overdense plasma created on solid surfaces. Generated XUV emission was presented by the pulse trains consisting of two or three non-equidistant attosecond pulses with the photon energy up to 100eV. Though the carrier-envelope phase of the driving laser was random, measuring and tagging it to the spectra of the generated XUV emission revealed a clear correlation. A novel interferometric approach [14] was invented for analysis of the resulting dependence of the harmonics pattern on the CEP of the driving laser pulses. This treatment provided enough information for complete temporal reconstruction of the generated pulse trains, which in turn allowed to recognize the spectra that belong to highly isolated attosecond pulses and define the corresponding CEP range. Thus the used laser system and harmonics generation approach were proved to be suitable for routine generation of isolated attosecond pulses, if the carrier-envelope phase of the laser is stabilized. Such a modification of the driving laser does not present any serious scientific challenge since various existing approaches have been successfully implemented in many other laser systems [34, 35].

In contrary to this, scaling the repetition rate towards desired kilohertz level requires significant improvement of the existing laser technologies. Besides high average power and pulse energy, few-cycle OPA-based lasers would benefit from good beam quality and relatively short duration of the pump pulses. Based on these requirements the researcher's efforts were aimed at designing and investigation of a high power multipass amplifier that would improve the existing pump laser [18] and reveal the pros and cons of different approaches for further development in this direction. Two thin Yb:YAG disks were used as the gain medium. Their unique thermal and optical properties allowed for creation of a system, which at 5kHz repetition rate amplifies 46mJ seed pulses almost five times, providing above 1kW of the output power while preserving a perfect beam quality ( $M^2 \approx 1.12$ ) and almost Fourier limited pulse duration of 800fs.

The key solution for reaching such parameters is the quasi-resonator optical scheme, which due to a special folding geometry and a circularly-symmetric optics allocation provides 17 bounces over the disks (their geometry supposes double-passing through the crystal for each bounce) and thus compensates their low single-pass gain, which is a natural consequence of the low thickness. High power CW pump lasers played an equally important role in reaching efficient amplification: almost 2kW of pump power were delivered to each of the disks via multimode optical fibers, resulting into the amplification factor  $G \approx 5$  for a strong 200W seed beam. This indicates conversion of 860W of the pump power into the seed and corresponds to ~23% optical efficiency. Correct propagation of the seed beam inside the amplifier for more than 150m was only possible due to the precise matching of the input beam to the eigenmode and careful investigation and pre-compensation of a thermally induced misalignment. This unwanted thermal effect appeared to be one of the main factors limiting the efficiency of the amplifier and its maximum output power. Though the pump lasers could provide much higher power and the

## Summary and Outlook

pump flux on the disks was also significantly below the allowed safe level, increasing the pump power above 2kW was not possible because of too strong misalignment of the seed beam.

Imaging approach was proved to be inappropriate for efficient amplification of a high power seed beam using thin disks. Low disks thickness does not allow accumulating enough gain within few passes, while increase of the number of passes leads to a significant beam degradation and results in optics damages. Imaging induced multiplication of the pumping-related soft aperture effect is assigned to be the main reason of such strong beam distortions. Counteracting it by decreasing the seed-to-pump spot sizes ratio drastically decreases the amplification efficiency and leads to a very low total gain. Nevertheless the  $4f$ -imaging configuration has one important advantage: thermal misalignment of the system does not affect the seed position on the disks and only causes the beam displacement on the imaging optics. Thus few passes amplifiers, which are usually based on thicker crystals in order to have enough gain and therefore operate at much lower repetition rates [76, 77], can benefit from the imaging propagation scheme. Correspondently low amount of involved imaging mirrors allows for bigger apertures, which would accept bigger misalignment amplitude. Good thermal stability also means that a high seed-to-pump spot sizes ratio can be used for additional improvement of the single pass gain: the aperture effect should not lead to any significant degradation of the beam quality due to a relatively low amount of bounces in such amplifiers.

At the current stage of development the output power and pulse energy of the described amplifier do not exceed the corresponding parameters of the source laser, which at 5kHz demonstrated stable operation with the output power of 1014W (including the losses in the compressor). However further scaling of the pulse energy of this regenerative amplifier based laser is not possible because of the optical switch operating close to its damage threshold [19, p46–48]. The same time according to the mode size the new amplifier should support up to 500mJ pulses. It means, that successful solving of the thermal misalignment problem via motorization of the disk's mechanics would allow for utilization of the full 4kW power of the pump lasers, which according to the simulations should lead to the output power of ~1500W in 5kHz operation regime. Moreover, based on the measured data and numerical simulations the system can provide significantly higher pulse energy in the cost of average power: being seeded at 1kHz, it should be able to amplify the 200mJ pulses of the source laser up to half a joule level – without any modifications and change of the design. Just the source laser parameters should be adapted.

Based on the presented results and ideas it can be summarized, that the described multipass amplifier does not only demonstrate a good performance at the current stage of development, but also has a great improvement potential for reaching parameters that haven't been available yet. It is a relatively small, but nevertheless an important step towards kilohertz-class few-cycle laser systems, which in the nearest future will push the attosecond science to a completely new level.

# Appendix A

## Prepulse generation

A small quarter-inch mirror was installed on a motorized stage in front of the last mirror before focusing. It reflected a small portion of the main beam in the same direction, but with a shorter optical path, which leads to arriving before the main pulse by a certain time called prepulse delay. The prepulse mirror was inserted with its reflecting surface on the back, as it was demonstrated in [78]. Thus the beam propagated through a thin glass layer before and after being reflected (**Figure S-1**). This provided a delay that is needed for reaching zero-delay while the prepulse mirror was installed in front of the main mirror. The mirror position corresponding to zero-delay was calibrated with the interference between the main pulse and the prepulse observed at focus. The prepulse delay was adjustable in the range from  $-1.5\text{ps}$  to  $12\text{ps}$ , where negative values indicate a postpulse instead of a prepulse and were used as “no prepulse” case during the experiment. The intensity of the generated prepulse at focus was estimated to be  $10^{-4} - 10^{-5}$  of the main pulse according to the pulse elongation in the glass and camera signal at focus, which indicated a 6 times larger spot size and 100 times lower energy relatively to the main pulse. **Figure 1-8** demonstrates the dependence of the measured XUV signal intensity on the prepulse delay.

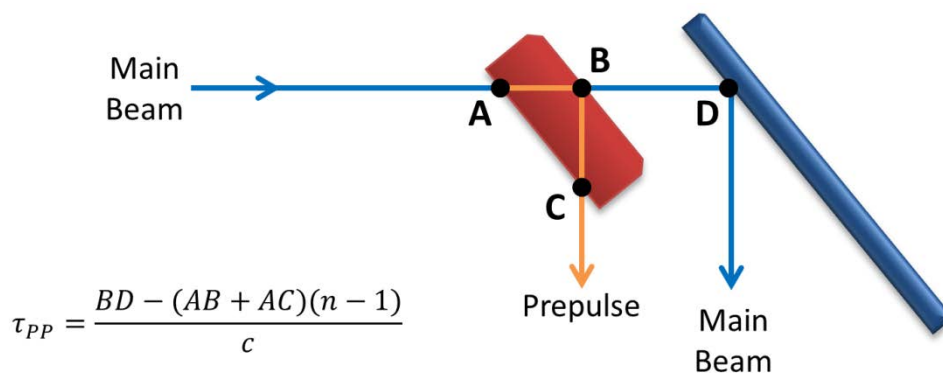


**Figure S-1: Prepulse generation.**

Blue bulk line is the beamline steering mirror, red bulk – prepulse mirror (thickness and dimensions are exaggerated). Blue line corresponds to the propagation of the main beam without prepulse mirror, orange line – part of the beam path that belongs to the prepulse. Adjustable distance  $BD$  corresponds to the retard of the main beam, while fixed propagation  $ABC$  – compensatory delay of the prepulse caused by the slower propagation of the beam in the glass.

**Appendix A: Prepulse generation**

# Appendix B

## Amplification simulation

### B.1 Basic assumptions

Numerical simulations of the amplification in thin disks are based on the equations presented by Martin Kaumanns in his work “*Generation of Energetic Femtosecond Pulses at High Average Power*” [19, p139–144], where among other results the development of a high power picosecond-class laser (that is used as the source laser for the multipass amplifier) is presented. The key points of this numeric approach are explained below.

**Quasi 2-level system.** Energy levels of Yb:YAG are approximated by a 2-level system (paragraph 3.2.1) according to its emission and absorption cross-section peaks around 940nm and 1030nm respectively.

**Separation of the pump and amplification phases.** The repetition rate of the seed laser is 5kHz which means that the seed pulse arrive every 0.2ms. Since their propagation through the amplifier (~180m) lasts roughly 0.6 $\mu$ s, amplification process of each pulse can be split into two phases. During *phase I* the pulse is bouncing several times between two disks while being amplified. On this time scale only the stimulated emission leading to depletion of both disks is important. Influence of the pumping and spontaneous emission to the population distribution can be rightfully considered as negligible due to the shortness of this phase relatively to the life time of the Yb:YAG upper state ( $\tau \approx 1ms$ ) and the period between two consecutive seed pulses. Thus the propagation distance between two disks can be ignored and the whole amplification phase can be described as alternating passing through the two disk  $N_{bounces}$  times. When the pulse leaves the amplifier *phase II starts*: pumping restores the population of the upper level of both disks by exciting the electrons from the lower level. The ASE losses are considered according to the worst case model presented by Speiser in [57], which assumes that all the spontaneous emission happens at 1030nm and thus is amplified the most.

**Equilibrium state.** Output pulse energy can be calculated in a very simple way as soon as the quasi *equilibrium state* is defined, i.e. what populations do the upper and lower levels reach at every cycle before a new pulse comes. Without energy extraction the population of the upper level does not grow continuously during pumping phase but always reaches some saturation level  $N_{sat}$ , which depends only on the pump flux and the disk material and defines ASE losses. If the period of the seed pulses significantly exceeds the lifetime of the upper state ( $f_{seed} < \tau^{-1} \approx 1kHz$ ), every new pulse comes to a saturated disk and experiences the same gain, which means that  $N_{sat}$  is the wanted equilibrium condition. However for above 1kHz repetition rate the seed pulses come before the population reaches saturation. **Figure S-2**

## Appendix B.2: Seed ellipse expansion

schematically describes the dynamics of the upper state population for such a case and explains the meaning of the equilibrium state.

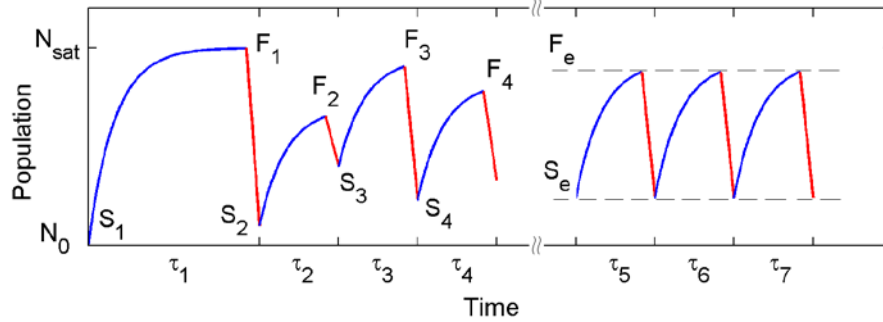


**Figure S-2: Dynamics of the upper state population.**

Y-axis shows the population of the UEL, x-axis – time. The figure demonstrates seven time periods consisting of a pump phase (blue curves  $S_n F_n$ ) and an amplification phase (red curves  $F_n S_{n+1}$ ) where a new seed pulse arrives to the disk and extracts the energy. Here  $S_n$  mean the starting populations in the beginning of the periods and  $F_n$  is the final populations. Duration of the amplification stage is exaggerated for better visibility. All the periods  $\tau_{2-7}$  have the same duration, while the first period  $\tau_1$  is significantly longer. **Period  $\tau_1$ :** Long pumping without any energy extraction allows reaching the maximal (for a given pump power) population  $F_1 = N_{sat} > F_e$ . Further increase of the population is not possible due to significant increase of the ASE losses. Because of this the first seed pulse has the maximal possible gain, which in turn leads to the strongest depletion.  $S_2 < S_e$ . **Period  $\tau_2$ :** pumping from a strongly depleted state leads to an under-populated condition  $F_2 < F_e$ . This leads to a small gain for the arriving seed pulse and a correspondently small depletion. The final state is under-depleted:  $S_2 < S_e < S_3$ . **Period  $\tau_3$ :** Due to the relatively high starting population  $S_3$  some over-pumping takes place:  $F_e < F_3$ . Consecutive amplification event will lead to slight over-depletion:  $S_4 < S_e < S_3$ . After some time such a sequence should converge to the quasi-equilibrium with the same starting and final populations  $S_e$  and  $F_e$  as well as the constant gain that all the seed pulses experience.

Thus the equilibrium state can be numerically found for given input parameters (pump and seed power, disk thickness and material etc.) by using the equation 3.31 sequentially for the pumping and amplification phases with equalized starting and final populations of the upper state.

## B.2 Seed ellipse expansion

As it was discussed in paragraph 4.3.6, within some acceptable range thermal misalignment of the seed leads to an elliptic pattern on the disk, which raises the gain above the calculated values via extraction of the energy from a bigger area. One of the simplest ways to describe this effect with minimal modifications of the code is to add an extra disk to each iteration, as if it would consist of 3 different disks instead of 2. Such a change has a very similar (just too much exaggerated) effect on amplification: every iteration the seed beam faces some additional fresh (less depleted) area and thus is being amplified more. However just adding a third disk that is pumped with the same pump will most likely lead to overestimation of the ellipse expansion effect. Thus some proportion between the values obtained from the normal 2-disks simulation and the modified 3-disks version is expected to be the most realistic. **Figure S-3** compares the measured data (**Figure 4-35**, high-gain measurement) with 3 different curves, obtained from simulations.

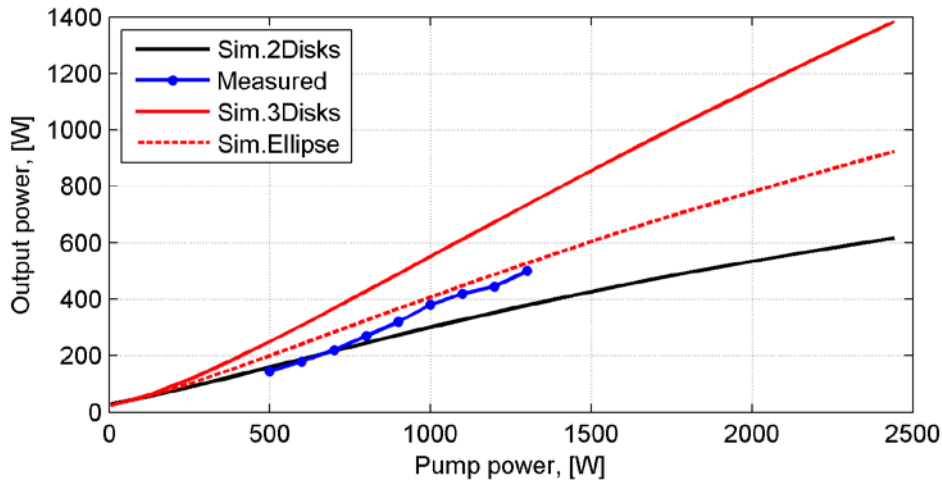


**Figure S-3: Simulations of the ellipse effect at low pump power.**

Blue line corresponds to the experimental data, black line – normal 2-disks simulation, red line – modified 3-disks simulation. Red dashed line – geometric mean ( $A = \sqrt{BC}$ ) of the red and black curves. Parameters:  $D_{PS} = 8mm$ ,  $D_{SS} = 4.4 \pm 0.7mm$ ,  $P_S = 50W$ ,  $N_{bounces} = 19$ .

At low pump power measured curve is close to the normal 2-disks simulation, because the seed pattern stays round. For a higher pump power the gain increases due to the seed ellipse expansion and the measured data gravitate to another curve, which is geometrical mean of 2- and 3-disks simulation. For additional prove of this concept another set of data, corresponding to the higher pump and seed power (**Figure 4-36c**, 17 bounces), was tested. Results are presented in **Figure S-4**.

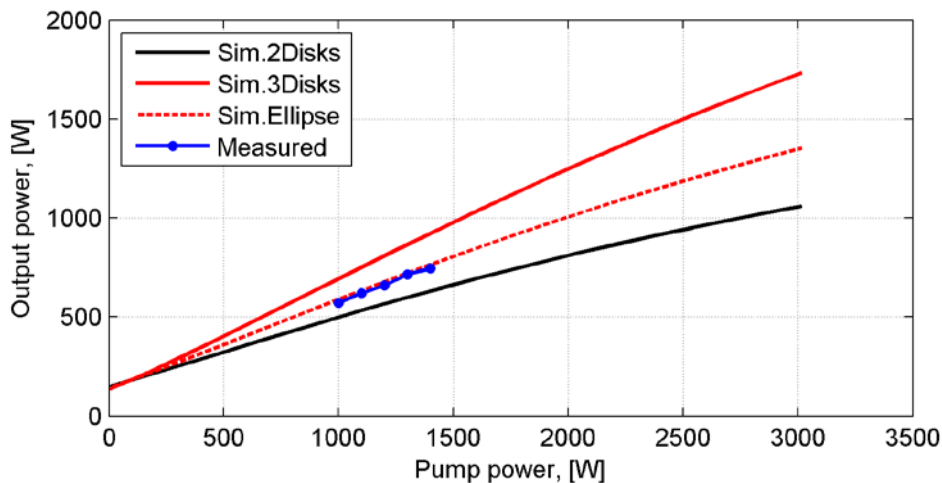


**Figure S-4: Simulations of the ellipse effect at high pump and seed power.**

Blue line – experimental data, black line – normal 2-disks simulation, red line – modified 3-disks simulation. Red dashed line – geometric mean of the red and black curves. Parameters:  $D_{PS} = 10mm$ ,  $D_{SS} = 4.4 \pm 0.7mm$ ,  $P_S = 200W$ ,  $N_{bounces} = 17$ .

Here the measured data show a perfect match with the geometrical mean curve. For the maximal stable output power of 1076W measured at  $P_S = 230W$  and  $P_P = 1900W$  such a simulation predicts the output power of 1018W, which is within the 6% precision. Thus it can be concluded, that within 1–2kW of pump power the additional gain caused by the seed ellipse expansion can be relatively well described using such a method.

**Appendix B.2: Seed ellipse expansion**

# Appendix C

## Damage threshold estimation

*Laser induced damage threshold* (LIDT) characterizes the light flux (or intensity) that given optical elements – in the context of the current work a mirror or a thin-disk – can withstand without being damaged. Since it does not only depend on the general material properties and the laser pulse parameters, but also on the quality of the exact samples (which can have different amount of defects), damage threshold value can be only defined statistically with some estimated probability.

In case of mirrors the estimated value is based on some amount (usually several tens) of damage events, which occur when a laser beam is by purpose focused on the surface: the pulse energy is being stepwise increased every few seconds (which means few thousands of shots for a kilohertz-class laser) until the damage happens and the corresponding value is added to the statistics. Repeating the measurement several times within the sample aperture for several random samples of the same production batch provides enough data to estimate the worst-case flux threshold that does not cause damage. Detailed description of the damage threshold flux calculation is described in [79, p137].

High-reflective mirrors used in this work (and also other projects in our laboratory) demonstrate the worst-case estimation of  $J_{LIDT} \approx 20\text{J}/\text{cm}^2$  for nanosecond pulses in normal operation and  $\sim 3$  times lower ( $J_{LIDT_{burst}} \approx 6\text{J}/\text{cm}^2$ ) while being used inside a resonator [19, p58], where the damage probability increases because the beam bounces many times over the same mirrors. Since all the imaging and steering mirrors in the multipass amplifier face each laser pulse only once, they should support the seed flux up to  $20\text{J}/\text{cm}^2$ .

Reproducing such a measurement for the disks cannot be performed because of the high cost of each sample. However in [51]  $700\mu\text{m}$  Yb:YAG disks were demonstrated to withstand  $4.5\text{J}/\text{cm}^2$  being tested by 100ps pulse in kilohertz regime. The authors also highlight, that the AR-coated front surface was always damaged first, which means that the given number should not depend on the disk thickness. Based on the power-law dependence of the damage threshold on the pulse duration  $J_{LIDT} \propto \sqrt{\tau}$  [19, p58], presented value can be extrapolated to  $\sim 14\text{J}/\text{cm}^2$  for 1ns pulses used in the developed multipass amplifier. Since the disks interact several times with each laser pulse, the burst correction factor should be also applied, which according to [19, p58] can be estimated between 2.2 (for  $G = 5$ ) and 2.5 (for  $G = 2.5$ ). This leads to the final (worst case) estimation of  $\sim 5.5\text{J}/\text{cm}^2$  for the disks in the described multipass amplifier.

**Appendix C: Damage threshold estimation**

# Appendix D

## Data archiving

All the data presented in the current work are archived on the server of the Laboratory for Attosecond Physics at Max Planck Institute of Quantum Optics and can be found in the following directory:

*/afs/ipp-garching.mpg.de/mpq.lap/publication\_archive/Theses/2021/Kormin, Dmitrii(PhD)*

Detailed explanation of the relation between the figures and the raw experimental data can be found in the document “*Legend.docx*”.

**Appendix D: Data archiving**

# Bibliography

- [1] B. Clegg, *The Man Who Stopped Time: The Illuminating Story of Eadweard Muybridge — Pioneer Photographer, Father of the Motion Picture, Murderer*. Washington, D.C.: Joseph Henry Press, 2007.
- [2] T. H. Maiman, “Stimulated optical radiation in ruby,” *Nature*, vol. 187, no. 4736, pp. 493–494, 1960, doi: 10.1038/187493a0.
- [3] E. P. Ippen, C. V. Shank, and A. Dienes, “Passive mode locking of the cw dye laser,” *Appl. Phys. Lett.*, vol. 21, no. 8, pp. 348–350, Oct. 1972, doi: 10.1063/1.1654406.
- [4] M. T. Hassan *et al.*, “Optical attosecond pulses and tracking the nonlinear response of bound electrons,” *Nature*, vol. 530, no. 7588, pp. 66–70, Feb. 2016, doi: 10.1038/nature16528.
- [5] M. Ferray, A. L’Huillier, X. F. Li, L. A. Lompre, G. Mainfray, and C. Manus, “Multiple-harmonic conversion of 1064 nm radiation in rare gases,” *J. Phys. B At. Mol. Opt. Phys.*, vol. 21, no. 3, pp. L31–L35, Feb. 1988, doi: 10.1088/0953-4075/21/3/001.
- [6] M. Hentschel *et al.*, “Attosecond metrology,” *Nature*, vol. 414, no. 6863, pp. 509–513, Nov. 2001, doi: 10.1038/35107000.
- [7] F. Krausz and M. Ivanov, “Attosecond physics,” *Rev. Mod. Phys.*, vol. 81, no. 1, pp. 163–234, 2009, doi: 10.1103/RevModPhys.81.163.
- [8] S. Kohlweyer, G. D. Tsakiris, C.-G. Wahlström, C. Tillman, and I. Mercer, “Harmonic generation from solid-vacuum interface irradiated at high laser intensities,” *Opt. Commun.*, vol. 117, no. 5–6, pp. 431–438, Jun. 1995, doi: 10.1016/0030-4018(95)00200-R.
- [9] C. Thauray and F. Quéré, “High-order harmonic and attosecond pulse generation on plasma mirrors: basic mechanisms,” *J. Phys. B At. Mol. Opt. Phys.*, vol. 43, no. 21, p. 213001, Nov. 2010, doi: 10.1088/0953-4075/43/21/213001.
- [10] M. Bellini, C. Corsi, and M. C. Gambino, “Neutral depletion and beam defocusing in harmonic generation from strongly ionized media,” *Phys. Rev. A*, vol. 64, no. 2, p. 023411, Jul. 2001, doi: 10.1103/PhysRevA.64.023411.
- [11] G. D. Tsakiris, K. Eidmann, J. Meyer-ter-Vehn, and F. Krausz, “Route to intense single attosecond pulses,” *New J. Phys.*, vol. 8, pp. 19–19, Jan. 2006, doi: 10.1088/1367-2630/8/1/019.
- [12] D. E. Rivas *et al.*, “Next Generation Driver for Attosecond and Laser-plasma Physics,” *Sci. Rep.*, vol. 7, no. 1, p. 5224, Dec. 2017, doi: 10.1038/s41598-017-05082-w.
- [13] M. Kübel *et al.*, “Carrier-envelope-phase tagging in measurements with long acquisition times,” *New J. Phys.*, vol. 14, no. 9, p. 093027, Sep. 2012, doi: 10.1088/1367-2630/14/9/093027.

## Bibliography

- [14] D. Kormin *et al.*, “Spectral interferometry with waveform-dependent relativistic high-order harmonics from plasma surfaces,” *Nat. Commun.*, vol. 9, no. 1, p. 4992, Dec. 2018, doi: 10.1038/s41467-018-07421-5.
- [15] O. Jahn *et al.*, “Towards intense isolated attosecond pulses from relativistic surface high harmonics,” *Optica*, vol. 6, no. 3, p. 280, Mar. 2019, doi: 10.1364/OPTICA.6.000280.
- [16] A. Borot *et al.*, “High-harmonic generation from plasma mirrors at kilohertz repetition rate,” *Opt. Lett.*, vol. 36, no. 8, p. 1461, Apr. 2011, doi: 10.1364/OL.36.001461.
- [17] H. Fattahi *et al.*, “Third-generation femtosecond technology,” *Optica*, vol. 1, no. 1, pp. 45–63, 2014, doi: 10.1364/OPTICA.1.000045.
- [18] T. Nubbemeyer *et al.*, “1kW, 200mJ picosecond thin-disk laser system,” *Opt. Lett.*, vol. 42, no. 7, pp. 1381–1384, 2017, doi: 10.1364/OL.42.001381.
- [19] R. M. Kaumanns, “Generation of Energetic Femtosecond Pulses at High Average Power,” Ludwig-Maximilians-Universität München, 2020.
- [20] A. Dubietis, G. Jonušauskas, and A. Piskarskas, “Powerful femtosecond pulse generation by chirped and stretched pulse parametric amplification in BBO crystal,” *Opt. Commun.*, vol. 88, no. 4–6, pp. 437–440, Apr. 1992, doi: 10.1016/0030-4018(92)90070-8.
- [21] D. E. Rivas *et al.*, “Propagation-enhanced generation of intense high-harmonic continua in the 100-eV spectral region,” *Optica*, vol. 5, no. 10, p. 1283, Oct. 2018, doi: 10.1364/OPTICA.5.001283.
- [22] B. Dromey *et al.*, “Bright Multi-keV Harmonic Generation from Relativistically Oscillating Plasma Surfaces,” *Phys. Rev. Lett.*, vol. 99, no. 8, p. 085001, Aug. 2007, doi: 10.1103/PhysRevLett.99.085001.
- [23] S. Inoue *et al.*, “Single plasma mirror providing  $10^4$  contrast enhancement and 70% reflectivity for intense femtosecond lasers,” *Appl. Opt.*, vol. 55, no. 21, p. 5647, Jul. 2016, doi: 10.1364/AO.55.005647.
- [24] G. Ma *et al.*, “Intense isolated attosecond pulse generation from relativistic laser plasmas using few-cycle laser pulses,” *Phys. Plasmas*, vol. 22, no. 3, p. 033105, Mar. 2015, doi: 10.1063/1.4914087.
- [25] R. Lichters, J. Meyer-ter-Vehn, and A. Pukhov, “Short-pulse laser harmonics from oscillating plasma surfaces driven at relativistic intensity,” *Phys. Plasmas*, vol. 3, no. 9, pp. 3425–3437, Sep. 1996, doi: 10.1063/1.871619.
- [26] D. E. Rivas, “Generation of Intense Isolated Attosecond Pulses at 100 eV,” Ludwig-Maximilians-Universität München, 2016.
- [27] T. Wittmann *et al.*, “Single-shot carrier-envelope phase measurement of few-cycle laser pulses,” *Nat. Phys.*, vol. 5, no. 5, pp. 357–362, May 2009, doi: 10.1038/nphys1250.
- [28] F. Tavella, K. Schmid, N. Ishii, A. Marcinkevičius, L. Veisz, and F. Krausz, “High-dynamic range pulse-contrast measurements of a broadband optical parametric chirped-pulse amplifier,” *Appl. Phys. B*, vol. 81, no. 6, pp. 753–756, Oct. 2005, doi: 10.1007/s00340-005-1966-3.

- [29] V. Lorient, G. Gitzinger, and N. Forget, “Self-referenced characterization of femtosecond laser pulses by chirp scan,” *Opt. Express*, vol. 21, no. 21, p. 24879, Oct. 2013, doi: 10.1364/OE.21.024879.
- [30] J. P. Christiansen, D. E. T. F. Ashby, and K. V. Roberts, “MEDUSA a one-dimensional laser fusion code,” *Comput. Phys. Commun.*, vol. 7, no. 5, pp. 271–287, May 1974, doi: 10.1016/0010-4655(74)90027-7.
- [31] T. Baeva, S. Gordienko, and A. Pukhov, “Theory of high-order harmonic generation in relativistic laser interaction with overdense plasma,” *Phys. Rev. E*, vol. 74, no. 4, p. 046404, Oct. 2006, doi: 10.1103/PhysRevE.74.046404.
- [32] “Bump Functions and Partitions of Unity,” in *An Introduction to Manifolds*, New York, NY: Springer New York, pp. 127–134.
- [33] B. Bergues *et al.*, “Tabletop nonlinear optics in the 100-eV spectral region,” *Optica*, vol. 5, no. 3, p. 237, Mar. 2018, doi: 10.1364/OPTICA.5.000237.
- [34] K.-H. Hong *et al.*, “High-energy, phase-stable, ultrabroadband kHz OPCPA at 21  $\mu\text{m}$  pumped by a picosecond cryogenic Yb:YAG laser,” *Opt. Express*, vol. 19, no. 16, p. 15538, Aug. 2011, doi: 10.1364/OE.19.015538.
- [35] Y. Deng *et al.*, “Carrier-envelope-phase-stable, 12 mJ, 15 cycle laser pulses at 21  $\mu\text{m}$ ,” *Opt. Lett.*, vol. 37, no. 23, p. 4973, Dec. 2012, doi: 10.1364/OL.37.004973.
- [36] J. Bierbach *et al.*, “Long-term operation of surface high-harmonic generation from relativistic oscillating mirrors using a spooling tape,” *Opt. Express*, vol. 23, no. 9, p. 12321, May 2015, doi: 10.1364/OE.23.012321.
- [37] K. Mecseki *et al.*, “High average power 88 W OPCPA system for high-repetition-rate experiments at the LCLS x-ray free-electron laser,” *Opt. Lett.*, vol. 44, no. 5, pp. 1257–1260, 2019, doi: 10.1364/OL.44.001257.
- [38] M. K. R. Windeler *et al.*, “100 W high-repetition-rate near-infrared optical parametric chirped pulse amplifier,” *Opt. Lett.*, vol. 44, no. 17, pp. 4287–4290, 2019, doi: 10.1364/OL.44.004287.
- [39] J. Rothhardt, S. Demmler, S. Hädrich, T. Peschel, J. Limpert, and A. Tünnermann, “Thermal effects in high average power optical parametric amplifiers,” *Opt. Lett.*, vol. 38, no. 5, pp. 763–765, 2013, doi: 10.1364/OL.38.000763.
- [40] R. Riedel *et al.*, “Thermal properties of borate crystals for high power optical parametric chirped-pulse amplification,” *Opt. Express*, vol. 22, no. 15, pp. 17607–17619, 2014, doi: 10.1364/OE.22.017607.
- [41] M. Kaumanns, D. Kormin, T. Nubbemeyer, V. Pervak, and S. Karsch, “Spectral broadening of 112 mJ, 13 ps pulses at 5 kHz in a LG 10 multipass cell with compressibility to 37 fs,” *Opt. Lett.*, vol. 46, no. 5, p. 929, Mar. 2021, doi: 10.1364/OL.416734.
- [42] K. Khrennikov *et al.*, “Tunable All-Optical Quasimonochromatic Thomson X-Ray Source in the Nonlinear Regime,” *Phys. Rev. Lett.*, vol. 114, no. 19, p. 195003, May 2015, doi: 10.1103/PhysRevLett.114.195003.

## Bibliography

- [43] A. Choubey *et al.*, “A highly efficient and compact long pulse Nd:YAG rod laser with 540 J of pulse energy for welding application,” *Rev. Sci. Instrum.*, vol. 84, no. 7, p. 073108, Jul. 2013, doi: 10.1063/1.4812635.
- [44] G. Huber, C. Kränkel, and K. Petermann, “Solid-state lasers: status and future {[Invited]},” *J. Opt. Soc. Am. B*, vol. 27, no. 11, pp. B93–B105, 2010, doi: 10.1364/JOSAB.27.000B93.
- [45] B. E. A. Saleh and M. C. Teich, *Fundamentals of Photonics*. Wiley, 2019.
- [46] A. E. Siegman, “New developments in laser resonators,” in *Optical Resonators*, 1990, vol. 1224, pp. 2–14, [Online]. Available: <https://doi.org/10.1117/12.18425>.
- [47] A. E. Siegman, “How to (Maybe) Measure Laser Beam Quality,” 1998, doi: 10.1364/DLAI.1998.MQ1.
- [48] A. E. Siegman, *Lasers*. University Science Books, 1986.
- [49] G. A. Reider, *Photonik*. Vienna: Springer Vienna, 2012.
- [50] D. E. McCumber, “Einstein Relations Connecting Broadband Emission and Absorption Spectra,” *Phys. Rev.*, vol. 136, no. 4A, pp. A954–A957, 1964, doi: 10.1103/PhysRev.136.A954.
- [51] M. J. Milla Rodrigo *et al.*, “Laser-induced damage threshold of Yb:YAG crystals at stretched 150-ps pulses (Conference Presentation),” in *Components and Packaging for Laser Systems IV*, Mar. 2018, p. 41, doi: 10.1117/12.2287714.
- [52] J. Koerner *et al.*, “Measurement of temperature-dependent absorption and emission spectra of Yb:YAG, Yb:LuAG, and Yb:CaF<sub>2</sub> between 20°C and 200°C and predictions on their influence on laser performance,” *J. Opt. Soc. Am. B*, vol. 29, no. 9, pp. 2493–2502, 2012, doi: 10.1364/JOSAB.29.002493.
- [53] D. Strickland and G. Mourou, “Compression of amplified chirped optical pulses,” *Opt. Commun.*, vol. 55, no. 6, pp. 447–449, 1985, doi: [https://doi.org/10.1016/0030-4018\(85\)90151-8](https://doi.org/10.1016/0030-4018(85)90151-8).
- [54] A. Giesen, H. Hügel, A. Voss, K. Wittig, U. Brauch, and H. Opower, “Scalable concept for diode-pumped high-power solid-state lasers,” *Appl. Phys. B*, vol. 58, no. 5, pp. 365–372, 1994, doi: 10.1007/bf01081875.
- [55] S. Ricaud *et al.*, “Yb:CaGdAlO<sub>4</sub> thin-disk laser,” *Opt. Lett.*, vol. 36, no. 21, pp. 4134–4136, 2011, doi: 10.1364/OL.36.004134.
- [56] T. Südmeyer *et al.*, “High-power ultrafast thin disk laser oscillators and their potential for sub-100-femtosecond pulse generation,” *Appl. Phys. B*, vol. 97, no. 2, pp. 281–295, 2009, doi: 10.1007/s00340-009-3700-z.
- [57] J. Speiser, “Scaling of thin-disk lasers - influence of amplified spontaneous emission,” *J. Opt. Soc. Am. B*, vol. 26, no. 1, pp. 26–35, 2009, doi: 10.1364/JOSAB.26.000026.
- [58] W. Koechner, “Absorbed Pump Power, Thermal Profile and Stresses in a cw Pumped Nd:YAG Crystal,” *Appl. Opt.*, vol. 9, no. 6, pp. 1429–1434, 1970, doi: 10.1364/AO.9.001429.

- [59] R. Paschotta, "Flat-top beams," *RP Photonics Encyclopedia*. Accessed: Dec. 14, 2020. [Online]. Available: [https://www.rp-photonics.com/flat\\_top\\_beams.html](https://www.rp-photonics.com/flat_top_beams.html).
- [60] G. B. Airy, "On the Diffraction of an Object-glass with Circular Aperture.," *Trans. Cambridge Philos. Soc.*, pp. 283–291, 1835.
- [61] J. Shang, X. Zhu, and G. Zhu, "Analytical approach to thermal lensing in end-pumped Yb:YAG thin-disk laser," *Appl. Opt.*, vol. 50, no. 32, p. 6103, Nov. 2011, doi: 10.1364/AO.50.006103.
- [62] D. Blázquez-Sánchez *et al.*, "Improving the brightness of a multi-kilowatt single thin-disk laser by an aspherical phase front correction," *Opt. Lett.*, vol. 36, no. 6, pp. 799–801, 2011, doi: 10.1364/OL.36.000799.
- [63] A. M. Scott, G. Cook, and A. P. G. Davies, "Efficient high-gain laser amplification from a low-gain amplifier by use of self-imaging multipass geometry," *Appl. Opt.*, vol. 40, no. 15, p. 2461, May 2001, doi: 10.1364/AO.40.002461.
- [64] H. Plaessmann, S. A. Ré, J. J. Aionis, D. L. Vecht, and W. M. Grossman, "Multipass diode-pumped solid-state optical amplifier," *Opt. Lett.*, vol. 18, no. 17, p. 1420, Sep. 1993, doi: 10.1364/OL.18.001420.
- [65] M. Shayganmanesh, M. H. Daemi, Z. Osgoui, S. Radmard, and S. S. Kazemi, "Measurement of thermal lensing effects in high power thin disk laser," *Opt. Laser Technol.*, vol. 44, no. 7, pp. 2292–2296, Oct. 2012, doi: 10.1016/j.optlastec.2012.02.019.
- [66] J. Mende, E. Schmid, J. Speiser, G. Spindler, and A. Giesen, "Thin disk laser: power scaling to the kW regime in fundamental mode operation," Feb. 2009, p. 71931V, doi: 10.1117/12.809031.
- [67] C. Herkommer *et al.*, "Ultrafast thin-disk multipass amplifier with 720 mJ operating at kilohertz repetition rate for applications in atmospheric research," *Opt. Express*, vol. 28, no. 20, p. 30164, Sep. 2020, doi: 10.1364/OE.404185.
- [68] J.-P. Negel *et al.*, "Thin-disk multipass amplifier for fs pulses delivering 400 W of average and 2.0 GW of peak power for linear polarization as well as 235 W and 1.2 GW for radial polarization," *Appl. Phys. B*, vol. 123, no. 5, p. 156, May 2017, doi: 10.1007/s00340-017-6739-2.
- [69] T. Dietz, M. Jenne, D. Bauer, M. Scharun, D. Sutter, and A. Killi, "Ultrafast thin-disk multi-pass amplifier system providing 1.9 kW of average output power and pulse energies in the 10 mJ range at 1 ps of pulse duration for glass-cleaving applications," *Opt. Express*, vol. 28, no. 8, p. 11415, Apr. 2020, doi: 10.1364/OE.383926.
- [70] R. Trebino *et al.*, "Measuring ultrashort laser pulses in the time-frequency domain using frequency-resolved optical gating," *Rev. Sci. Instrum.*, vol. 68, no. 9, pp. 3277–3295, 1997, doi: 10.1063/1.1148286.
- [71] A. A. Jalali, J. Rybarsyk, and E. Rogers, "Thermal lensing analysis of TGG and its effect on beam quality," *Opt. Express*, vol. 21, no. 11, pp. 13741–13747, 2013, doi: 10.1364/OE.21.013741.

## Bibliography

- [72] R. Antipenkov *et al.*, “The construction of Allegra kilohertz femtosecond laser system at ELI-Beamlines,” in *Short-pulse High-energy Lasers and Ultrafast Optical Technologies*, 2019, vol. 11034, pp. 58–63, doi: 10.1117/12.2524436.
- [73] R. Budriunas *et al.*, “53 W average power CEP-stabilized OPCPA system delivering 5.5 TW few cycle pulses at 1 kHz repetition rate,” *Opt. Express*, vol. 25, no. 5, pp. 5797–5806, 2017, doi: 10.1364/OE.25.005797.
- [74] O. Hort *et al.*, “High-flux source of coherent XUV pulses for user applications,” *Opt. Express*, vol. 27, no. 6, p. 8871, Mar. 2019, doi: 10.1364/OE.27.008871.
- [75] M. Chyla, T. Miura, M. Smrz, H. Jelinkova, A. Endo, and T. Mocek, “Optimization of beam quality and optical-to-optical efficiency of Yb:YAG thin-disk regenerative amplifier by pulsed pumping,” *Opt. Lett.*, vol. 39, no. 6, p. 1441, Mar. 2014, doi: 10.1364/OL.39.001441.
- [76] M. Siebold *et al.*, “Terawatt diode-pumped Yb:CaF<sub>2</sub> laser,” *Opt. Lett.*, vol. 33, no. 23, p. 2770, Dec. 2008, doi: 10.1364/OL.33.002770.
- [77] D. L. Brown, I. Will, and W. Seka, “Large-aperture ring amplifier with gains in excess of 40,000 and several-joule output capability,” in *Conference on Lasers and Electro-Optics*, 1993, p. CTuN37, [Online]. Available: <http://www.osapublishing.org/abstract.cfm?URI=CLEO-1993-CTuN37>.
- [78] S. Kahaly *et al.*, “Direct Observation of Density-Gradient Effects in Harmonic Generation from Plasma Mirrors,” *Phys. Rev. Lett.*, vol. 110, no. 17, p. 175001, Apr. 2013, doi: 10.1103/PhysRevLett.110.175001.
- [79] M. Ueffing, “Direct amplification of femtosecond pulses,” Ludwig-Maximilians-Universität München, 2018.

# List of publications

## Peer reviewed journal articles

- D. E. Rivas, A. Borot, D. E. Cardenas, G. Marcus, X. Gu, D. Herrmann, J. Xu, J. Tan, **D. Kormin**, G. Ma, W. Dallari, G. D. Tsakiris, I. B. Földes, S.-w. Chou, M. Weidman, B. Bergues, T. Wittmann, H. Schröder, P. Tzallas, D. Charalambidis, O. Raszkazovskaya, V. Pervak, F. Krausz and L. Veisz. "Next Generation Driver for Attosecond and Laser-plasma Physics." *Sci Rep* 7, 5224 (2017).

I implemented the plasma mirror setup for the contrast enhancement and participated in the CEP-tagging experiments.

- **Dmitrii Kormin**, Antonin Borot, Guangjin Ma, William Dallari, Boris Bergues, Márk Aladi, István B. Földes and Laszlo Veisz, "Spectral interferometry with waveform-dependent relativistic high-order harmonics from plasma surfaces." *Nat Commun* 9, 4992 (2018).

I performed the experiment and the analysis of the experimental data. I also contributed to the invention of the harmonics interferometric treatment by testing this approach on the experimental data and optimizing it for the best agreement with the simulations results.

- Olga Jahn, Vyacheslav E. Leshchenko, Paraskevas Tzallas, Alexander Kessel, Mathias Krüger, Andreas Münzer, Sergei A. Trushin, George D. Tsakiris, Subhendu Kahaly, **Dmitrii Kormin**, Laszlo Veisz, Vladimir Pervak, Ferenc Krausz, Zsuzsanna Major, and Stefan Karsch, "Towards intense isolated attosecond pulses from relativistic surface high harmonics." *Optica* 6, 280-287 (2019).

I participated in the experiment preparation.

- Martin Kaumanns, Vladimir Pervak, **Dmitrii Kormin**, Vyacheslav Leshchenko, Alexander Kessel, Moritz Ueffing, Yu Chen, and Thomas Nubbemeyer, "Multipass spectral broadening of 18mJ pulses compressible from 1.3ps to 41fs." *Opt. Lett.* 43, 5877-5880 (2018).

I contributed to the experiment and the discussion of the results.

- Martin Kaumanns, **Dmitrii Kormin**, Thomas Nubbemeyer, Vladimir Pervak and Stefan Karsch, "Spectral broadening of 112mJ, 1.3ps pulses at 5kHz in a LG01 multipass cell with compressibility to 37fs." *Opt. Lett.* 46, 929-932 (2021)

I contributed to the experiment and the discussion of the results.

## List of publications

# Acknowledgements

First of all, I would like to thank my supervisor Professor Ferenc Krausz for giving me this unique opportunity to join his research team and to work in the most advanced and well-equipped optical laboratories of Max-Planck-Institute for Quantum Optics and Ludwig Maximilian University of Munich. All my researches as well as this thesis would not be possible without his continuous support.

It is also impossible to underestimate the importance of communication with many people I have been lucky to meet during my research and who provided me a lot of scientific and personal support.

I want to thank Professor Laszlo Veisz, who invited me to join his project at MPQ in the very beginning of my research carrier and thus opened me a path into ultrafast and attosecond science. I also cordially thank my first science-mates Antonin Borot and William Dallari, who helped me to dive into this exciting and complicated topic. Additionally I express my thanks to Boris Bergues, George Tsakiris and Guangjin Ma for their help in understanding and interpreting the experimental results and matching them with the model. It is also important to thank the colleagues from the adjacent experiments, namely Daniel Rivas, Daniel Cardenas and Matthew Weidman, who shared their valuable experience with the driving laser system and put a lot of efforts into its stable operation.

Great thanks to Tanya Bergues and Monika Wild, who helped me to organize my moving to Munich and assisted me a lot during my first months in Germany. None less gratitude has to be expressed to my former wife Anastasiia Averina. Though our life-paths diverged, without her care and support I would not have been able to adapt so quickly to a completely new environment and concentrate on the research from the very beginning.

My transition from MPQ to the laser development laboratories of LMU was simple and comfortable thanks to friendly and cooperative atmosphere that Thomas Nubbemeyer as the project coordinator organized in his group. He did not only help to fill the gaps in my knowledge in this field and assisted a lot in the lab work, but also provided important support in terms of integration to a new social group and communication with colleagues and superiors. In addition, I would also like to express my thankfulness to Oleg Pronin and Hannieh Fattahi for their valuable advices in different complicated situations, requiring an unbiased view from outside.

I thank my laboratory colleagues Mathias Krüger, Moritz Üffing, Florian Saran and Andreas Münzer for their assistance in the lab. Martin Kaumanns deserves a special thank for a long and productive cooperation. His laser development experience and readiness to start both a complicated discussion about physical processes and an entertaining mind-refreshing small talk played an important role in efficient daily work during all these years.

## **Acknowledgements**

I also thank those colleagues from the neighboring laboratories, who did not directly participate in my researches but nevertheless was a part of a big and friendly team of like-minded scientists: Ayman Alismail, Haochuang Wang, Gaia Barbiero, Simon Reiger, Olga Jahn and Vyacheslav Leshchenko. Additionally I want to say thanks to Markus Pötzlberger, Kafai Mak, Nathalie Nagl, Sebastian Gröbmeyer, Daniel Gerz and Christina Hofer for wonderful parties and different entertainment events, which are absolutely necessary for a good rest from work.

Finally I would like to thank all the people, who provide necessary technical and administrative assistance to our research group. I thank Vladimir Pervak and his team for providing crucial for laser development high-quality coatings and Johannes Wulz, Klaus Wirgler and Christoph Rahm for their help in designing vacuum chambers. Special thanks to Rolf Öhm and other co-workers of the LMU workshop for manufacturing different non-standard mechanical components. Besides, I want to thank TRUMPF GmbH + Co. KG and TRUMPF Scientific Lasers GmbH + Co. KG for their cooperation and providing high quality thin disks and related equipment. I also greatly appreciate the assistance of the LMU administration, particularly Hans-Friedrich Wirth, Klaus Franke, Katharina Adler and Martin Groß.